



# Investigating aerodynamic performance of a coaxial dual-rotor wind turbine



**Author:**  
**Harika Gurram**  
DTU Wind-M-0767  
December 2024

**Author:**  
Harika Gurram

**Title:**  
Investigate aerodynamic performance of  
a coaxial dual-rotor wind turbine

DTU Wind & Energy Systems is a department of the Technical University of Denmark with a unique integration of research, education, innovation and public/private sector consulting in the field of wind energy. Our activities develop new opportunities and technology for the global and Danish exploitation of wind energy. Research focuses on key technical-scientific fields, which are central for the development, innovation and use of wind energy and provides the basis for advanced education at the education.

DTU Wind-M-0767  
December 2024

ECTS: 45

Education: Master of Science

**Supervisors:**

Jens Nørkær Sørensen

**DTU Wind & Energy Systems**

Wei Yu

**TU Delft**

Torben Juul Larsen

**Vestas Wind System A/S**

**Remarks:**

This report is submitted as partial fulfillment of the requirements for graduation in the above education at the Technical University of Denmark.

**Technical University of Denmark**  
Department of Wind and Energy Systems  
Frederiksborgvej 399  
4000 Roskilde  
Denmark  
[www.wind.dtu.dk](http://www.wind.dtu.dk)

# Investigating aerodynamic performance of a coaxial dual-rotor wind turbine

by

Harika Gurram

to obtain the degrees of

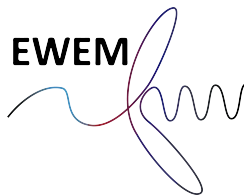
**Master of Science**  
in Wind Energy  
at Technical University of Denmark

**Master of Science**  
in Aerospace Engineering  
at Delft University of Technology

*To be defended on the 10 of December, 2024*

|                    |  |   |
|--------------------|--|---|
| Supervisors:       | Wei Yu<br>Jens Nørkær Sørensen<br>Torben Juul Larsen | TU Delft<br>DTU<br>Vestas Wind System A/S |
| Defence committee: | Dominic von Terzi<br>Robert Flemming Mikkelsen       | TU Delft<br>DTU                           |
| Start date:        | November 1, 2023                                     |   |
| End date:          | December 10, 2024                                    |   |
| Student numbers:   | TU Delft:<br>DTU:                                    | 5834430<br>s223693                        |

An electronic version of this thesis is available at  
<https://repository.tudelft.nl> and <https://findit.dtu.dk>



# Abstract

---

Wind turbine technology has advanced significantly as a result of the growing need for renewable energy to fight climate change and lessen reliance on fossil fuels. Dual-rotor wind turbines are one of these developments that shows promise for increasing energy extraction efficiency by absorbing wake energy that remains from the upwind rotor. The impact of rotor spacing, tip-speed ratio, rotating direction, and pitch angle on turbine efficiency are the main topics of this study, which examines the aerodynamic performance of coaxial dual-rotor wind turbines.

The study computes the effect of axial induction while neglecting tangential induction. It also highlights the distinct advantages of both co-rotating (CO-RWT) and counter-rotating (CR-RWT) systems, examining the aerodynamic differences between them. Actuator Disc Model (ADM) simulations, Blade Element Momentum (BEM) theories, and analytical techniques are used to determine velocity deficits and assess rotor interactions. The results show that CR-RWT setups provide better power. The findings demonstrate that CR-RWT configurations achieve high power coefficients due to improved wake recovery and reduced turbulence, while CO-RWT designs prioritize increased torque and power density.

The analysis reveals that parameters such as rotor spacing and TSR significantly influence the aerodynamic interactions between both the rotors. Optimal spacing minimizes wake interference, while precise control of TSR and pitch angles improves overall turbine performance. By systematically investigating these factors, this work identifies the conditions under which dual-rotor wind turbines can maximize energy output and efficiency. The study provides valuable insights into optimal design parameters for dual-rotor configuration, contributing to the development of cost-effective, high-efficiency wind turbines for future energy needs.

# Acknowledgements

---

My tale of gratitude and motivation goes hand in hand. Before I fondly acknowledge the presence and incredible contributions of a plethora of people in my life, my mind wanders through memory lane. While the aftermath of the pandemic brought irreversible changes to the world, the zestful and positive side of my Libra personality pushed me to explore how I could amplify my contribution to a better tomorrow. Sustainability became more than a buzzword, and I began pondering how I could use my formal training in aerospace engineering in these avenues of the future. This exploration led me to the discovery of EWEM. Thus began a 2-year journey filled with curiosity, resilience, lifelong learning, immutable friendships, and core transformation.

I would like to first extend my heartfelt gratitude to all my professors who in addition to being stalwarts in their field are amazing human beings and have inspired me in every junction. The lectures in the classrooms, the engaging assignments, the eventful extra curriculars, the fulfilling field trips and the insightful tests are the testament to the massive impact and uniqueness of this program, and I would like to thank the entire management and program coordinating team at both TU Delft and DTU for designing and modelling such an exceptional program.

My sincere thanks also go to my supervisors Professor Jens, Assistant Professor Dr. Wei, Mr. Torben and Mr Rob for entrusting me with this beautiful topic and guiding me through the entire thesis. My every consultation with these erudite gurus felt like having an encyclopedia at my fingertip and I can't thank them enough for their constructive and candid feedback. My journey in this graduate program took an extraordinary turn when I discovered that I would not only be graduating with a degree but also a tiny human being. The journey of motherhood, intertwined with the story of this master's program, creates a beautiful chapter in my life. There were times when my body and my mind coaxed me to give up but not once has my soul shown me the exit door. The arrival of my daughter bolstered my resilience further. Suddenly, I had another reason to do justice to this arduous 2-year story. Witnessing my 10-month-old's determination to figure out every new toy drove me to burn the midnight oil and give my all. So, I would like to thank my daughter for making me a better person and a better academician.

I would like to thank my entire cohort for making the discussions so engaging and perspective. I would like to specially thank my friends in DTU and TU Delft for their remarkable support throughout the program.

My sister, Dr. Harsha Gurram, have been the cornerstone of my life and I am forever indebted to her. I cannot imagine even the beginning of my journey without my wonderful parents, and I have no words to express my gratitude towards them. I would specially like to thank my mother, my eternal source of unmatched strength, who always nurtures and brings out the best in me. My in-laws, especially my sister-in-law, have been a sounding board for

me, saving countless hours of therapist money. Lastly, I want to thank the person whose hand I am holding right now—my husband, my guiding light—without whom I would still be lost in the streets of Austin. Finally, this is for you! This is dedicated to my daughter, Samanvi Sabyasachi. May you grow into a wonderful human being that I know you are and may your priceless smile continue to light up your mother's life.

**HARIKA**

# Contents

---

|          |  |           |
|----------|--|-----------|
| <b>1</b> | <b>Introduction</b>                                      | <b>1</b>  |
| 1.1      | Literature Review . . . . .                              | 4         |
| 1.1.1    | Analytical and Semi-Analytical Approaches . . . . .      | 4         |
| 1.1.2    | Computational Fluid Dynamics Simulations . . . . .       | 6         |
| 1.1.3    | Experimental and Wind Tunnel Studies . . . . .           | 9         |
| 1.1.4    | Summary . . . . .  | 10        |
| 1.2      | Research Gap . . . . .                                   | 12        |
| 1.3      | Research Questions . . . . .                             | 12        |
| 1.4      | Thesis Outline . . . . .                                 | 13        |
| <b>2</b> | <b>State of the Art</b>                                  | <b>15</b> |
| 2.1      | Analytical and Semi-Analytical Methods . . . . .         | 15        |
| 2.1.1    | 1-D Momentum Theory . . . . .                            | 15        |
| 2.1.2    | Blade Element Momentum Theory for Single-Rotor . . . . . | 19        |
| 2.1.3    | Wake velocity . . . . .                                  | 22        |
| 2.1.3.1  | Wilson's Velocity Model . . . . .                        | 23        |
| 2.1.3.2  | O.Gur's induced velocity model . . . . .                 | 25        |
| 2.1.4    | Blade Element Method for Dual Rotors . . . . .           | 27        |
| 2.2      | Computational Methods . . . . .                          | 30        |
| 2.2.1    | Actuator Disk Model . . . . .                            | 30        |
| 2.3      | Uncertainties . . . . .                                  | 31        |
| 2.4      | Parametric Study . . . . .                               | 33        |
| 2.5      | Annual Energy Production . . . . .                       | 33        |
| 2.6      | Summary . . . . .  | 34        |
| <b>3</b> | <b>Methodology</b>                                       | <b>35</b> |
| 3.1      | Blade Element Method . . . . .                           | 35        |
| 3.2      | Actuator Disc Method . . . . .                           | 36        |
| 3.2.1    | Mesh Independence Study . . . . .                        | 37        |
| 3.2.1.1  | Varying Mesh Size . . . . .                              | 37        |
| 3.2.1.2  | Varying Domain Size . . . . .                            | 38        |
| 3.2.1.3  | Varying Turbulence Intensity . . . . .                   | 39        |
| 3.2.1.4  | Final Simulation Setup . . . . .                         | 39        |
| 3.3      | Summary . . . . .  | 40        |
| <b>4</b> | <b>Single Rotor Performance and Validation</b>           | <b>43</b> |
| 4.1      | Introduction . . . . .                                   | 43        |
| 4.2      | BEM Results . . . . .                                    | 43        |
| 4.2.1    | Determining Optimal Operating Conditions . . . . .       | 43        |

---

|          |  |           |
|----------|--|-----------|
| 4.2.2    | Validation . . . . .   | 46        |
| 4.2.3    | Annual Energy Production . . . . .   | 49        |
| 4.3      | Actuator Disc Simulations Results . . . . .                                  | 50        |
| 4.4      | Summary . . . . .  | 51        |
| <b>5</b> | <b>Dual Rotor Performance - No rotation</b>                                  | <b>52</b> |
| 5.1      | Introduction . . . . .   | 52        |
| 5.2      | BEM Results . . . . .  | 52        |
| 5.2.1    | Velocity in the wake . . . . .   | 52        |
| 5.2.2    | Varying downstream distance . . . . .  | 53        |
| 5.2.3    | Effect of variable rotational speed . . . . .                                | 57        |
| 5.2.4    | Effect of variable pitch . . . . .   | 61        |
| 5.3      | Actuator Disc Simulation Results . . . . .                                   | 63        |
| 5.4      | Summary . . . . .  | 70        |
| <b>6</b> | <b>Co and Counter Rotating Dual Rotor Performance</b>                        | <b>72</b> |
| 6.1      | Introduction . . . . .   | 72        |
| 6.2      | BEM Results . . . . .  | 72        |
| 6.2.1    | Comparing CO-RWT and CR-RWT the performance . . . . .                        | 73        |
| 6.3      | Power Comparison for Optimal Co-Rotating and Counter-Rotating Configurations | 78        |
| 6.3.1    | Power Contributions from Individual Rotors . . . . .                         | 80        |
| 6.4      | Model comparison . . . . .   | 80        |
| 6.5      | Summary . . . . .  | 82        |
| <b>7</b> | <b>Conclusion</b>  | <b>83</b> |
|          | <b>References</b>  | <b>I</b>  |
|          | <b>Bibliography</b>  | <b>I</b>  |

# List of Figures

---

|      |   |    |
|------|---|----|
| 1.1  | New capacity installed and top five market share [1] . . . . .  | 1  |
| 1.2  | Dual-rotor configuration with both rotors placed behind the hub [11] . . . . .  | 3  |
| 1.3  | Dual-rotor configuration with rotors placed behind on either side of the nacelle hub [12] . . . . .   | 3  |
| 1.4  | Dual-rotating wind turbine with identical rotor diameters mounted on either side of the nacelle used for present study . . . . .  | 3  |
| 1.5  | Dual rotor actuator disc model [13] . . . . .   | 4  |
| 1.6  | Inflow for BEMT for CR-RWT with downwind rotor operating inside the stream tube of upwind rotor [15] . . . . .  | 5  |
| 1.7  | Actuator disk and blade-element models illustrating the velocity components for CRWT. [16] . . . . .  | 6  |
| 1.8  | Comparing AEP of CRWT and SRWT (located in the island of Sprogø, Denmark) [7]   | 7  |
| 1.9  | Mesh in the domain (Left), surface mesh on the blade surface for counter-rotating wind turbine [5] . . . . .  | 7  |
| 1.10 | Increase in normalized maximum power coefficient and the normalization of total power coefficient for CRWT against SRWT according to rotor axial distance ratio with diameter ratio $D1/D2 = 1.0$ . [5] . . . . . | 8  |
| 1.11 | a.CO-RWT dual rotors, b.CO-RWT tri-rotors c. CR-RWT dual rotor d.c with a $15^\circ$ phase difference e.CR-RWT dual rotor with phase-difference of $90^\circ$ [19] . . . . .                                      | 8  |
| 1.12 | Velocity contours downstream for a.single rotor case, b.co-rotating dual rotor, c.Three rotor co-rotating d.counter-rotating wind turbines.[19] . . . . .   | 9  |
| 1.13 | Dual rotor experimental setup . . . . .   | 10 |
| 1.14 | Dual rotor Sairui [26] . . . . .  | 10 |
| 2.1  | Illustration of a 1-D Streamtube . . . . .  | 15 |
| 2.2  | $C_P$ and $C_T$ as functions of axial induction factor $a$ . . . . .  | 17 |
| 2.3  | Dual-rotor setup . . . . .  | 18 |
| 2.4  | Blade sections [27] . . . . .   | 19 |
| 2.5  | BEM flow chart . . . . .  | 20 |
| 2.6  | Wake behind the wind turbine [29] . . . . .   | 22 |
| 2.7  | Normalised wake velocity computed using Wilson's equation for $C_T = 0.8$ . . . . .   | 25 |
| 2.8  | (a) Axial and (b) Tangential velocity evolution in the downstream (c) Distance coefficient angle [31] . . . . .   | 26 |
| 2.9  | Normalised wake velocity computed using Wilson's equation for $C_T = 0.8$ . . . . .   | 27 |
| 2.10 | Dual rotors wind turbine definition . . . . .   | 27 |
| 2.11 | Counter-rotating case [31] . . . . .  | 29 |
| 2.12 | Co-rotating case [31] . . . . .   | 29 |
| 2.13 | Actuator disk model [27] . . . . .  | 30 |
| 2.14 | Weibull probability density function for the wind speed [33] . . . . .  | 34 |

|      |  |    |
|------|--|----|
| 3.1  | Mesh refinement for fine mesh . . . . .  | 38 |
| 3.2  | Final domain size . . . . .  | 38 |
| 3.3  | Axial Velocity downstream of the upstream rotor for coarse mesh . . . . .  | 40 |
| 3.4  | Smoothed Axial Velocity downstream of the upstream rotor for coarse mesh . . . . .   | 40 |
| 3.5  | Radial variation of axial induction downstream of the upstream rotor for coarse mesh . . . . .   | 40 |
| 3.6  | Comparing ADM results with theory . . . . .  | 40 |
| 4.1  | Variation of $C_p$ for different $\lambda$ and $\theta$ (contour) . . . . .  | 43 |
| 4.2  | Variation of $C_P$ for different $\lambda$ and $\theta$ (surface) . . . . .  | 44 |
| 4.3  | Variation of $C_T$ for different $\lambda$ and $\theta$ (contour) . . . . .  | 44 |
| 4.4  | Variation of $C_T$ for different $\lambda$ and $\theta$ (surface) . . . . .  | 44 |
| 4.5  | Thrust for high pitch and low pitch . . . . .  | 45 |
| 4.6  | Power for high pitch and low pitch . . . . .   | 46 |
| 4.7  | Comparison of reference model coefficient of power across velocities with BEM results . . . . .  | 47 |
| 4.8  | Comparison of reference model coefficient of thrust across velocities with BEM Results . . . . .   | 47 |
| 4.9  | Comparison of reference model power across velocities with BEM Results . . . . .   | 47 |
| 4.10 | Comparison of reference model thrust across velocities with BEM Results . . . . .  | 47 |
| 4.11 | Normal force distribution over blade span for different wind speeds . . . . .  | 48 |
| 4.12 | Tangential force distribution over blade span for different wind speeds . . . . .  | 48 |
| 4.13 | Power coefficient variation across wind speeds for different TSR . . . . .   | 48 |
| 4.14 | Thrust coefficient variation across wind speeds for different TSR . . . . .  | 48 |
| 4.15 | Power variation across wind speeds for different TSR . . . . .   | 48 |
| 4.16 | Thrust variation across wind speeds for different TSR . . . . .  | 48 |
| 4.17 | Axial induction factor distribution over bladespan . . . . .   | 49 |
| 4.18 | Tangential induction factor distribution over bladespan . . . . .  | 49 |
| 4.19 | Validating the ADM power values with BEM and DTU 10MW results . . . . .  | 50 |
| 4.20 | Normalised velocity variation in the downstream for variable $C_T$ . . . . .   | 51 |
| 5.1  | Normalised velocity in the wake of upwind rotor ( $\lambda = 8$ ) . . . . .  | 53 |
| 5.2  | Sketch illustrating dual rotor for different downstream distances (not to the scale) . . . . .   | 53 |
| 5.3  | Comparing the Power for single rotor and downwind rotor placed at different downstream distances . . . . .   | 54 |
| 5.4  | Comparing the Thrust for single rotor and downwind rotor placed at different downstream distances . . . . .  | 55 |
| 5.5  | Comparing the single rotor Power[W] to the dual-rotor . . . . .  | 55 |
| 5.6  | Comparing the single rotor Thrust[N] to the dual-rotor . . . . .   | 56 |
| 5.7  | Comparing Power single-rotor to dual-rotor varying with the distance between the rotors . . . . .  | 56 |
| 5.8  | Comparing Thrust single-rotor to dual-rotor varying with distance between the rotors . . . . .   | 57 |
| 5.9  | Normalised velocity in the wake of upwind rotor for varying TSR . . . . .  | 58 |
| 5.10 | Comparing the Power[W] for dual rotor, single rotor and downwind rotor contribution for the upwind and downwind rotors operating at same TSR . . . . .   | 58 |
| 5.11 | Comparing the Thrust [N] for dual rotor, single rotor and downwind rotor contribution for the upwind and downwind rotors operating at same TSR . . . . . | 59 |
| 5.12 | Comparing the total power for various TSR combinations . . . . .   | 60 |
| 5.13 | Comparing the total thrust for various TSR combinations . . . . .  | 60 |
| 5.14 | The velocity deficit for varying pitch at upwind optimal operating conditions . . . . .  | 61 |

|      |  |    |
|------|--|----|
| 5.15 | Power coefficient variation for pitch difference between two rotors as a set of curves for increasing upwind rotor pitch . . . . .   | 62 |
| 5.16 | Power coefficient variation for DRWT 10%D pitch difference between two rotors as a set of curves for increasing upwind rotor pitch . . . . .                                     | 62 |
| 5.17 | Power coefficient variation for pitch difference between two rotors as a set of curves for increasing upwind rotor pitch . . . . .   | 63 |
| 5.18 | Axial velocity in the downstream wake of the upstream rotor. The velocity is compared between Wilson's model, Actuator Disc Model (ADM), and observed far-wake velocity. . . . . | 64 |
| 5.19 | Comparing normalised velocity in upstream and downstream for single rotor and dual rotor for centerline ( $r/R = 0$ ) . . . . .  | 65 |
| 5.20 | Comparing normalised velocity in upstream and downstream for SWRT and DWRT for $r/R = 95$ . . . . .  | 65 |
| 5.21 | Influence of downwind rotor on upwind rotor for different rotor spacing . . . . .  | 66 |
| 5.22 | Normalized velocity contours for single and dual rotor configurations with $C_T = 0.2$ .   | 67 |
| 5.23 | Normalized velocity contours for single and dual rotor configurations with $C_T = 0.6$ .   | 67 |
| 5.24 | Normalized velocity contours for single and dual rotor configurations with $C_T = 1.2$   | 67 |
| 5.25 | Comparing pressure coefficient for the single rotor to dual rotor with $C_T = 0.2$ . .   | 68 |
| 5.26 | Comparing pressure coefficient for the single rotor to dual rotor with $C_T = 0.8$ . .   | 68 |
| 5.27 | Comparing pressure coefficient for the single rotor to dual rotor with $C_T = 1.2$ . .   | 69 |
| 5.28 | influence of the downwind rotor on upwind rotor for variable upwind loading and downwind rotor $TSR = 8$ . . . . .   | 70 |
| 6.1  | Comparing the velocity deficit equations given by Wilson [28] and Gur [16] . . . . .   | 72 |
| 6.2  | Comparing the single-rotor Power [W] to the Co-Rotating Configuration . . . . .  | 73 |
| 6.3  | Comparing the singleT Power [W] to the Counter-Rotating Configuration . . . . .  | 73 |
| 6.4  | Comparing the single rotor Power [W] to the downwind rotor in co-rotating configuration . . . . .  | 74 |
| 6.5  | Comparing the single-rotor Power [W] to the downwind rotor in counter-rotating configuration . . . . .   | 74 |
| 6.6  | Comparing the single-rotor Thrust [N] output to downwind rotor (co-rotating) . .   | 75 |
| 6.7  | Comparing the single-rotor Thrust [N] output to downwind rotor (counter-rotating)  | 75 |
| 6.8  | Comparing the SRWT Torque [N-m]output to downwind rotor (co-rotating) . . . . .  | 76 |
| 6.9  | Comparing the SRWT Torque [N-m] output to downwind rotor (counter-rotating)  | 76 |
| 6.10 | Comparing the total power for various TSR combinations for co-rotating . . . . .   | 77 |
| 6.11 | Comparing the total power for various TSR combinations for counter-rotating . . .  | 77 |
| 6.12 | Comparing the total thrust for various TSR combinations for co-rotating . . . . .  | 78 |
| 6.13 | Comparing the total thrust for various TSR combinations for counter-rotating . .   | 78 |
| 6.14 | Comparing Total power for Co Rotating configuration . . . . .  | 79 |
| 6.15 | Comparing Total power for Counter Rotating configuration . . . . .   | 79 |
| 6.16 | Comparing performance for Co- Rotating configuration . . . . .   | 79 |
| 6.17 | Comparing performance for Counter Rotating configuration . . . . .   | 79 |
| 6.18 | Comparing the different models used to compute the wake velocity in the downstream   | 81 |

# List of Tables

---

|     |  |    |
|-----|--|----|
| 1.1 | Summary of dual-rotor research grouped by approach with Power output . . . . .                   | 11 |
| 3.1 | Specifications of the DTU 10MW [34] . . . . .  | 36 |
| 3.2 | Mesh size sensitivity analysis . . . . .   | 37 |
| 3.3 | Domain size sensitivity analysis . . . . .   | 38 |
| 3.4 | Turbulence model and intensity sensitivity analysis . . . . .                                    | 39 |
| 3.5 | Summary approach, assumptions, limitations, and comparison . . . . .                             | 42 |
| 5.1 | Power Output for Single and Dual Rotor Configurations at Varying Spacings . . .                  | 66 |
| 5.2 | Comparison of Power Output for Single and Dual Rotor Configurations with Varying $C_T$ . . . . . | 69 |
| 6.3 | Comparison of Wilson's Model, ADM, and Linear Variation (O Gur) . . . . .                        | 81 |

# Nomenclature

---

|        |                                 |           |   |
|--------|---------------------------------|-----------|---|
| ADM    | Actuator Disc Model             | HAWC2     | Horizontal Axis Wind turbine simulation Code 2nd generation (DTU) |
| AEP    | Annual Energy Production        | HAWCStab2 | Steady state version of HAWC2 for stability analysis (DTU)        |
| ALM    | Actuator Line Method            | HAWT      | Horizontal Axis Wind Turbine                                      |
| BEM    | Blade Element Momentum          | IP-BRM    | In-Plane Blade Root Moment  |
| CFD    | Computational Fluid Dynamics    | LES       | Large Eddy Simulation   |
| CO-RWT | Co-Rotating Wind Turbine        | MRWT      | Multiple Rotor Wind Turbine                                       |
| CR-RWT | Counter-Rotating Wind Turbine   | OOP-BRM   | Out-Of-Plane Blade Root Moment                                    |
| DNS    | Direct Numerical Simulation     | SRWT      | Single Rotor Wind Turbine   |
| DRWT   | Dual Rotor Wind Turbine         | TB-FA     | Tower Base Fore-Aft Moment  |
| DTU    | Technical University of Denmark | TB-SS     | Tower Base Side-Side Moment                                       |
| GW     | Gigawatt                        | TSR       | Tip Speed Ratio   |
| GWEC   | Global Wind Energy Council      | W         | Watt  |
| GWh    | Gigawatt-hour                   |           |   |

# Table of Symbols

---

| <b>Symbol</b> | <b>Description</b>          |
|---------------|-----------------------------|
| $C_P$         | Power coefficient           |
| $C_T$         | Thrust coefficient          |
| $T$           | Thrust force                |
| $Q$           | Torque                      |
| $p$           | Pressure                    |
| $P$           | Power                       |
| $D$           | Rotor Diameter              |
| $A_d$         | Area of Rotor Disc          |
| $R$           | Radius of Rotor Disc        |
| $\rho$        | Density of Air              |
| $U_\infty$    | Free-stream velocity        |
| $U_d$         | Velocity at Rotor Disc      |
| $a$           | Axial Induction Factor      |
| $a'$          | Tangential Induction Factor |
| $V_{rel}$     | Relative Velocity           |
| $C_L$         | Lift coefficient            |
| $C_D$         | Drag coefficient            |
| $\alpha$      | Angle of attack             |
| $\phi$        | Flow angle                  |
| $\Omega$      | Angular velocity of rotor   |
| $\lambda$     | Tip speed ratio             |
| $\theta$      | Pitch angle                 |
| $C_l$         | Lift coefficient            |
| $c$           | Chord Length                |

# CHAPTER 1

## Introduction

The global demand for sustainable solutions to mitigate climate change and reduce dependence on fossil fuels remains strong. To meet this demand the focus is on renewable energy sources. The Global Wind Energy Council 2024 (GWEC) report highlights that the wind energy sector achieved a milestone in 2023, surpassing 117GW of new capacity additions, which is a remarkable 50% increase compared to 2022 [1]. This unprecedented growth signals a phase of rapid expansion driven by increased political commitments, including 28<sup>th</sup> the ambitious goal of the Conference of the Parties (COP28) of tripling renewable energy capacity by 2030.

The increase in wind power installations is driven by national policy structures, advances in offshore wind technology, and new markets across 54 countries. However, the report states that achieving global climate objectives will require scaling annual wind capacity additions to 320GW by 2030. Figure 1.1 illustrates the top five market leaders and their respective shares in new capacity installations. It shows the global distribution of the new wind energy capacity (= 116.6GW) installed in 2023. The Asia-Pacific region, dominated by China, accounted for 71% of installations, followed by Europe (16%), North America (7%), Latin America (5%), and Africa & the Middle East (1%). China led individual country contributions with 65% of the global total, while the United States (12%), Brazil (5%), Germany (4%), and India (4%) were key contributors. This reflects the pivotal role of established and emerging markets in driving wind energy expansion worldwide.

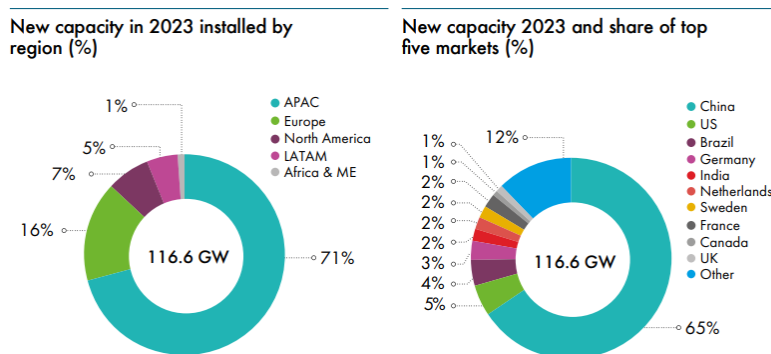


**Figure 1.1:** New capacity installed and top five market share [1]

In response to escalating energy demands, the advancements in wind turbine rotor technology have become essential. Continuous innovation in turbine designs has led to the development of novel configurations that ensure high efficiency in power generation while reducing the spatial footprint and the costs incurred during manufacturing and maintenance. These designs include multi-rotor wind turbines, which distribute loads across multiple rotors, thereby increasing power output. Another example is the coaxial dual-rotor configuration, with two rotors aligned

along the same axis. The conventional horizontal axis single-rotor wind turbine can convert  $\approx 59\%$  of the available wind kinetic energy into mechanical energy described by Betz limit [2]. As only two-thirds of the wind energy is captured by the single rotor integrating an additional rotor downstream of the initial one, the dual-rotor design allows extraction of the residual energy in the wake, further increasing overall energy capture.

The dual-rotor design allows flexibility and adaptability to optimize the performance across different environmental conditions and reduce overall maintenance costs [3]. The current work focuses on investigating the aerodynamic performance of a coaxial dual-rotor wind turbine, where the downwind rotor is positioned behind the nacelle hub. The primary goal is to study the effects of the induction factor, analyze the key parameters affecting turbine efficiency, and identify the optimal configuration.

Newman[4] expanded the classical actuator disc theory for single-rotor to multiple rotors, assuming no fluid rotation, and, calculated the maximum power coefficient for  $n$  actuator disc. Subsequent research further investigated the influence of the fluid rotation on the performance of the dual rotor, where the downwind rotor is rotating in the same direction as the upwind rotor which is termed Co-Rotating (CO-RWT) and when the downwind rotor is rotating in the opposite direction termed Counter-Rotating (CR-RWT). The aerodynamic performance of these configurations were validated through CFD simulations and experimental testing [5, 6]. Studies such as [7, 8] report that CR-RWT wind turbines can enhance power production by 7% to 20% compared to conventional single-rotor designs.

CO-RWT configurations increase torque, as the downwind rotor utilizes additional wind energy from the upwind rotor's wake. This configuration results in an increase in power output without a proportional increase in swept area. The main advantage of CO-RWT is its ability to generate more power from a given turbine size, which, in turn, potentially reduces foundation and structural costs. CR-RWT configurations also utilize the energy in the wake of the upwind rotor. However, in contrast to CO-RWT, CR-RWT configurations reduce aerodynamic losses typically found in the wake of single-rotor systems, improving efficiency and stability. In CR-RWT, the downwind rotor mitigates turbulence generated by the upwind rotor, creating a more stable flow and reducing energy losses. CR-RWT turbines also generate balanced torque, reducing structural stress and enabling simpler, lighter design requirements. This design improves energy capture and stability, particularly in variable wind conditions, as counter-rotation naturally stabilizes the system against lateral forces. While CO-RWT turbines prioritize power enhancement through increased torque, CR-RWT turbines focus on stability, reduced turbulence, and efficient energy capture.

Several factors influence the aerodynamic performance of CO-RWT and CR-RWT turbines, including rotor spacing, tip-speed ratio (TSR), and rotational speed. Research shows that rotor spacing significantly affects aerodynamic interaction, and optimizing this distance enhances energy capture by the rear rotor [9]. Additionally, precise control of TSR and rotational speed can further improve system efficiency [6]. Furthermore, these configurations use rotors with either identical or different diameters, positioned on the same side of the nacelle, as shown in Figure 1.2, or on opposite sides of the nacelle, as shown in Figure 1.3. Each design presents unique advantages and challenges [10].



**Figure 1.2:** Dual-rotor configuration with both rotors placed behind the hub [11]

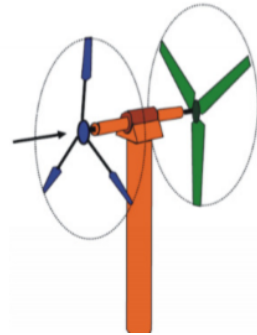


**Figure 1.3:** Dual-rotor configuration with rotors placed behind on either side of the nacelle hub [12]

The present study focuses on a co-axial dual rotor configuration with identical rotor diameters and blades mounted on either side of the nacelle, as shown in 1.4.

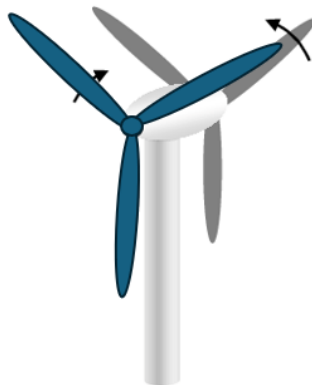


**Figure 1.4:** Dual-rotating wind turbine with identical rotor diameters mounted on either side of the nacelle used for present study

## 1.1 Literature Review

This section provides an overview of previous research on dual-rotor wind turbine performance, where the downwind rotor is either a CO-RWT or CR-RWT. Researchers have conducted empirical, analytical, and CFD assessments to examine performance. Using scaled models in wind tunnels and real-world experiments, these studies have validated theoretical and computational predictions while providing practical insights. To evaluate performance, researchers considered parameters affecting power production and made assumptions to simplify computations. The following sections outline the work of previous researchers based on the assessment approaches they employed.

### 1.1.1 Analytical and Semi-Analytical Approaches

To compute the power extracted by rotors in single or dual configurations, analytical methods such as linear momentum theory, semi-analytical methods like the quasi-strip method, and commonly used engineering tools like the Blade Element Momentum (BEM) method are employed. The BEM combines momentum theory and blade element theory.

An extended linear momentum theory to analyze the power extraction of dual-rotor wind turbines with equal-sized rotors is used by SundarRaju et al. [13]. The rotors were modeled as two separate actuator discs, with the rear rotor enclosed within the inner stream tube of the front rotor, as shown in Figure 1.5. The interaction between the front and rear rotors was included in the analysis. Axial thrusts were calculated and used as inputs for CFD simulations to evaluate the flow characteristics across the rotors. The results demonstrated that the total power coefficient is related to rotor separation, with a maximum coefficient of 0.814 achieved at a separation distance of 2.8 times the rotor diameter.

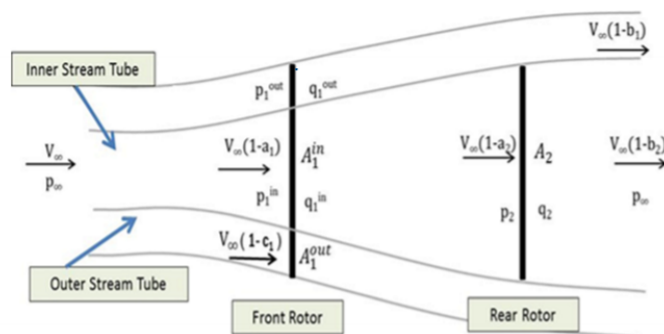


**Figure 1.5:** Dual rotor actuator disc model [13]

S. N. Jung et al.[14] predicted the performance of a 30 kW CR-RWT under uniform airflow conditions using quasi-steady strip theory, examining optimal configurations without aerodynamic interference. Results showed that higher performance when the downwind rotor diameter is less than half the upwind rotor's diameter, with the best distance between the rotor at half the downwind diameter.

Blade element momentum theory is a widely used engineering tool for modeling and optimizing the performance of dual-rotor wind turbines. BEM combines momentum theory with blade element theory to predict forces on each blade section, providing insights into how design parameters, such as pitch angles and rotor speeds, influence overall turbine performance. By assuming steady-state flow and uniform wind conditions, BEM is used for preliminary design and optimization and is also computationally less intensive.

To adapt BEM for dual-rotor systems, the standard BEM model is modified under various assumptions to simplify the computation of dual-rotor performance. For instance, S. Lee et al. [15] used BEM to study the effects of design parameters on CR-RWT performance. In this analysis, the downwind rotor is assumed to be placed in fully developed flow, as shown in Figure 1.6, with the reduced velocity from the upwind rotor serving as the inflow for the downwind rotor. Additionally, it is assumed that the downwind rotor does not influence the upwind rotor. Under these conditions, optimal combinations of pitch angles, rotor speeds, and radii were studied, demonstrating a significant improvement in power coefficients compared to traditional single-rotor wind turbines.

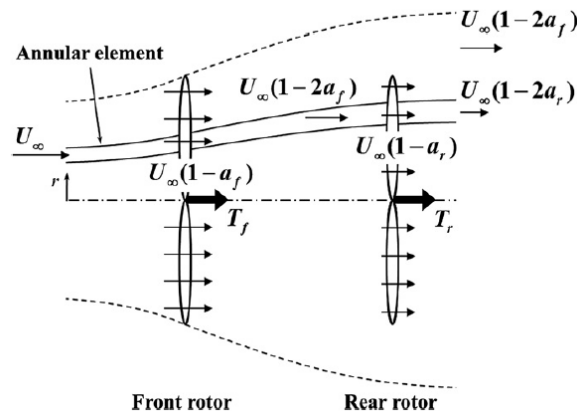


**Figure 1.6:** Inflow for BEMT for CR-RWT with downwind rotor operating inside the stream tube of upwind rotor [15]

However, O. Gur [16] extended traditional BEM models by developing a relationship between induced velocities and downstream distance. This method assumes a rigid wake downstream and was validated against results from the propeller, hovering rotor, and prop-fan experiments. The experiments were conducted on the same blade for single and dual-rotor configurations to isolate the effects of using a dual rotor. The model can also accommodate CR-RWT configurations for more accurate performance predictions.

This modified BEM is further extended to handle CR-RWT dual-rotor configurations by employing an equivalent actuator-disk model, as shown in Figure 1.7. Each disk is treated separately, and the induced velocities  $W_{a,1on2}$ ,  $W_{t,1on2}$ ,  $W_{a,2on1}$ , and  $W_{a,1on1}$  are recalculated until convergence is achieved, typically within a few iterations. The main difference between the modified BEM and the standard BEM is the inclusion of cross-induced velocities between the disks. The upwind disk induces axial and circumferential cross-induced velocities on

the downwind disk, with the downwind disk unaffected by the circumferential cross-induced velocity. This model enables a straightforward estimation of cross-induced velocities in such configurations.

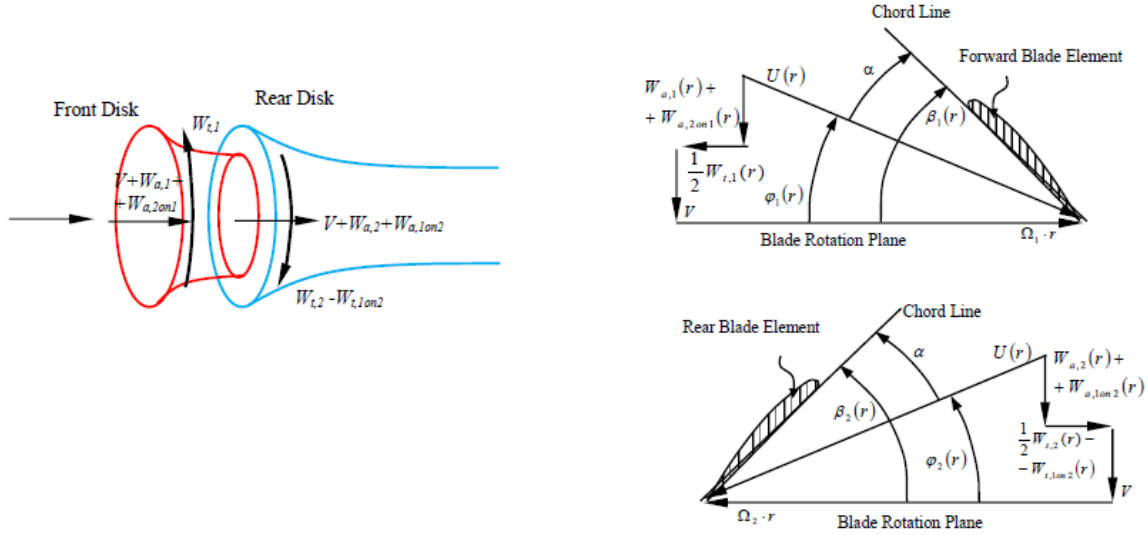


**Figure 1.7:** Actuator disk and blade-element models illustrating the velocity components for CRWT. [16]

## 1.1.2 Computational Fluid Dynamics Simulations

CFD has been widely adopted to simulate and optimize the performance of CR-RWTs, offering detailed insights into aerodynamic interactions, wake behavior, and flow dynamics. CFD simulations enable researchers to examine how design parameters, such as rotor spacing, pitch angles, and diameter ratios, affect CR-RWT efficiency.

For example, W. Z. Shen et al.[7] assessed CR-RWT performance using a modified Actuator Line model (ALM), examining axial rotor distance and rotational speed effects. The author observed that thrust remained constant regardless of rotor spacing, while power efficiency decreased with closer distances. At higher speeds, the downwind rotor's power coefficient dropped, yet overall CR-RWT efficiency nearly doubled compared to a single rotor, with a 43% increase in Annual Energy Production (AEP). The Figure 1.8 shows the comparison of AEP for a SRWT and CRWT

The research by A. Riszal[8] on Tip Speed Ratio (TSR) variations and rotational ratios provides further insight into the aerodynamic performance of CRWTs. Utilizing S826 airfoil models and ANSYS FLUENT for CFD simulations, they found that optimal TSR values and closer rotor distances enhance rear rotor power generation, driven by inflow angles and flow separation dynamics that affect lift and drag forces.

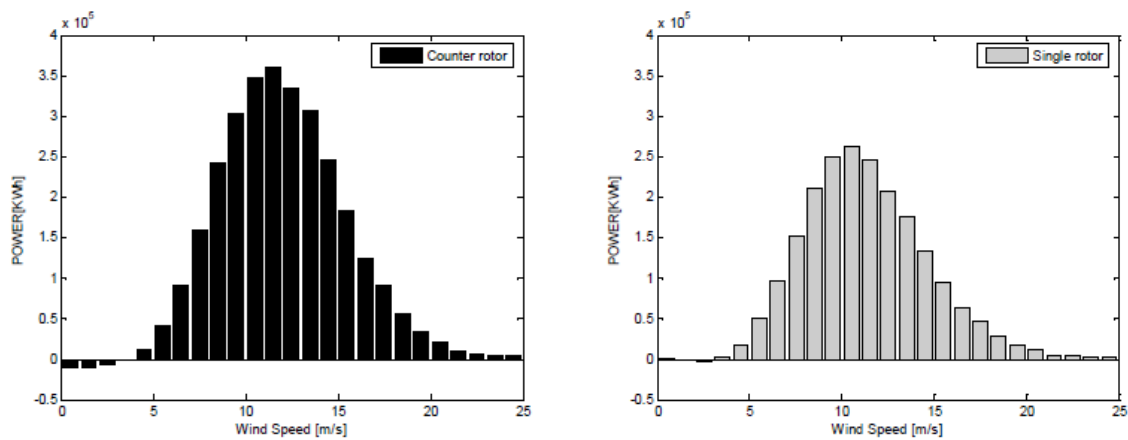


**Figure 1.8:** Comparing AEP of CRWT and SRWT (located in the island of Sprogø, Denmark) [7]

Santhana Kumar et al.[17] used CFD to simulate and compare CR-RWTs and single-rotors, finding a 10% increase in power output for CR-RWT at an optimal axial distance of 0.65 times the primary rotor diameter. V. A. Koehuan et al.[5] employed CFD with  $k - \epsilon$  turbulence modeling and hexahedral meshing, Figure 1.9 shows the mesh in the domain and mesh on the blade surface. The rotor diameter ratio ( $D_1/D_2$ ) of 1.0 provided optimal CR-RWT performance, with significant power coefficient improvements over single-rotor setups. Their study also showed that performance stability was achieved at an axial distance ratio ( $Z/D_1$ ) of 0.5, confirming the role of rotor spacing in maximizing power efficiency Figure 1.10 shows the normalized power coefficient values.

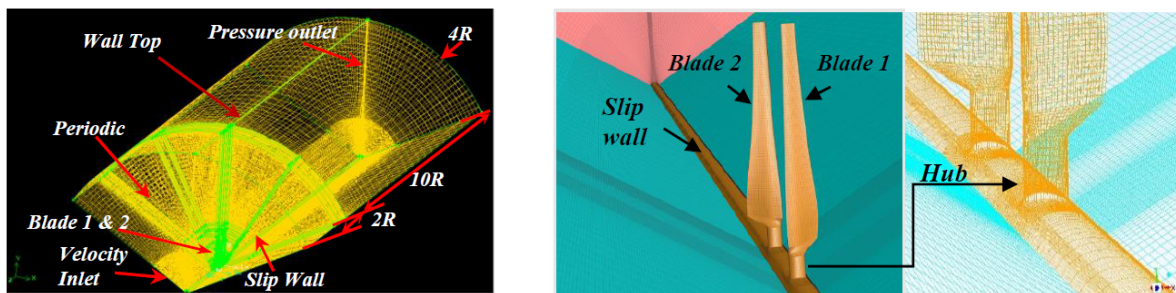


**Figure 1.9:** Mesh in the domain (Left), surface mesh on the blade surface for counter-rotating wind turbine [5]

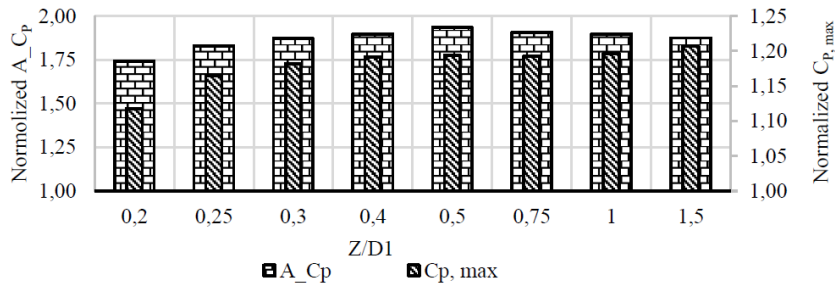


**Figure 1.10:** Increase in normalized maximum power coefficient and the normalization of total power coefficient for CRWT against SRWT according to rotor axial distance ratio with diameter ratio  $D1/D2 = 1.0$ . [5]

Other researchers have focused on extending traditional CFD models to analyze dual-rotor configurations. M. Pacholczyk et al.[18] conducted a parametric CFD study on small CR-RWTs, examining the effects of rotor axial distances ranging from  $0.1D$  to  $1D$  on performance. Their findings indicate that CR-RWTs generally outperform single-rotor, with optimal power gains at a distance of  $1D$ . Similarly, H. Sundararaju et al.[13] used CFD to study airflow patterns around dual-rotor configurations, finding the relationship between the total power and the rotor spacing .

S Bian et al. [19] investigated the aerodynamic performance and wake dynamics of co-axial multi-rotor wind turbines using CFD and the ALM with Large Eddy Simulation (LES). The study focuses on CO-RWT and CR-RWT co-axial configurations, analyzing the effects of rotor interactions on aerodynamic efficiency and wake recovery. The Figure 1.11 shows the different configurations considered for the study. The results indicate that CO-RWT improves aerodynamic performance by enhancing wake recovery while CR-RWT configurations cause periodic torque fluctuations due to wake interference.

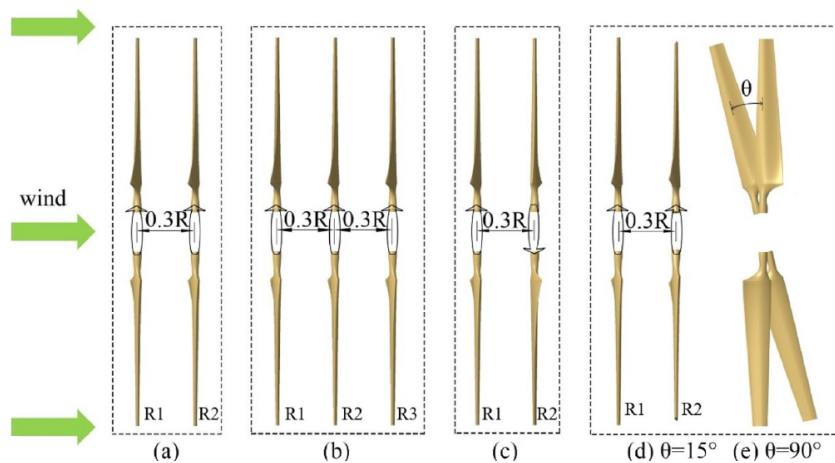


**Figure 1.11:** a.CO-RWT dual rotors, b.CO-RWT tri-rotors c. CR-RWT dual rotor d.c with a  $15^\circ$  phase difference e.CR-RWT dual rotor with phase-difference of  $90^\circ$  [19]

The Figure 1.12 shows the comparison of the wake recovery downstream for single, CO-RWT dual, CO-RWT tri-rotors, and CR-RWT dual rotors The study finds that a rotor distance ex-

ceeding 0.5 times the rotor radius ( $0.5R$ ) minimizes the downwind rotor's impact on the upwind rotor, and specific azimuth angles help optimize performance. This research demonstrates that co-axial MRWTs can provide increased power density with a reduced spatial footprint, making them suitable for offshore wind applications.

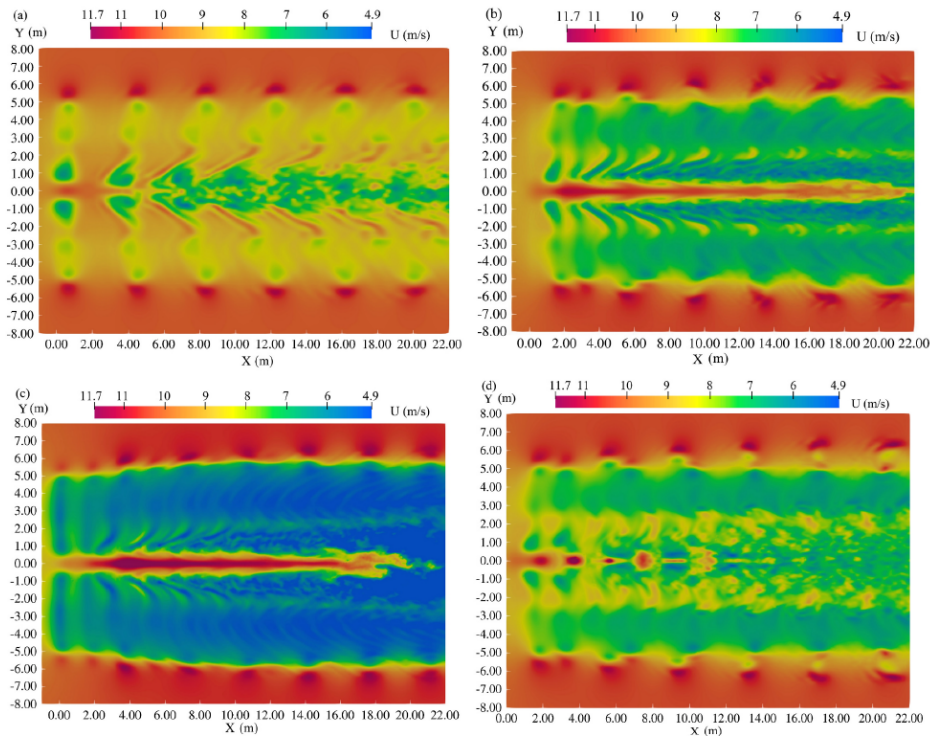


**Figure 1.12:** Velocity contours downstream for a. single rotor case, b. co-rotating dual rotor, c. Three rotor co-rotating d. counter-rotating wind turbines. [19]

### 1.1.3 Experimental and Wind Tunnel Studies

Empirical studies further support the benefits of CR-RWTs. Wang et al. [20] experimentally studied CR-RWT tidal turbines, demonstrating that optimized rotor spacing and blade pitch angles result in higher power coefficients, highlighting CR-RWT adaptability across various environments. Similarly, Ushiyama et al. [21] conducted experiments on dual-rotor wind turbines and found that CR-RWT achieves superior power coefficients compared to both the co-axial dual-rotor and single-rotor turbines, with optimal performance observed in specific diameter and spacing configurations.

These empirical results align with CFD findings, indicating that CR-RWT dual-rotor configurations can increase power output by 7% to 12% over traditional single-rotor designs [22, 20]. Furthermore, comparisons with CO-RWT configurations suggest that CR-RWT designs achieve up to 20% higher energy output [23, 24].

Additional insights into dual-rotor wind turbine performance come from E. Erturk et al. [25], who investigated a dual-rotor wind turbine model under simulated wind conditions. Their study

demonstrated a 20% increase in power output compared to a single-rotor configuration. By incorporating local wind data, the study estimated that dual-rotor wind turbines could generate 22% more annual electricity than single-rotor systems. While DRWTs have approximately 10% higher initial costs, their enhanced efficiency results in a significantly shorter payback period. These findings underscore the potential of DRWTs for sustainable energy production. The dual-rotor demonstration model is illustrated in Figure 1.13.

Growing interest in co-axial dual-rotor wind turbines has led to the development of larger prototypes by the wind energy industry. In May 2023, Huaneng successfully demonstrated a 2.7 MW twin-rotor wind turbine, named "Sairui," in China, marking a significant advancement in multi-rotor wind turbine (MRWT) technology [26], as shown in Figure 1.14.

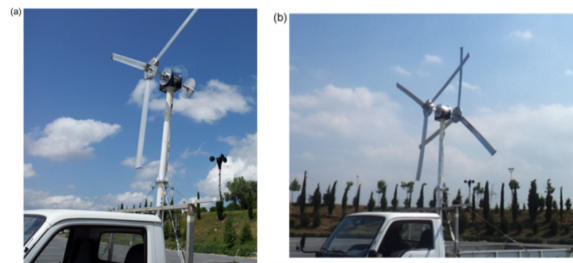


**Figure 1.13:** Dual rotor experimental setup



**Figure 1.14:** Dual rotor Sairui [26]

## 1.1.4 Summary

The reviewed literature consistently indicates that dual rotors can outperform traditional single rotors by effectively utilizing wake energy. Through empirical assessments, analytical modeling, and CFD simulations, researchers have developed an understanding of how to optimize CO-RWT and CR-RWT configurations for maximum efficiency. These findings suggest that the CR-RWT configuration captures the maximum increase in power. Further research, particularly involving hybrid approaches that combine CFD, BEM, and experimental data, will be crucial for refining dual-rotor designs and expanding their applicability across various wind and landscape conditions. The Table 1.1 summaries different approaches and outcomes.

**Table 1.1:** Summary of dual-rotor research grouped by approach with Power output

| Approach  | Focus   | Key Findings  | Power Output  |
|---|---|---|---|
| <b>Blade Element Momentum (BEM) and Variants</b><br>[18] [15] [22]      | <ul style="list-style-type: none"> <li>-Wind turbines with configurable dual rotors arranged in co-rotating and counter-rotating format.</li> <li>-How design parameters such as pitch angle and rotor speed influence outcomes.</li> <li>-Investigating blade pitch and rotor spacing for tidal turbines.</li> </ul>                   | <ul style="list-style-type: none"> <li>- The power coefficients were higher by 10.6% for counter-rotating arrangements than for single rotors and were also higher by 4.6% than for co-rotating arrangements.</li> <li>-The performance improved markedly when the pitch angles and rotor speeds were optimal.</li> <li>- Better angular positioning and spacing resulted in higher power coefficients.</li> </ul>                            | 10%-11% (depending on design parameters)  |
| <b>Analytical and Vortex-Based Methods</b> Papers 2, 9, 14, 16 [7] [16] | <ul style="list-style-type: none"> <li>-Use vortex lattice modeling and generalized analytical methods for the simplified modeling of dual-rotor wind turbines.</li> <li>- Perform a preliminary design dual-rotor wind turbine system using extended blade-element techniques for the modeling of a contra-rotating system.</li> </ul> | <ul style="list-style-type: none"> <li>-Rapid and efficient analytical methods provided predictions that were computationally straightforward.</li> <li>- Models that use vortex lattices and enhanced blade-element theory agreed with results from our experiments and those from CFD studies.</li> <li>- Accurate simulations allowed us to perform optimization with far greater ease than when using the experimental method.</li> </ul> | Improved efficiency validated with experimental data (exact gain not quantified). |
| <b>CFD Methods</b> Papers 6, 7, 11, 15                                  | <ul style="list-style-type: none"> <li>- The CRWT's performance is optimized while varying rotor spacing, tip speed ratio, and axial distance.</li> <li>- Wake recovery and turbulent flow scenario analysis.</li> <li>- Confirmation through comparison with experimental data and data from the wind tunnel.</li> </ul>               | <ul style="list-style-type: none"> <li>- CRWTs demonstrated efficiencies as much as 19.37% greater than those of single-rotor systems.</li> <li>- Optimal axial spacing (0.65 times rotor diameter) improved power output by 10%.</li> <li>- Simulated performance correlated strongly with experimental data, providing confidence in the aerodynamic predictions.</li> </ul>  | 10%-19% (depending on configuration and spacing)                                  |
| <b>Hybrid Approaches (CFD + Actuator/Analytical)</b> Papers 4, 5, 10    | <ul style="list-style-type: none"> <li>- Merged computational fluid dynamics with actuator disc and line methods.</li> <li>- Analyzed counter-rotating wind turbine performance in turbulent conditions.</li> <li>- Improved the annual energy production estimate using hybrid simulations.</li> </ul>                                 | <ul style="list-style-type: none"> <li>-Detailed flow characteristics are captured well by actuator disc and hybrid CFD methods.</li> <li>- CRWTs produced 43.5% more annual energy than single-rotor setups.</li> </ul>  | Up to 20% (annual production improvements)  |
| <b>Experimental and Wind Tunnel Studies</b> Papers 7, 13                | <ul style="list-style-type: none"> <li>- Confirming the aerodynamic and wake performance of CRWTs.</li> <li>- The influence of the recovery of the wake on the arrangement of wind farm components.</li> </ul>  | -In contrast to single rotors, counter-rotating setups achieved 7.2% greater power coefficients and superior wake recovery.   | 7.2%-20% (depending on experimental configuration)                                |

## 1.2 Research Gap

As discussed in Section 1.1 section, various approaches are employed to investigate the efficiency of dual rotors in both CO-RWT and CR-RWT configurations. However, there are notable gaps in the research, particularly for the rotors with the same diameter. The effect of the upwind induction factor on the total power of the dual-rotor wind turbine. The influence of key parameters such as TSR, and pitch angles on the performance. A systematic parametric study varying rotational direction, TSR, pitch angle for upwind rotor and the influence on the downwind rotor.

## 1.3 Research Questions

The current work focuses on the aerodynamic performance of the dual-rotor configurations. Both the rotors are placed on the same axis on either side of the nacelle hub. The rotors are of the same diameter and blade geometry. The primary objective is to investigate the influence of the upwind rotor's induction factor on the total power generated. Furthermore, it involves identifying the parameters significantly impacting the dual-rotor wind turbine efficiency. A systematic computation of the performance of the dual-rotor configuration is conducted by varying the key parameters: upwind rotor loading, rotation direction, rotor spacing, rotational speed, and pitch angles. The objective can be further divided into the following questions:

**Research Question 1:** How do the loading, induction effects, and design parameters of a dual-rotor wind turbine influence its overall efficiency and performance?

- **Sub-question 1.1:** How does the axial and tangential loading, along with the induction effects of the upwind rotor, impact the aerodynamic performance and power output of the downwind rotor?
- **Sub-question 1.2:** Which design parameters, including rotor spacing, blade pitch angle, rotational speed, and loading distribution between the upwind and downwind rotors, have the most significant influence on turbine efficiency?
- **Sub-question 1.3:** What are the optimal values for rotor spacing, pitch angle, rotational speed, and loading distribution that maximize the aerodynamic efficiency and power generation?

**Research Question 2:** How does the performance of a CO-RWT dual-rotor wind turbine compare to that of a CR-RWT variant?

- **Sub-question 2.1:** In terms of aerodynamic efficiency, how does the CR-RWT design compare to the CO-RWT design under similar loading and operating conditions?
- **Sub-question 2.2:** How do the variations in key parameters such as rotor spacing and rotational speed affect the performance of the CO-RWT and CR-RWT configurations?

## 1.4 Thesis Outline

The thesis is organized to systematically explore the design and performance optimization of dual-rotor wind turbines. chapter 1 introduces the increasing demand for innovative solutions in wind energy, driven by the need to meet global renewable energy targets. Notably, there has been a 50% increase in wind energy installations over the previous year, underscoring the urgency for efficient wind power technology. This chapter highlights the potential of dual-rotors to extract higher power than the conventional designs. Following this, an extensive literature review establishes the current state of knowledge in the field, identifies gaps in research, and formulates the primary research questions that this thesis will address.

chapter 2 delves into the state-of-the-art methodologies used to assess single-rotor performance and adaptations required for dual-rotor configurations. Analytical and semi-analytical methods are reviewed, covering foundational theories like 1-D momentum theory, actuator disc theory, and blade element momentum theory. This chapter also explains modifications applied to the BEM approach, which enables it to evaluate dual-rotor configurations and consider the effects of rotor rotation on performance. These methods serve as the theoretical foundation for the research.

chapter 3 outlines the methodology implemented in this study. It details the evaluation of single-rotor performance and the calculation of near-wake velocity deficit using Wilson's velocity model. The dual-rotor setup is introduced here, with assumptions regarding wake structure for both CO-RWT and CR-RWT configurations. Additionally, this chapter covers the setup of Actuator Disc Model (ADM) simulations, which are used to validate BEM results and analyze variations in near-wake velocity, establishing a robust approach for simulating dual-rotor performance.

In chapter 4, the performance of the reference (DTU 10MW) wind turbine is assessed. The chapter provides a detailed examination of optimal operating conditions to achieve the maximum power coefficient ( $C_{Pmax}$ ) and discusses the impact of blade pitch adjustments on turbine performance. The Annual Energy Production (AEP) of the turbine is also calculated, verifying the accuracy and reliability of the BEM method through comparison with established data.

chapter 5 shifts the focus to dual-rotor performance without considering rotation effects. It begins with calculating the downstream velocity deficit based on the thrust coefficient ( $C_T$ ) of the upwind rotor. Using this reduced velocity, the performance of the dual-rotor configuration is computed, and optimal operating conditions are determined. The BEM results for dual-rotor configurations are validated by comparing them to the DTU 10MW report and ADM simulation data, providing a robust foundation for understanding dual-rotor performance.

Following this validation, chapter 6 investigates the performance of both CO-RWT and CR-RWT dual-rotor configurations. This chapter builds on ADM findings to examine the velocity deficit in the wake of the upwind rotor. The analysis focuses on key parameters such as rotor spacing, pitch angle, and rotation direction, evaluating their influence on the overall performance of the dual-rotor system. This exploration provides insights into the aerodynamic interactions within dual-rotor setups and identifies configurations that enhance energy extraction.

Finally, chapter 7 concludes the thesis by summarizing the research findings and addressing the primary research questions. The chapter discusses the implications of the results for the design and operation of CR-RWTs and highlights areas for future research. This includes recommendations for further optimizing CR-RWT efficiency and refining computational models to better capture complex aerodynamic phenomena.

# CHAPTER 2

## State of the Art

This chapter provides a brief overview of the theory behind various analytical and computational models used to analyze single- and dual-rotor configurations.

### 2.1 Analytical and Semi-Analytical Methods

Analytical and semi-analytical methods are essential tools in the study and optimization of Horizontal Axis Wind Turbines (HAWTs), providing efficient solutions for predicting aerodynamic performance, wake interactions, and rotor dynamics. Methods such as BEM theory and ADM allow for fast estimations of key parameters like power output, thrust, and torque, facilitating design and optimization without the high computational costs of full-scale simulations. Recent advancements have addressed limitations in these models, incorporating corrections for effects like unsteady flow, tip losses, and yawed conditions, and leading to hybrid models that balance accuracy with computational efficiency. This section reviews the state-of-the-art analytical and semi-analytical approaches in HAWT analysis, highlighting their theoretical foundations, practical applications, and recent developments in wind turbine technology.

#### 2.1.1 1-D Momentum Theory

1-D momentum theory is a fundamental analytical approach used to predict the maximum theoretical power coefficient of a HAWT. In this model, the turbine rotor is represented as an infinitely thin, permeable disk with no frictional losses, and it is assumed that the flow is incompressible and inviscid. The rotor acts as a drag device that imparts a thrust force to the airflow, resulting in a decrease in the flow's momentum as it passes through the rotor plane.

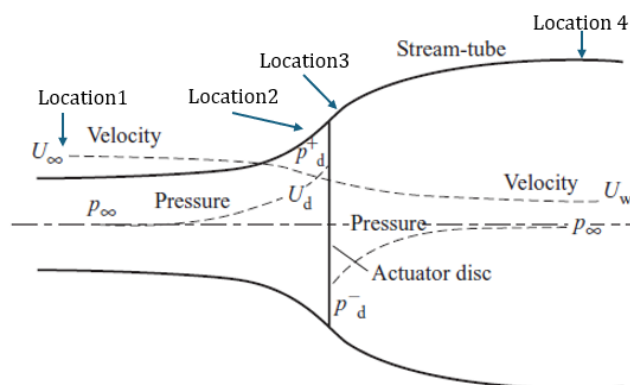


**Figure 2.1:** Illustration of a 1-D Streamtube

To analyze the flow through the rotor, a streamtube is defined that encompasses the mass flow through the rotor plane as shown in Figure 2.1. This streamtube is divided into four locations: Location 1 represents the free-stream conditions at the entrance, Location 2 is immediately upstream of the rotor disk, Location 3 is immediately downstream of the rotor disk, and Location 4 represents the flow far downstream after it has stabilized. The thrust force  $T$  exerted by the rotor on the wind can be expressed as the pressure difference across the rotor disk, multiplied by the area of the disk  $A_d$ , as follows:

$$T = (P_2 - P_3)A_d, \quad (2.1)$$

where the area of the rotor disk  $A_d$  is given by

$$A_d = \pi R^2, \quad (2.2)$$

with  $R$  representing the radius of the rotor.

Under the assumptions of steady, incompressible, and inviscid flow, and with the applied thrust at the rotor plane, conservation principles of mass, momentum, and energy apply. The conservation of mass implies that the mass flow rate must remain constant through the streamtube, leading to:

$$\dot{m} = \rho U_\infty A_1 = \rho U_d A_d = \rho U_4 A_4, \quad (2.3)$$

where  $\rho$  is the air density,  $U_\infty$  is the free-stream velocity,  $U_d$  is the velocity at the disk, and  $A_1$ ,  $A_d$ , and  $A_4$  are the cross-sectional areas at the respective points.

Applying the principle of momentum conservation, the thrust  $T$  can also be described as:

$$T = \rho U_d A_d (U_\infty - U_4) = (P_2 - P_3)A_d. \quad (2.4)$$

For energy conservation, Bernoulli's equation is applied upstream and downstream of the rotor, assuming no energy losses across the rotor plane:

$$P_\infty + \frac{1}{2}\rho U_\infty^2 = P_2 + \frac{1}{2}\rho U_d^2, \quad (2.5)$$

$$P_3 + \frac{1}{2}\rho U_d^2 = P_4 + \frac{1}{2}\rho U_4^2. \quad (2.6)$$

To quantify the reduction in wind velocity caused by the rotor, the axial induction factor  $a$  is defined as the fractional reduction in the wind speed from the free stream to the rotor plane:

$$a = \frac{U_\infty - U_d}{U_\infty}. \quad (2.7)$$

Using this factor, the velocities at the rotor plane and far downstream can be written as  $U_d = U_\infty(1 - a)$  and  $U_4 = U_\infty(1 - 2a)$ , respectively.

With these expressions, the non-dimensional thrust coefficient  $C_T$  and power coefficient  $C_P$  can be derived as functions of the axial induction factor  $a$ . The thrust coefficient, representing the ratio of the thrust to the dynamic pressure force over the rotor area, is given by:

$$C_T = \frac{T}{\frac{1}{2}\rho U_\infty^2 A_d} = 4a(1 - a). \quad (2.8)$$

Similarly, the power coefficient  $C_P$ , which quantifies the efficiency of power extraction by the rotor, is expressed as:

$$C_P = \frac{P}{\frac{1}{2}\rho U_\infty^3 A_d} = 4a(1-a)^2. \quad (2.9)$$

#### Maximum power coefficient for single-rotor

To determine the maximum power coefficient, we differentiate  $C_P$  with respect to  $a$  and set the derivative to zero:

$$\frac{dC_P}{da} = 4(1-a)(1-3a). \quad (2.10)$$

Solving  $\frac{dC_P}{da} = 0$  gives the optimal induction factor  $a = \frac{1}{3}$ . Substituting this value into Equation 2.9 yields the maximum power coefficient:

$$C_{P_{\max}} = \frac{16}{27} \approx \mathbf{59\%}. \quad (2.11)$$

This theoretical maximum power coefficient, commonly known as the **Betz Limit**, represents the upper limit for energy extraction from a wind turbine rotor in a 1-D flow scenario. It implies that no single-rotor HAWT can exceed a power coefficient of 16/27 under ideal conditions. However, this limit is based on simplified assumptions, such as the absence of rotational wake losses, which do not fully capture the physical characteristics of actual HAWTs. Real turbines are torque-driven devices, introducing rotation in the wake, a factor not accounted for in the 1-D momentum model.

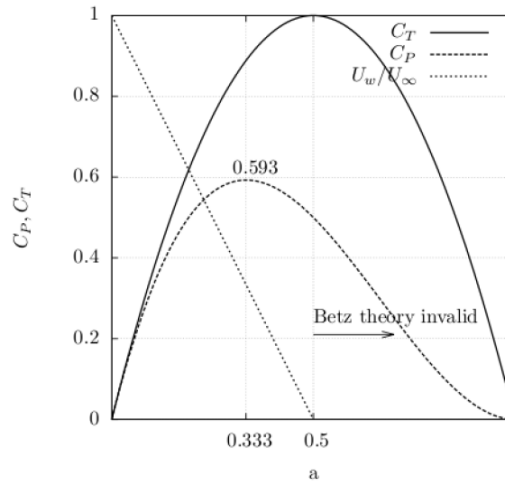


**Figure 2.2:**  $C_P$  and  $C_T$  as functions of axial induction factor  $a$

**Maximum power coefficient for dual-rotors** The dual-rotor configuration, where the second rotor is placed in the wake of the upwind rotor and with the same diameter as shown in Figure 2.3. The total power extracted is given by

$$P = P_1 + P_2 = \frac{1}{2}\rho AV^3 C_{P1} + \frac{1}{2}\rho AV_1^3 C_{P2}, \quad (2.12)$$

where

$$C_{P1} = \frac{P}{\frac{1}{2}\rho AV^3}, \quad C_{P2} = \frac{P}{\frac{1}{2}\rho AV_1^3}. \quad (2.13)$$

The power coefficient is given by:

$$C_P = \frac{P_1 + P_2}{\frac{1}{2}\rho AV^3} = C_{P1} + \left(\frac{V_1}{V_0}\right)^3 C_{P2}. \quad (2.14)$$

Since  $u_1 = \frac{1}{2}(V_0 + V_1) \Rightarrow \frac{V_1}{V_0} = 2u_1 - 1 = 2(1 - a_1) - 1 = 1 - 2a_1$ , we thus get:

$$C_P = C_{P1}(a_1) + (1 - 2a_1)^3 C_{P2}(a_2). \quad (2.15)$$

where,  $a_1$  is the induction factor of turbine 1 and  $a_2$  is for turbine 2. The optimum value of  $C_{P2}$  is  $16/27$ , since  $C_{P2} = C_{P2}(a_2)$ . The optimum value of the total expression is obtained by differentiation:

$$\frac{dC_P}{da_1} = 0. \quad (2.16)$$

Differentiating Eq. (2.15), we get:

$$4(1 - a_1)^2 - 8a_1(1 - a_1) - 6(1 - 2a_1)^2 C_{P2} = 0, \quad (2.17)$$

which simplifies to:

$$6(1 - 2C_{P2})a_1^2 - 4(2 - 3C_{P2})a_1 + (2 - 3C_{P2}) = 0. \quad (2.18)$$

Utilizing  $C_{P2} = 16/27$  and solving for  $a_1$ , we get  $a_1 = 1/5$ . Substituting into Eq. (2.15), we obtain:

$$C_{P1} = 4a_1(1 - a_1)^2 = \frac{64}{125}. \quad (2.19)$$

Thus,

$$C_P = \frac{64}{125} + \left(\frac{3}{5}\right)^3 \frac{16}{27} = \frac{16}{25} = \mathbf{64\%}. \quad (2.20)$$

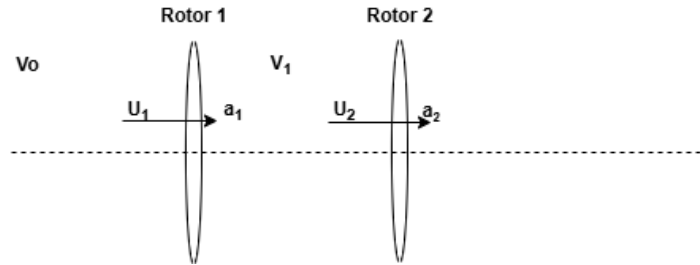


**Figure 2.3:** Dual-rotor setup

Similar to the single rotor, the same assumptions are considered for deriving the maximum power for the dual-rotor. Additionally, the influence of the downwind rotor on the upwind rotor and wake rotation are not considered. Under these simplified conditions, the dual-rotor extracts 64% of power, exceeding the Betz limit

## 2.1.2 Blade Element Momentum Theory for Single-Rotor

The BEM is a classical semi-analytical approach used to predict the performance of propellers, rotor blades, and wind turbines. In this method, the blade is discretized into several small elements along its span, as shown in Figure 2.4. Each blade element is treated independently, assuming that the forces acting on one element do not affect the neighboring elements. This allows for a straightforward calculation of aerodynamic forces on each segment using the local flow conditions and the geometric properties of the blade. BEM combines these aerodynamic forces with the overall rotor geometry to estimate the turbine's performance under various operating conditions.

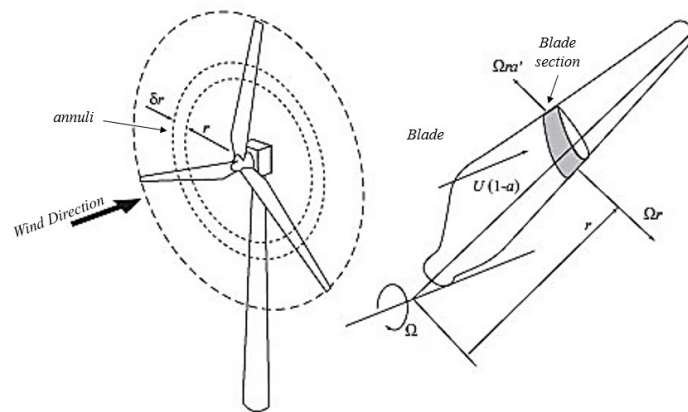


**Figure 2.4:** Blade sections [27]

**Fundamental Principles** BEM operates on two main principles:

- **Blade element theory:** The blade is divided into small sections (or elements), and the forces on each section are calculated independently.
- **Momentum theory:** The overall aerodynamic behavior of the rotor is described by conservation of momentum, particularly the interaction between the rotor and the wind flow, taking into account the induced velocity field.

Each blade element experiences two key aerodynamic forces:

- **Lift:** Perpendicular to the relative wind velocity.
- **Drag:** Parallel to the relative wind velocity.

These forces depend on the local inflow conditions (such as wind speed and rotational velocity), blade geometry, and the angle of attack. The total thrust and torque of the rotor are obtained by integrating these local forces along the blade's span.

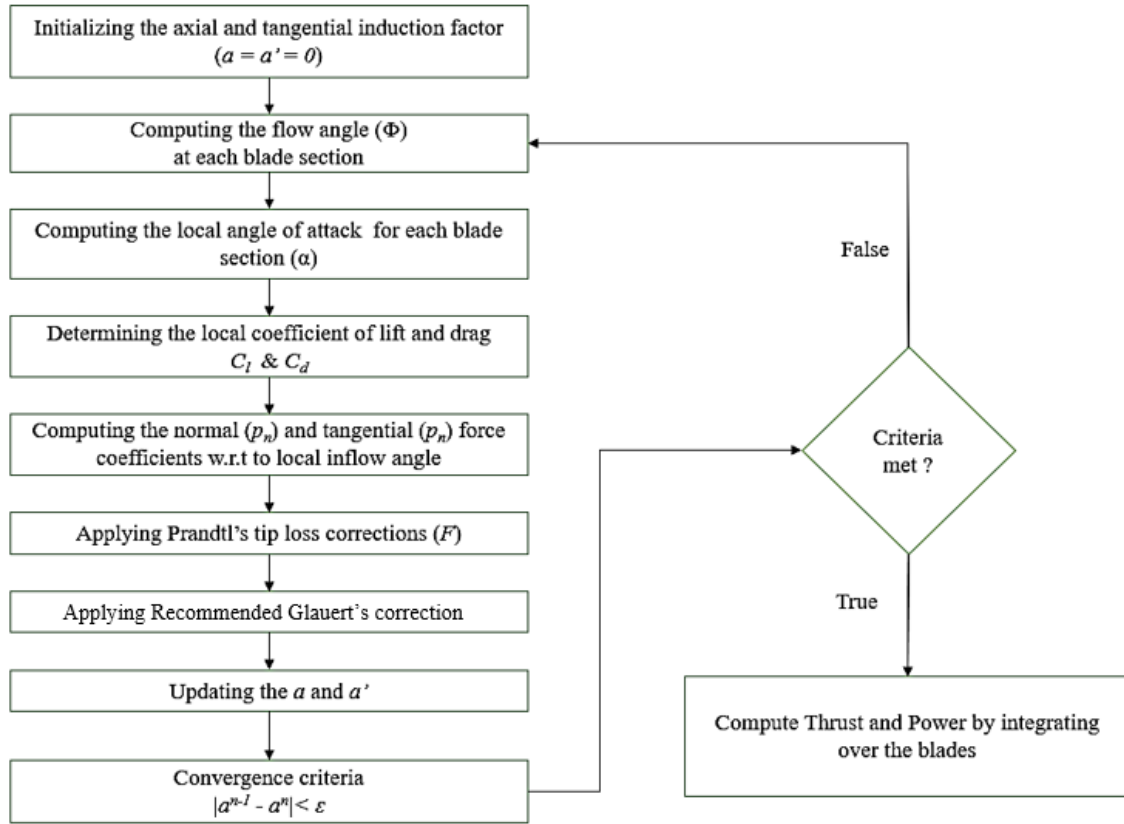


Figure 2.5: BEM flow chart

### Lift and Drag Forces

For a blade element of length  $\Delta r$ , the lift ( $L$ ) and drag ( $D$ ) forces are calculated using the following equations:

$$L = \frac{1}{2} \rho V_{rel}^2 c \Delta r C_L(\alpha) \quad (2.21)$$

$$D = \frac{1}{2} \rho V_{rel}^2 c \Delta r C_D(\alpha) \quad (2.22)$$

where:

- $\rho$  is the air density,
- $V_{rel}$  is the relative wind velocity experienced by the element,
- $c$  is the chord length of the element,
- $C_L$  and  $C_D$  are the lift and drag coefficients, respectively, which are functions of the angle of attack  $\alpha$ .

**Angle of Attack** The angle of attack ( $\alpha$ ) for each blade element is critical for determining the lift and drag forces. It is defined as the angle between the chord line of the blade element and the direction of the relative wind velocity. The angle of attack is calculated as:

$$\alpha = \phi - \theta \quad (2.23)$$

where:

- $\phi$  is the inflow angle, which is the angle between the rotor plane and the relative wind velocity,
- $\theta$  is the pitch angle of the blade element.

**Relative Wind Velocity** The relative wind velocity ( $V_{rel}$ ) experienced by a blade element is the result of the combination of the incoming wind speed and the rotational speed of the rotor. It can be expressed as:

$$V_{rel} = \sqrt{(V_o(1 - a))^2 + (\Omega r(1 + a'))^2} \quad (2.24)$$

where:

- $V_o$  is the freestream velocity,
- $a$  is the axial induction factor (a measure of how much the wind speed slows down as it passes through the rotor),
- $\Omega$  is the angular velocity of the rotor,
- $r$  is the radial distance from the rotor axis,
- $a'$  is the tangential induction factor (related to the induced rotational flow).

**Performance Calculations** The overall performance of the rotor is evaluated by integrating the forces generated by each blade element across the entire span of the blade. Specifically, the thrust ( $T$ ) and torque ( $Q$ ) are calculated by summing the contributions of lift and drag from each element:

$$T = \int_0^R (L \cos(\phi) + D \sin(\phi)) dr \quad (2.25)$$

$$Q = \int_0^R r(L \sin(\phi) - D \cos(\phi)) dr \quad (2.26)$$

where:

- $R$  is the total radius of the rotor,
- $L$  and  $D$  are the lift and drag forces at each blade element,
- $\phi$  is the inflow angle.

By calculating the thrust and torque, the overall performance of the rotor (such as power output and efficiency) can be assessed. These performance metrics are critical for optimizing the rotor design and understanding how different parameters, such as blade geometry and operating conditions, affect overall efficiency.

### 2.1.3 Wake velocity

The wake velocity is influenced by the rotor's induction factors and loading. In the wake region, the axial velocity is reduced compared to the free-stream velocity due to energy extraction by the rotor. This reduction is quantified using the axial induction factor, which represents the fraction of velocity lost as the airflow passes through the rotor disc. Additionally, tangential velocities are introduced in the wake due to the rotational motion of the blades, creating a swirling flow pattern. The velocity deficit and wake rotation collectively impact downstream rotors in dual-rotor configurations, altering their aerodynamic performance.

Calculating the velocity deficit in the wake behind a wind turbine analytically presents several challenges due to the complexity of the fluid dynamics involved. While simplified models, such as the Jensen (Park) wake model, provide a useful framework for estimating wake behavior, they often lack the precision required to capture the flow dynamics accurately. Computational models, such as the ADM, offer significantly better precision.

Actuator disk simulations provide a more detailed and flexible approach to modeling the wake behind wind turbines compared to traditional analytical models. Although analytical models are helpful for quick approximations and insights, they tend to oversimplify the complex physics of wind turbine wakes. In contrast, actuator disk simulations offer a more accurate representation of physical processes by resolving key flow phenomena that are often neglected in analytical approaches. The wake regions can be broadly divided into near-wake and far-wake regions as shown in Figure 2.6. For the current research, the focus is on computing the velocity deficit in the near-wake region. Wilson's velocity [28] equation and O.Gur's [16] velocity equation [16] are used to calculate the velocity in the wake.

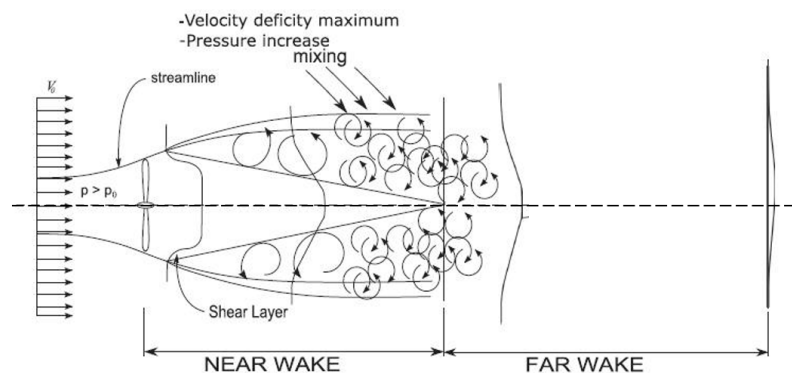


**Figure 2.6:** Wake behind the wind turbine [29]

### 2.1.3.1 Wilson's Velocity Model

For computing the velocity downstream of the upwind rotor, Wilson's velocity equation is used [28]. A simple analytical approximation for the inviscid flow field of a horizontal-axis wind turbine can be developed from actuator-disk theory. Let the mean axial velocity at the rotor be  $u_a = V(1 - a)$  and the mean axial velocity in the far wake be  $u_{FW} = V(1 - 2a)$ . The axial velocity along the axis of a rotor is approximated by

$$u = V \left[ 1 - a - a \frac{\xi}{1 + \xi^2} \right] \quad (2.27)$$

where  $\xi = x/R$  and the rotor is at the origin. Here the rotor radius is  $R$ , the free stream velocity is  $V$ , and the  $x$  direction is measured downstream from the rotor. The above relation is exact for the velocity along the axis of a rotor with a cylindrical vortex sheet wake. The  $a$  is calculated using the Froude's momentum theory [30]

**Froude's actuator disk theory** provides a simple, 1-dimensional approach to the problem of rotor modeling. Assumptions consider an ideal rotor as shown below:

1. 1-Dimensional analysis, and the disk is essentially a discontinuity moving through the fluid.
2. Infinitesimally thin disk of area  $A$ , which offers no resistance to fluid passing through it as frictional forces are negligible compared with momentum flux and pressure changes (hence assumption 5).
3. Thrust loading and velocity are uniform over the disk.
4. Far-field is at free-stream pressure, both far upstream and downstream.
5. Inviscid (thus irrotational), incompressible, and isentropic flow.

Since the disk acts as a drag device, and by assumption 1, the source of drag must be a pressure difference across the disk. This drag manifests itself as thrust loading along the axis normal to the disk. Rewriting the terms of momentum:

$$\sum F_x = \dot{m}(\Delta U) \quad (2.28)$$

A relationship between  $(U_\infty, u_1, u_2)$ , thrust (slowing the fluid), and power may be derived by consideration of the assumptions. Noting that assumption 1 states the disk is a discontinuity and that the flow can be considered stationary, Bernoulli's equation and constant are not valid across the disk, but they may be applied from the far field to the disk in either direction. Placing a control volume around the disk extending far ahead to the free stream and considering that the disk serves to slow down the flow, mass conservation defines streamlines (as the flow slows, conservation dictates the area increases):

Applying Bernoulli in valid regions:

$$p_\infty + \frac{1}{2}\rho U_\infty^2 = p_1 + \frac{1}{2}\rho u_1^2 \quad (2.29)$$

$$p_1 - \Delta p + \frac{1}{2}\rho u_1^2 = p_2 + \frac{1}{2}\rho u_2^2 \quad (2.30)$$

$$\Delta p = \frac{1}{2}\rho(U_\infty^2 - u_2^2) \quad (2.31)$$

Applying the axial momentum equation to a cylindrical control volume (CV) made by rotation of the above control volume about the x-axis:

$$\frac{\partial}{\partial t} \iiint_{CV} \rho \mathbf{v} d\mathbf{v} + \iint_{CS} U \rho \mathbf{v} \cdot d\mathbf{A} = F_{x,t} + F_{press} \quad (2.32)$$

Simplifying this equation by assuming stationary flow (i.e., a moving disk) and noting that pressure forces on the ends of the CV are equal (at  $A_\infty(\rho gh + p_{atm})$ ):

$$\sum F_{press,x} = 0 \quad (2.33)$$

$$\rho u_2^2 A_2 + \rho U_\infty^2 (A_\infty - A_2) + \dot{m}_{side} U_\infty = p_\infty A_\infty U_\infty - \rho A_\infty U_\infty^2 = -T \quad (2.34)$$

Conservation of mass yields the following relationships:

$$\rho A_2 u_2 + \rho (A_\infty - A_2) U_\infty + \dot{m}_{side} = \rho A_\infty U_\infty \quad (2.35)$$

$$p_\infty = p_{atm} + \rho (U_\infty - u_2) \quad (2.36)$$

$$\dot{m}_2 = \rho A_2 u_2 \quad (2.37)$$

Combining with gives the following relationship, as anticipated by (and in the expected form of)

$$T = \rho A_1 A_2 (U_\infty - u_2) = \dot{m} (U_\infty - u_2) \quad (2.38)$$

$$u_1 = \frac{1}{2}(u_1 + u_2) \quad (2.39)$$

Thus, the velocity at the actuator disk is the mean of the freestream and far wake velocities. Redefining the control volume to be coincident with streamlines around the disk, ensuring no mass transfer out of the CV except at the ends (as the fluid flows along streamlines and cannot cross them). The axial momentum equation is thus recast as:

$$T = \rho A_1 A_1 (U_\infty - u_2)^2 + F_{press} \quad (2.40)$$

Since the physics of the situation remains the same, no matter which control volume is used, we declare that the net pressure force on the CV walls that follow streamlines must be zero. By assumption 4, and referring to the new control volume, power is equal to the rate of work, which is itself equal to the rate of momentum transfer through the CV:

$$P = \frac{1}{2}\rho U_\infty^3 A_\infty (1 - a)^2 = P_{atm} - \frac{\rho}{2}(U_\infty^2 - u_2^2) \quad (2.41)$$

Defining an axial induction factor  $a$  and combining leads to the well-known result:

$$u_2 = (1 - 2a)U_\infty \quad (2.42)$$

$$P = 2\rho U_\infty^3 a(1-a)^2 A_1; T = 2\rho U_\infty^2 a(1-a) A_1 \quad (2.43)$$

Defining  $C_P$  as power non-dimensionalized by available power through the disk area, and similarly defining  $C_T$  for thrust:

$$C_P = \frac{P}{\frac{1}{2}\rho U_\infty^3 A_1}; C_T = \frac{T}{\frac{1}{2}\rho U_\infty^2 A_1} \quad (2.44)$$

$$C_P = 4a(1-a)^2; C_T = 4a(1-a) \quad (2.45)$$

The flow induction factor is determined using Equation 2.46.

$$U_\infty = \frac{U_{AD}}{1-a}, \quad a = 0.5 \left(1 - \sqrt{1 - C_T}\right) \quad (2.46)$$

For calculating the inflow axial velocity in the wake, Wilson's equation is used, and the axial induction  $a$  is calculated using the  $C_T$  values of the upstream rotor at optimal conditions. Figure 2.7 shows the normalized axial velocity behind the rotor calculated using Wilson's equation for  $C_T = 0.8$ .

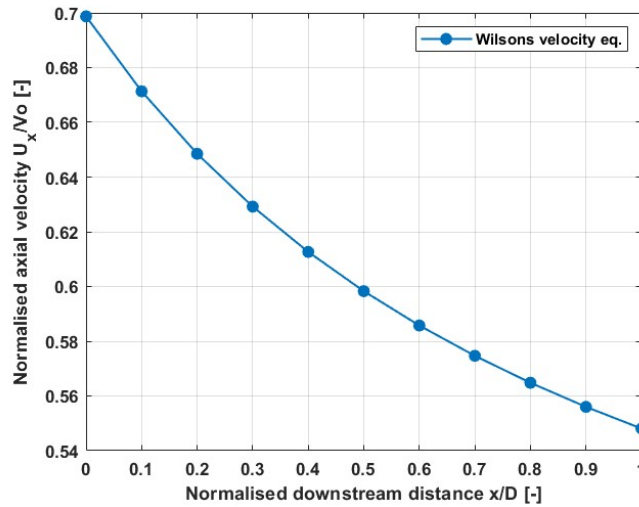


**Figure 2.7:** Normalised wake velocity computed using Wilson's equation for  $C_T = 0.8$

### 2.1.3.2 O.Gur's induced velocity model

To calculate the velocity in the wake, the induction factors of the flow should be computed, based on which the forces on the downwind rotor can be determined. The velocities in the upstream and downstream vary with the distance [16]. In the upstream, the incoming flow is  $V_o$ , which is the freestream velocity. The axial velocity behind the rotor and in the far wake is calculated as  $(1-a)V_o$  and  $(1-2a)V_o$ , respectively. Similarly, the tangential velocity behind the rotor and in the far wake is calculated as  $-a'\Omega r$  and  $-2a'\Omega r$ , respectively, where  $\Omega$  is. Figure 2.8 shows the axial and tangential velocity evolution and the distance coefficient angle. For a downstream distance ( $x$ ), the velocity in the wake can be calculated based on the distance coefficient. The Equation 2.50 is used to calculate the axial and tangential velocity in the

downstream of the upwind rotor. The

$$C_{dist} = 1 + \cos(\theta); 1 + \frac{x}{\sqrt{(x^2 + R^2)}} \quad (2.47)$$

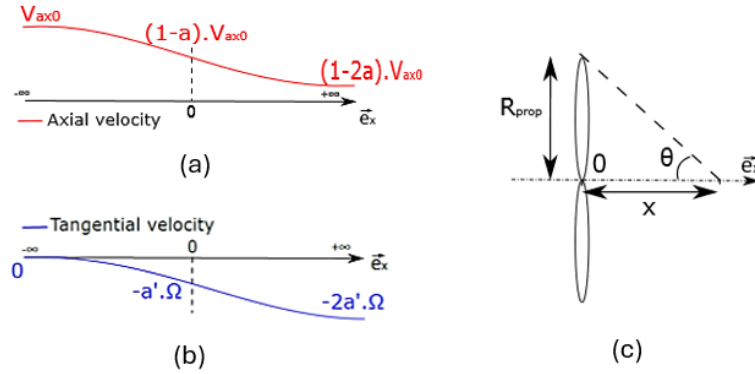


**Figure 2.8:** (a) Axial and (b) Tangential velocity evolution in the downstream (c) Distance coefficient angle [31]

**Axial velocity**

$$V_{ax} = (1 - C_{dist} a) V_o \quad (2.48)$$

**Tangential velocity**

$$V_\theta = -a' \cdot \Omega \cdot r \cdot C_{dist} \quad (2.49)$$

Figure 2.9 shows the comparison of axial velocity variation downstream between Wilson's velocity model and O. Gur's velocity model. The method proposed by O. Gur shows a larger velocity deficit compared to Wilson's. The assumption of linear velocity variation in the wake might be overpredicting the deficit.

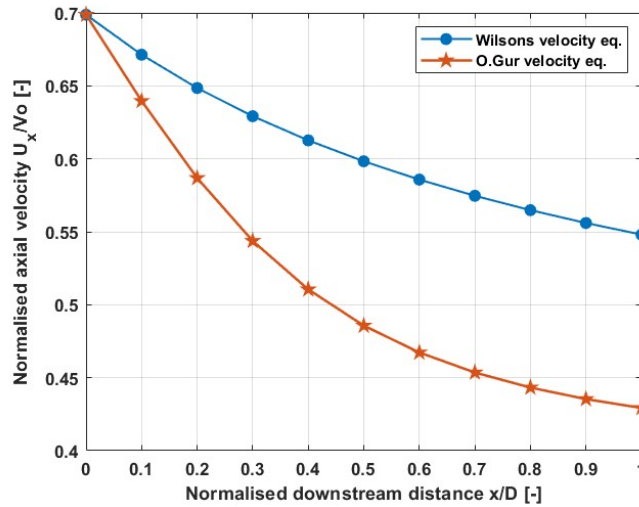


**Figure 2.9:** Normalised wake velocity computed using Wilson's equation for  $C_T = 0.8$

## 2.1.4 Blade Element Method for Dual Rotors

In the case of a dual-rotor wind turbine BEM is applied to both the upwind and downwind rotors. The model assumes inviscid, incompressible flow, steady-state conditions, no interactions from the downwind rotor to the upwind rotor, and neglects radial velocity. For the second rotor, the calculation is similar to the first, with the key difference being the inflow conditions, which are affected by the wake of the upwind rotor and the distance between the two rotors. The presence of the upwind rotor introduces a modified flow field, including a tangential velocity component that does not exist for the upwind rotor. This additional rotational inflow, generated by the wake of the upwind rotor, contributes to the axial deceleration of the wind.

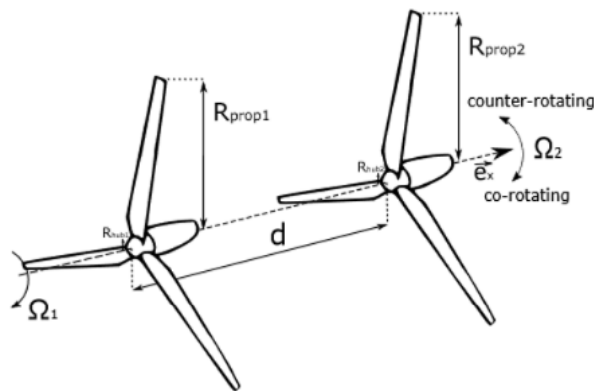


**Figure 2.10:** Dual rotors wind turbine definition

As shown in Figure 2.10, BEM process for the second rotor considers these modified inflow conditions. Here, the variables indexed with "1" correspond to the upwind rotor, while those indexed with "2" refer to the downwind rotor. The second rotor is located at a downstream distance  $x = d$ . The velocity variation is associated with the distance since the upstream

velocity (freestream) is  $V_o$  and the velocity behind the rotor is  $V_o(1 - a)$  and the velocity in the far wake is  $V_o(1 - 2a)$ . The axial velocity and the tangential velocity in the downstream can be calculated based on the distance coefficient as shown in Figure 2.8. Equation 2.50 can be used to calculate the axial and tangential velocity on the second rotor.

$$C_{dist} = 1 + \cos(\theta); \frac{x}{\sqrt{(x^2 + R^2)}} \quad (2.50)$$

- **Axial Flow Velocity:** The wind velocities of the first rotor and the second rotor are as follows:

*Rotor 1:*

$$V_{ax} = (1 - a_1)V_o \quad (2.51)$$

where,  $a_1$  is the axial induction factor for the first rotor,  $V_o$  is freestream velocity and  $V_{ax}$  is the axial velocity for the Rotor1.

*Downstream of the Rotor1:*

$$V_{ax1} = (1 - C_{dist} a_1)V_o \quad (2.52)$$

where,  $C_{dist}$  is the coefficient based on the downstream distance

*Rotor 2:*

$$V_{ax2} = (1 - a_2)V_{ax1} \quad (2.53)$$

where  $a_2$  is the axial induction factor for the second rotor.

- **Tangential Flow Velocity:** Similar to the axial velocity, The flow seen by the second rotor blade in the tangential direction depends on the blade's rotational direction. The tangential velocity includes contributions from the wake of the upwind rotor and the rotation of the second rotor, they are given as follows:

*Rotor1*

$$V_{\theta} = -a'_1 \Omega r \quad (2.54)$$

*Downstream to Rotor1*

$$V_{\theta1} = -a'_1 \cdot \Omega \cdot r \cdot C_{dist} \quad (2.55)$$

*Rotor2*

$$V_{\theta2} = V_{\theta1} + V_{brz2} + V_{ind2} \quad (2.56)$$

where  $V_{brz2} = \Omega_2 r$  is the rotational component of the second rotor, and  $V_{ind2}$  is the induced tangential velocity.

### Counter-Rotating and Co-Rotating Configurations

Two distinct configurations are considered for the second rotor: counter-rotating and co-rotating.

- In the **counter-rotating case**, the blade of the second rotor turns in the opposite direction to the upwind rotor (Figure 2.11). In this case, the tangential wind velocity  $V_{\theta1}$  is aligned with the blade's rotational motion, reducing the effective tangential flow velocity seen by the blade. The relative tangential velocity seen by the second rotor is given by:

$$V_{\theta2}(\text{counter}) = (1 + a'_2)(\Omega_2 r - V_{\theta1}) \quad (2.57)$$

- In the **co-rotating case**, the second rotor rotates in the same direction as the first rotor (Figure 2.12). In this configuration, the tangential wind velocity opposes the rotational movement of the second rotor, increasing the overall tangential inflow velocity:

$$V_{\theta 2}(\text{co}) = (1 + a'_2)(\Omega_2 r + V_{\theta 1}) \quad (2.58)$$

### Performance Calculation for the Dual Rotor System

The fundamental equations of BEM remain unchanged for the second rotor, with the modifications applied only to the inflow wind speed vector (both magnitude and direction). The same BEM procedure used for the first rotor is applied to the second rotor, accounting for the altered inflow conditions due to the wake and rotational effects from the upwind rotor.

The total power produced by the dual-rotor system is the sum of the power generated by the two rotors:

$$P_{\text{turbine tot}} = P_{\text{turbine 1}} + P_{\text{turbine 2}} \quad (2.59)$$

The overall power coefficient  $C_{p_{\text{tot}}}$  is defined as the ratio of the total power extracted by both rotors to the total available wind power:

$$C_{p_{\text{tot}}} = \frac{P_{\text{turbine tot}}}{P_{\text{wind}}} \quad (2.60)$$

This dual-rotor approach captures the interaction effects between the upwind and downwind rotors, allowing for more accurate modeling of rotor performance and aerodynamic efficiency in various configurations.

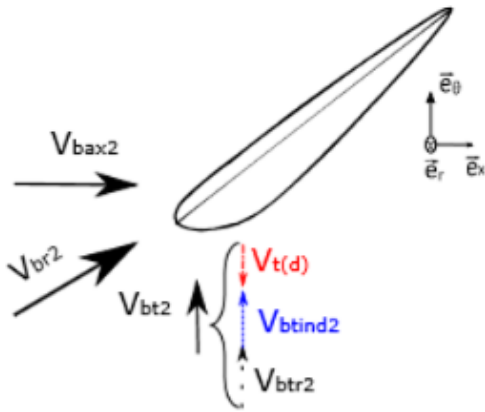


Figure 2.11: Counter-rotating case [31]

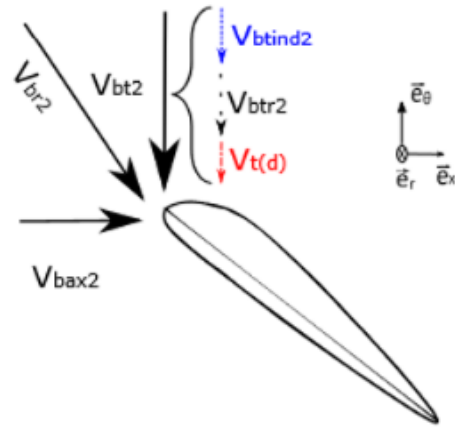


Figure 2.12: Co-rotating case [31]

## 2.2 Computational Methods

Selecting the appropriate models for conducting numerical simulations is crucial to address the research goals mentioned in the previous sections. The BEM model offers detailed performance metrics for each blade segment, including thrust, power, torque, blade loading, and aerodynamic forces. This enables a nuanced understanding of performance across various operating conditions by altering the parameters that influence turbine efficiency. However, computing the aerodynamic interactions between rotors requires a high-fidelity model, for which the Actuator Disk Model is employed. ADM is adept at resolving the aerodynamic interactions between rotors in a dual wind turbine setup. It can simulate wake effects, including velocity deficits and increased turbulence intensity, thus allowing for the analysis of how the upwind rotor's operation impacts the downwind rotor's performance. The Actuator Line Model provides a detailed understanding of the aerodynamic interactions at the blade level. But it is quite computationally intensive.

### 2.2.1 Actuator Disk Model

The Actuator Disk Model (ADM) is a conceptual approach used to represent the impact of a wind turbine on the airflow in simulations. It depicts the turbine as a porous disk (as shown in Figure 2.13) that imparts thrust on the airflow, thereby extracting energy, without the need to physically resolve the blades. It is advantageous in large-scale wind farm simulations where the detailed blade geometry resolution is unnecessary or too costly. It provides a means to capture the essential physics of turbine operation, including wake formation and turbine interactions, which are critical for optimizing farm layouts and turbine designs.

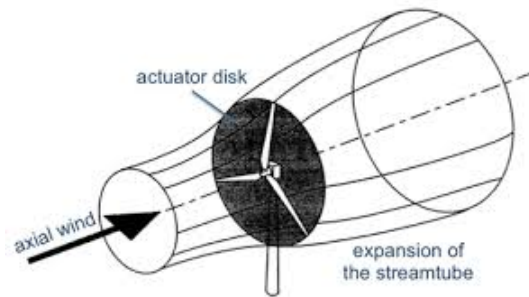


**Figure 2.13:** Actuator disk model [27]

In the ADM, the thrust exerted by the wind turbine and the power extracted are calculated using the following equations:

$$T = \frac{1}{2} \rho A V^2 C_T \quad (2.61)$$

$$P = \frac{1}{2} \rho A V^3 C_P \quad (2.62)$$

where:

- $\rho$  is the air density,
- $A$  is the area of the actuator disk,

- $V$  is the wind speed far upstream of the disk,
- $C_T$  is the thrust coefficient, and
- $C_P$  is the power coefficient.

OpenFOAM incorporates the ADM through source terms in the Navier-Stokes equations. These source terms represent the momentum deficit and energy extraction caused by the wind turbine, defined as:

$$\vec{F}_{ADM} = -\frac{1}{2}\rho AC_T \vec{U}_\infty^2 \delta(\vec{x} - \vec{x}_{disk}) \quad (2.63)$$

$$\dot{W}_{ADM} = -\frac{1}{2}\rho AC_P \vec{U}_\infty^3 \delta(\vec{x} - \vec{x}_{disk}) \quad (2.64)$$

where:

- $\rho$  is the fluid density,
- $A$  is the actuator disk area,
- $C_T$  and  $C_P$  are the thrust and power coefficients, respectively,
- $\vec{U}_\infty$  is the free stream velocity,
- $\delta(\vec{x} - \vec{x}_{disk})$  is the Dirac delta function, ensuring the force is applied only at the disk location.

## 2.3 Uncertainties

When assessing how well the dual-rotor configuration performs, it is absolutely crucial to take into account any uncertainties. This study, grounded in first-order models and concentrated on aerodynamics, accounts for not just one but several aerodynamic losses—many of which are the result of complex interactions between the rotor blades and the airflow. These include swirl loss, tip loss, induction loss, viscous loss, wake loss. Understanding these losses is key not just to turbine performance optimization but also to accurate modeling of rotor aerodynamics.

- **Swirl Loss:** Swirl loss indicates the energy that is not converted into power when a turbine generates electricity. It involves the rotation of the air beyond the turbine, downstream from it. Designers cannot see this effect, which is hard to measure, and they cannot capture the air in wind tunnels to show how it behaves past the blades of a real wind turbine. A turbulent wake cannot transfer useful work to the wind power system. Swirl is one of the first attempts to visualize beyond the blades and past the turbine. Reducing swirl loss, which can be achieved by optimizing blade pitch or adding a counter-rotating rotor, is essential to maximize energy capture.
- **Tip Loss:** Tip loss arises at the blade tips due to pressure equalization between the high-pressure side and low-pressure side of the blade, resulting in a vortex at the tip. This vortex reduces lift, decreasing the energy extracted from the wind. The Prandtl tip loss factor is commonly used in aerodynamic modeling to account for this efficiency loss at the blade tips. Design techniques, such as adding winglets or optimizing taper and

twist distribution, can reduce tip vortex intensity and improve aerodynamic efficiency.

- **Induction Loss:** Induction loss occurs due to the energy expended in accelerating air through the rotor plane. According to momentum theory, the rotor induces a reduction in wind speed as the air passes through the rotor, leading to a loss in available power because not all of the wind's kinetic energy is converted to rotor torque. In an ideal situation, the induction factor maximizes energy extraction up to the Betz limit. However, in the real world, deviations from this optimal induction factor result in induction loss. Dynamic pitch adjustment and control strategies help minimize these losses by keeping the rotor near optimal operating conditions.
- **Viscous Loss:** Drag forces on the blade surfaces as they slice through the air are the cause of viscous loss. This drag comes from the blade surface and the airflow it's supposed to be moving, which, if it were doing so really well, wouldn't be happening at all. The energy that's being dissipated in that very unproductive partnership is being dissipated as heat. Viscous losses are affected mostly by how smooth or rough the blade surface is, the shape of the airfoil, and the Reynolds number associated with the airflow. To reduce the inevitable energy waste that results from these blade/air interactions, designers and maintenance teams can take a couple of different paths.
- **Wake Loss:** Wake loss designates the diminution of wind energy that is available to downstream turbines because of the wake formed by the rotor of an upwind turbine. When a wind turbine array extracts energy from the wind, it reduces the wind speed—not only in the immediate vicinity of the rotor but also in the wake region downstream of the wind turbine. This region extends 5 to 8 rotor diameters downstream of the turbine for the defect itself and, to a finite extent, 2 rotor diameters in the direction perpendicular to the turbine and the flow direction. The wind speed is more or less recovered to the upstream speed at 5 to 8 rotor diameters downstream. If the turbine array is well-spaced, that is. If not, wake mining occurs, with the upwind turbine taking too much energy from the wind.

BEM contains various empirical corrections to handle aerodynamic losses that the basic theory does not fully capture. One of the main corrections is Prandtl's tip loss factor, which compensates for reduced lift near the blade tips due to vortex formation. This tip loss correction helps to ensure that BEM does not overestimate lift in the region of the blade tip. BEM also applies a root loss correction to compensate for reduced lift near the blade root. In neither case does BEM employ a rigorous mathematical treatment; instead, it uses empirical factors to make the theory work better. Similarly, BEM applies **root loss corrections** to account for the diminished lift near the blade root, where the blade geometry is less effective. In conditions of high rotor loading, where the axial induction factor  $a$  can exceed 0.5, BEM employs **Glauert's correction** to adjust the relationship between the thrust coefficient  $C_T$  and the induction factor. This correction prevents overestimation of thrust and power in high-induction scenarios.

Yaw misalignment corrections, such as skewed wake models, are built into BEM to account for power loss and uneven loading when the rotor is not perfectly aligned with the wind. Slower and more regionally gusty winds that change direction (as commonly produced by

thunderstorms) can induce yaw error in a wind turbine and thus power production losses. Some BEM implementations use dynamic stall models to capture unsteady flow effects when wind conditions rapidly change. These model corrections can reduce the impact of transient stall on performance estimates. However, just as with the no-correction assumption, these effects are not corrected for in an overall BEM solution—they are accounted for in the models used to generate the solution.

## 2.4 Parametric Study

A parametric study was conducted to determine the optimal configuration for maximizing efficiency and to assess the impact of specific parameters on turbine performance. The following parameters were varied and analyzed:

- *Axial distance* between the two rotors.
- *Tip-speed ratio* of the downstream rotor.
- *Blade pitch angle*.

By systematically adjusting these parameters, the study aimed to evaluate their influence on the performance of the downstream rotor and to identify the configuration that maximizes energy extraction. The results of this parametric analysis provide valuable insights into the optimal spacing and operational settings for dual-rotor wind turbines, offering a pathway to enhance overall efficiency.

## 2.5 Annual Energy Production

The annual energy production (AEP) of a wind turbine depends on both the turbine's power curve and the wind speed distribution at the site. To estimate the amount of energy captured, the power output is evaluated as a function of wind speed using the turbine's power curve. Wind speed at the location is represented by a Weibull probability density function, which provides the probability that the wind speed lies within a specific range. This distribution is characterized by two parameters: the scale factor  $A$  and the shape factor  $K$ , which may be adjusted to reflect local site conditions [32].

The Weibull distribution for wind speeds  $V_o$  between two values  $V_i$  and  $V_{i+1}$  can be expressed as:

$$h_w(V_o) = \frac{K}{A} \left( \frac{V_o}{A} \right)^{k-1} \exp \left( - \left( \frac{V_o}{A} \right)^k \right), \quad (2.65)$$

where  $h_w(V_o)$  represents the probability density function for wind speeds, allowing for the calculation of the contribution of energy production in each wind speed interval.

The probability  $f(V_i < V_o < V_{i+1})$ , that the wind speed lies within an interval  $[V_i, V_{i+1}]$ , can be determined by:

$$f(V_i < V_o < V_{i+1}) = \exp \left( - \left( \frac{V_i}{A} \right)^k \right) - \exp \left( - \left( \frac{V_{i+1}}{A} \right)^k \right). \quad (2.66)$$

This probability function, as defined in Equation 2.66, is used to plot the Weibull distribution against wind speed, as shown in Figure 2.14. For a site with a scale parameter  $A = 9$  m/s

and shape parameter  $k = 1.9$ , the annual hours associated with each wind speed range can be determined. The total annual energy production (AEP) is computed by summing the contributions across all wind speeds using the formula:

$$\text{AEP} = \sum \frac{1}{2} (P(V_{i+1}) + P(V_i)) f(V_i < V_o < V_{i+1}) \times 8760, \quad (2.67)$$

where  $P(V_i)$  represents the power output at wind speed  $V_i$ , and 8760 denotes the total number of hours in a year.

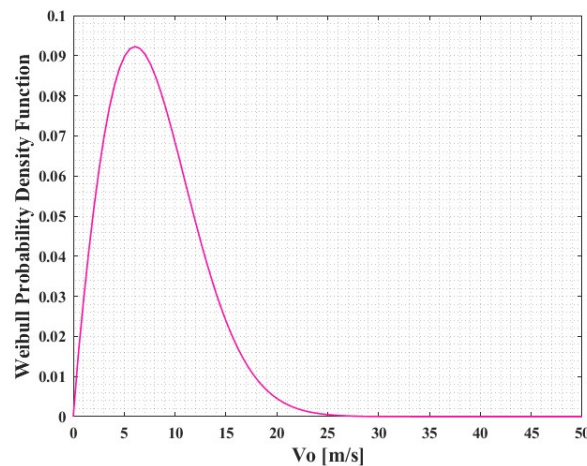


**Figure 2.14:** Weibull probability density function for the wind speed [33]

## 2.6 Summary

This chapter gives an overview of analytical and computational methods used to analyze the performance of wind turbines with either a single rotor or a dual-rotor configuration. It starts off with the analytical approaches, discussing BEM theory, and Actuator Disk Models, which are fundamental tools for calculating the performance of these wind turbine configurations. They allow for interactions between both the wind turbine rotors and the wind itself to be incorporated into the calculations, while still keeping the computational expense low enough that they can be used to simulate large numbers of possible designs. This makes BEM theory and Actuator Disk Models ideal for preliminary design and upscaling analyses. The chapter gives a thorough description of how BEM theory works, using it first to calculate the performance of a single wind turbine rotor, and then moving on to describe how it can be used to calculate the performance of a two-rotor wind turbine system.

The chapter also deals with different types of aerodynamic losses—like swirl, tip, induction, viscous, and wake losses—that can affect rotor efficiency. It then moves on to how BEM corrections (like Prandtl’s tip loss factor and Glauert’s correction) compensate for these aerodynamic losses, bringing the BEM models ever closer to reality. Chapter 4 also lays down the basic ideas behind two advanced computational methods—analytical dynamic modeling and computational fluid dynamics—that offer ways to calculate rotor efficiency in new and complex configurations, especially when two or more rotors are present. This chapter establishes a foundation for evaluating and optimizing advanced rotor configurations in wind turbine design.

# CHAPTER 3

## Methodology

---

This chapter outlines the analytical and CFD models used to compute the performance of single and dual rotors. Additionally, it discusses the models and setup used to determine the performance of the CO-RWT and CR-RWT configurations.

### 3.1 Blade Element Method

The DTU 10MW wind turbine is used as the reference turbine for the current study. Table 3.1 shows the specifications of the reference model.

**Single-Rotor:** The reference model is used to compute the performance and determine the optimal operating conditions across the TSR range of 5 to 14, with pitch angles varying from  $-2^\circ$  to  $5^\circ$ . The cut-in and cut-out wind speeds are set between 4 and 25 m/s. Power and thrust are computed across these ranges and validated by comparing the results with HAWCStab2 results reported for the DTU 10MW report [34].

**Dual-Rotor:** The performance of the dual rotor is computed in combination with the wake model. The downwind rotor is placed in the near wake of the upwind turbine. The following setups and assumptions are used:

1. **No Wake Rotation:** This method calculates only the change in axial velocity along the wake centerline, without considering wake rotation. The axial induction factor in the downstream flow is determined based on the thrust coefficient of the upstream rotor using Equation 2.46. The reduced velocity in the wake is calculated using Equation 2.27, which becomes the new inflow velocity for BEM calculations to determine the performance of the downwind rotor. The velocity deficit varies with the downstream distance, and the reduced velocity is calculated based on the placement of the downwind rotor. The wake interactions between the upwind and downwind rotors are not explicitly calculated. The results from Wilson's velocity model can be compared to O. Gur's [16] model by calculating the velocity deficit in the wake ignoring wake rotations.
2. **Co-Rotating Configuration:** The co-rotating case is modeled as outlined in chapter 2. In this configuration, the near wake is assumed to be rigid, with tangential velocity linearly varying across the rotor radius. These rotational effects are incorporated into the inflow velocity for the downstream rotor.
3. **Counter-Rotating Configuration:** Similar to the co-rotating case, the counter-rotating setup assumes a near-wake model with a linearly varying tangential velocity. These rotational effects are included in the inflow velocity calculations for the downstream rotor, enabling a direct comparison of performance across all three configurations.

Similar to the single-rotor analysis, the performance of the dual-rotor is computed for TSR ranging from 5 to 14, with pitch angles between  $-2^\circ$  and  $5^\circ$ . Additionally, the distance between the rotors is varied at 10%D, 20%D, and 40%D to determine the optimal position.

**Table 3.1:** Specifications of the DTU 10MW [34]

| Parameter               | DTU 10MW                             |
|-------------------------|--------------------------------------|
| Wind Regime             | IEC Class 1A                         |
| Rotor Orientation       | Clockwise rotation - Upwind          |
| Control                 | Variable Speed, Collective Pitch     |
| Cut-in Wind Speed       | 4 m/s                                |
| Cut-out Wind Speed      | 25 m/s                               |
| Rated Wind Speed        | 11.4 m/s                             |
| Rated Power             | 10 MW                                |
| Number of Blades        | 3                                    |
| Rotor Diameter          | 178.3 m                              |
| Hub Diameter            | 5.6 m                                |
| Hub Height              | 119.0 m                              |
| Drivetrain              | Medium Speed, Multiple-Stage Gearbox |
| Minimum Rotor Speed     | 6.0 rpm                              |
| Maximum Rotor Speed     | 9.6 rpm                              |
| Maximum Generator Speed | 480.0 rpm                            |
| Gearbox Ratio           | 50                                   |
| Maximum Tip Speed       | 90.0 m/s                             |
| Hub Overhang            | 7.1 m                                |
| Shaft Tilt Angle        | 5.0 deg                              |
| Rotor Precone Angle     | -2.5 deg                             |
| Blade Prebend           | 3.332 m                              |
| Rotor Mass              | 227,962 kg                           |
| Nacelle Mass            | 446,036 kg                           |
| Tower Mass              | 628,442 kg                           |

## 3.2 Actuator Disc Method

BEM in conjunction with the wake model provides estimates of power output for each configuration, which were then compared to identify the effects of rotation on dual-rotor performance relative to the single-rotor reference model. To achieve more detailed insights into wake interactions that are challenging to capture with analytical methods, ADM simulations were employed. These simulations provide a three-dimensional view of the wake, allowing for a refined analysis of velocity variation, power output, and wake recovery. This approach ensures that the wake effects, including the velocity deficit and turbulence, are accurately accounted for in the performance calculations of both the upwind and downwind rotors.

Firstly, a mesh independence study was conducted to minimize numerical error and identify the optimal mesh configuration for accurately resolving the downstream wake. This study ensures the mesh settings are fine enough to capture the wake's influence on the axial induction

factor for both rotors. The following sections discuss the findings of the mesh sensitivity analysis, which provides the foundation for accurate and consistent ADM simulation results.

### 3.2.1 Mesh Independence Study

To ensure accuracy in actuator disc simulations and minimize numerical errors, a sensitivity study was conducted to examine the effects of mesh refinement, domain size, turbulence intensity, and Reynolds number on induction at the disc. Using the methodology outlined by A.Sala [35], a range of values for each parameter was selected for variation. Actuator disc simulations were performed using OpenFOAM [30], with the DTU 10MW wind turbine as the reference rotor. The mesh independence study identified the optimal mesh size, domain configuration, and turbulence model settings to balance computational efficiency with precision. The following sections describe the parameter studies conducted on the single-rotor reference model.

#### 3.2.1.1 Varying Mesh Size

Mesh size is a critical factor in computational studies as it influences simulation accuracy. Four different cell sizes were tested to calculate the average induction across the disc, and the relative error was compared to the theoretical induction. The cell size was normalized by the rotor diameter  $D$ . A block mesh approach is used for all mesh cases, incorporating multiple refinement boxes. This approach improves convergence, reduces discontinuities in computed values, and enhances the rate of convergence. Figure 3.1 shows the refinement of the fine mesh setup. Table 3.2 summarizes the results for each mesh size. It was observed that a fine mesh provided a lower error percentage and computational cost compared to a super fine mesh, while medium and coarse meshes, although faster, produced higher relative errors. The relative error is calculated using Equation 3.1. For further simulations, fine mesh is used.

$$Relativeerror = \frac{a_{theory} - a_{avg}}{a_{theory}} \cdot 100 \quad (3.1)$$

**Table 3.2:** Mesh size sensitivity analysis

| Mesh        | Cell size $L_{ref}/D$                  | Axial Induction Factor $a_{avg}$ | Relative Error [%] |
|-------------|--|----------------------------------|--------------------|
| Coarse      | $0.1 \times 10^{-2}$                   | 0.2659                           | 13%                |
| Medium      | $0.5 \times 10^{-3}$                   | 0.2787                           | 7.5%               |
| <b>Fine</b> | <b><math>0.5 \times 10^{-4}</math></b> | <b>0.2926</b>                    | <b>2.4%</b>        |
| Super Fine  | $0.5 \times 10^{-5}$                   | 0.2957                           | 1.4%               |

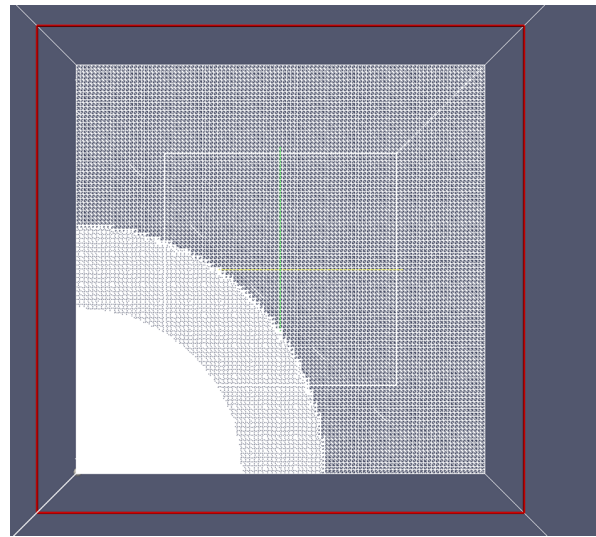


**Figure 3.1:** Mesh refinement for fine mesh

### 3.2.1.2 Varying Domain Size

Using the fine mesh setting, the influence of domain size on simulation results is analyzed. Based on A. Sala's [35] findings, only the upstream distance is varied, while the downstream boundary is fixed at  $10D$  and the lateral extents at  $6D$ . The results indicate a noticeable difference in induction when the upstream boundary is reduced, with a 5% difference observed. However, when the upstream boundary is increased beyond  $10D$ , the difference in induction values becomes negligible, as the flow stabilizes in the upstream region. Therefore for the simulations, the upstream  $10D$  domain length is used.

**Table 3.3:** Domain size sensitivity analysis

| Upstream Domain | Axial Induction Factor $a_{\text{avg}}$ | Relative Error [%] |
|-----------------|---|--------------------|
| 4D              | 0.2585                                  | 13.8%              |
| 6D              | 0.2683                                  | 10.5%              |
| <b>10D</b>      | <b>0.2923</b>                           | <b>2.5%</b>        |
| 12D             | 0.2926                                  | 2.5%               |

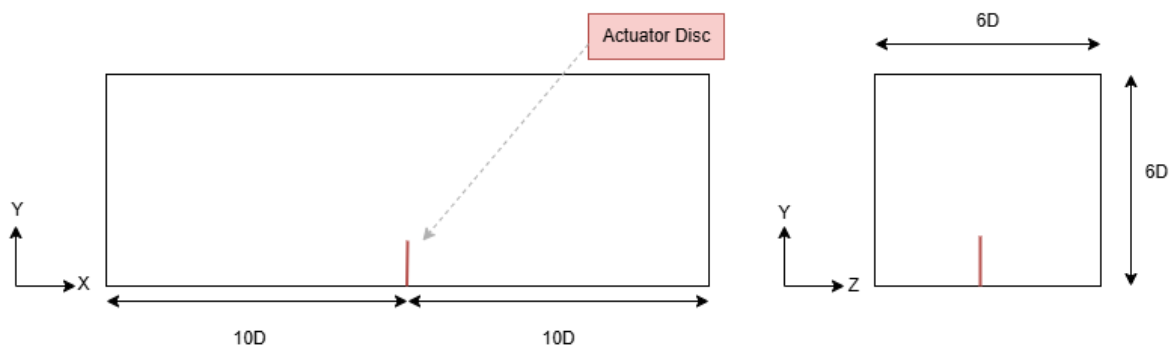


**Figure 3.2:** Final domain size

### 3.2.1.3 Varying Turbulence Intensity

The effect of turbulence intensity is tested using a fine mesh and a domain with a 10D upstream distance. As turbulence intensity increases, the induction factor decreases, consistent across both k-omega and k-epsilon models. Varying the turbulence models shows that the k-omega model yields lower axial induction values. The induction factor values are higher for the k-epsilon model compared to the k-omega SST model. This occurs because the k-epsilon model tends to over-predict turbulence dissipation, resulting in faster wake recovery and a shallower velocity deficit in the near-wake region. This overestimated wake recovery effectively reduces the velocity deficit, leading to an overestimation of the induction factor at the rotor.

In contrast, the k-omega SST model better captures the near-wake effects, providing more accurate predictions of the velocity deficit and turbulent structures. This results in a lower, more realistic induction factor, as the model accounts for slower wake recovery and maintains a stronger velocity deficit closer to the rotor

**Table 3.4:** Turbulence model and intensity sensitivity analysis

| Mesh    | $k - \epsilon a_{\text{avg}}$ | $k - \omega SST a_{\text{avg}}$ | $k - \epsilon$ Relative Error [%] | $k - \omega SST$ Relative Error [%] |
|---------|-------------------------------|---------------------------------|-----------------------------------|-------------------------------------|
| Laminar | 0.2926                        | 0.2582                          | 2.5%                              | 5%                                  |
| 1% TI   | 0.2652                        | 0.2584                          | 11.6%                             | 13.8%                               |
| 3% TI   | 0.2564                        | 0.2528                          | 14.5%                             | 15.7%                               |
| 5% TI   | 0.2518                        | 0.2464                          | 16%                               | 17.8%                               |

### 3.2.1.4 Final Simulation Setup

For final simulations, a fine mesh size with  $0.5 \times 10^{-4}$  and a domain extending 10D upstream and downstream was selected. The k-omega SST model was chosen for its accuracy in capturing turbulent effects. Velocity data was extracted from individual cells, where a discontinuity in velocity near the disc was observed due to the actuator disc model. To address this, linear interpolation was applied to smooth the velocity profile, as shown in Figure 3.3 and Figure 3.4.

The axial induction factor was computed by taking a weighted average as defined in Equation 3.2, and the downstream axial induction was analyzed based on radial distribution, as shown in Figure 3.5.

$$a_{\text{avg}} = \frac{\sum_{i=1}^N a_i \cdot \pi (r_{i+1}^2 - r_i^2)}{\pi D^2 / 4} \quad (3.2)$$

The final mesh configuration, which incorporated refinement zones for smooth transitions, showed strong agreement with theoretical predictions and Glauert's correction for high thrust coefficients as shown in Figure 3.6. These results confirm that the chosen setup effectively captures induction and wake characteristics, validating the model for ADM simulations in wind turbine analysis.

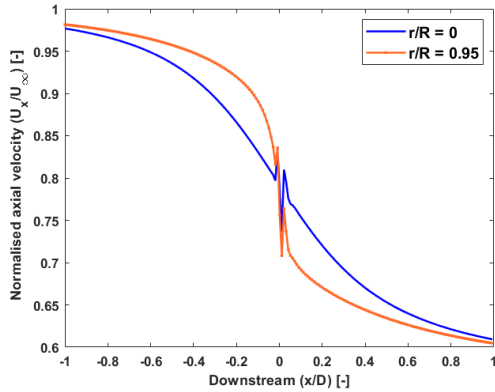


**Figure 3.3:** Axial Velocity downstream of the upstream rotor for coarse mesh

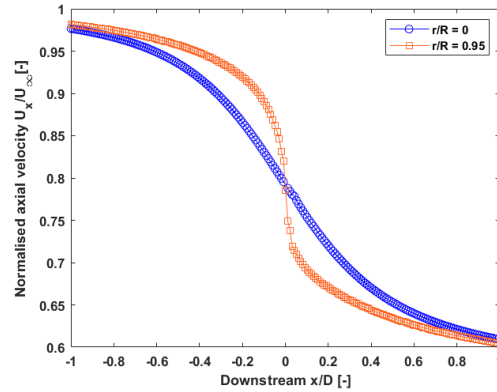


**Figure 3.4:** Smoothed Axial Velocity downstream of the upstream rotor for coarse mesh

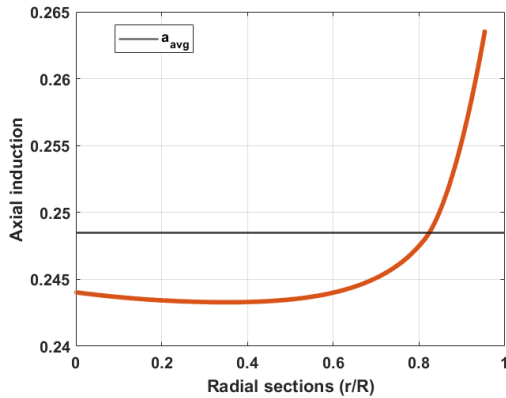


**Figure 3.5:** Radial variation of axial induction downstream of the upstream rotor for coarse mesh

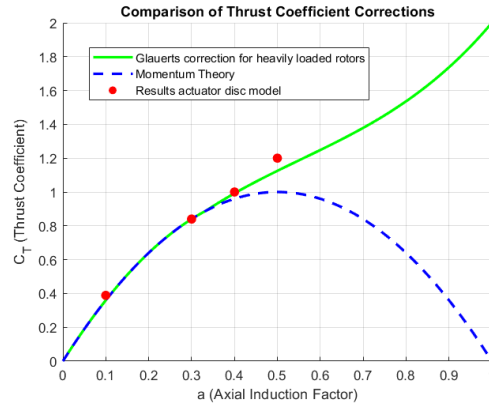


**Figure 3.6:** Comparing ADM results with theory

### 3.3 Summary

This section deals with the dual-rotor and single-rotor configurations. As a first step, the performance of the single-rotor configuration is validated. For the dual-rotor configuration the downstream velocity deficits for a number of different cases (no wake rotation, co-rotating, and counter-rotating) was calculated. With the conditions established by these calculations, the performance of the downwind rotor was computed, to assess how well it works in the dual configuration as compared to the single rotor, which served as the baseline. A summary of the analytical methods—along with a convenient list of assumptions and limitations—is given in Table 3.5.

To obtain detailed information about the interactions of wakes, simulations were performed using computational fluid dynamics along with the actuator disc method (ADM). This allowed us to carry out a 3D analysis of the changes in velocity and the effects of the wake. A mesh independence study was conducted to determine how fine mesh must be, to minimize numerical errors. For the simulations, a mesh that was sufficiently refined and appropriately sized domain

---

was implemented, henceforth level of accuracy was optimized. For the turbulence model, k-omega SST model was selected which is well-known for capturing the near-wake effects at an accurate level. This setup agreed very well with theoretical predictions, and therefore it was set up for our detailed ADM simulations.

**Table 3.5:** Summary approach, assumptions, limitations, and comparison

| Aspect                            | Wilson's Velocity Equation   | O.Gur's Relation   | ADM Simulations (OpenFOAM)  |
|-----------------------------------|--|--|---|
| <b>Assumptions</b>                | <ul style="list-style-type: none"> <li>- Wake rotation is not taken into account.</li> <li>- The centerline linear axial velocity variation downstream.</li> <li>- Thrust coefficient-based induction calculations made straightforward.</li> </ul>    | <ul style="list-style-type: none"> <li>- The wake rotation was incorporated as a linearly varying component within the near field.</li> <li>- Tangential velocity varies linearly in the wake.</li> <li>- Takes for granted that flow is steady and has reached a stable condition.</li> </ul>   | <ul style="list-style-type: none"> <li>- Takes into account the three-dimensional interactions of wakes, turbulence, and the spatial diversity of flow.</li> <li>- Models conditions of uniform aerodynamic loading.</li> <li>- Employs a computational grid of fine mesh and models turbulent flows with state-of-the-art accuracy.</li> </ul> |
| <b>Limitations</b>                | <ul style="list-style-type: none"> <li>-Wake rotation and tangential velocity components are ignored.</li> <li>- Only valid for axial velocity variation along the centerline.</li> <li>- Make flow dynamics simpler, hence less realistic.</li> </ul> | <ul style="list-style-type: none"> <li>- Restricted to wake interactions occurring in close proximity to the rotor.</li> <li>- Presumes the changes in velocity are linear in both the tangential and axial directions.</li> <li>- Inapplicable for predictions of rotor performance at distances comparable to the rotor radius.</li> </ul> | <ul style="list-style-type: none"> <li>- Requires a lot of computational resources.</li> <li>- Demands meticulous mesh refinement and sensitivity investigations.</li> <li>- Delivers results contingent on the turbulence model's precision.</li> </ul>  |
| <b>Results</b>                    | <ul style="list-style-type: none"> <li>- Gives a theoretical baseline for understanding the trends in axial velocity.</li> <li>- Makes predictions about how much the axial flow affects the induction factor and deficit velocity.</li> </ul>         | <ul style="list-style-type: none"> <li>- Considers the effects of tangential velocity and how it interacts with what's going on axially.</li> <li>- Emphasizes how wake rotation influences near-field velocity deficits.</li> </ul>   | <ul style="list-style-type: none"> <li>- Delivers 3D understanding of wake behavior, how fast the velocity recovers, and the nature of the turbulence.</li> <li>- Quantifies wake interactions and induction you get in a truly scaled wind turbine arrangement.</li> </ul>   |
| <b>Comparability and Insights</b> | <ul style="list-style-type: none"> <li>- Appropriate for setting up baseline trends in axial velocity and induction.</li> <li>- Outcomes partially coincide with O. Gur's technique for near-wake axial velocity.</li> </ul>                           | <ul style="list-style-type: none"> <li>- Extends Wilson's findings by including wake rotation effects.</li> <li>- Comparable to ADM results for near-field wake dynamics.</li> <li>- Provides insights into the velocity that is tangential.</li> </ul>  | <ul style="list-style-type: none"> <li>- Confirms analytical results using realistic flow conditions.</li> <li>- Offers an all-encompassing understanding of the impacts of turbulence and spatial factors.</li> <li>- Complements Ogur's technique for comprehensive wake interaction analysis.</li> </ul>                                     |

# CHAPTER 4

## Single Rotor Performance and Validation

### 4.1 Introduction

In this section, we compute the reference model's performance using BEM, validating the results against the turbine report [34]. Additionally, CFD simulations are conducted using the actuator disc method, and these CFD results are compared with the reported results.

### 4.2 BEM Results

The BEM method is employed to evaluate the performance of the reference turbine for a range of tip speed ratios, inflow velocity, and pitch. Firstly, the optimal operational parameters corresponding to the maximum power output are calculated. The performance is then calculated for cut-in and cut-out wind speeds.

#### 4.2.1 Determining Optimal Operating Conditions

The reference model's performance is computed for the range of TSR from 5 to 14 and pitch angles from  $-2^\circ$  to  $5^\circ$ . The TSR and blade pitch must be adjusted in response to changing wind conditions to maximize the power extracted from the wind. When the free-stream velocity results in a tip speed ratio below the optimal value ( $\lambda < \lambda_{opt}$ ), the rotor generates less power. On the other hand, if the rotor spins faster than the optimal speed relative to the wind, the blades create a barrier effect, inducing high turbulence that diminishes power output. Consequently, the power coefficient and turbine efficiency depend on the tip speed ratio. Figure 4.1 and Figure 4.2 show the variation of coefficient of power over the range of tip speed ratio and pitch angles. The optimum values of pitch  $\approx 0^\circ$  and corresponding  $\lambda_{opt} = 8$  for  $C_{Pmax} = 0.4662$ .

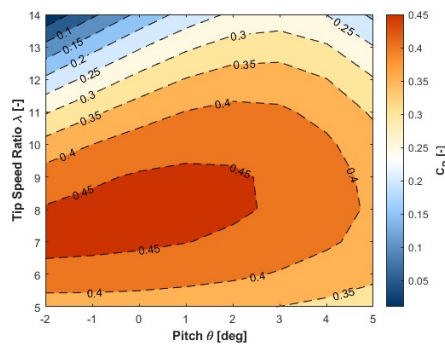


**Figure 4.1:** Variation of  $C_p$  for different  $\lambda$  and  $\theta$  (contour)

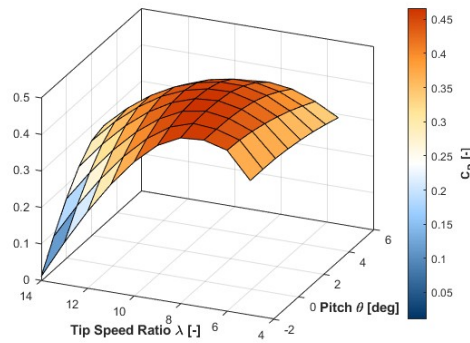


**Figure 4.2:** Variation of  $C_P$  for different  $\lambda$  and  $\theta$  (surface)

Figure 4.3 and Figure 4.4 show the contour and surface plot, it can be observed that the maximum  $C_T$  is 1.1359, which corresponds to optimal values of  $\theta_{opt} = -2^\circ$  and  $\lambda_{opt} = 10$ . The thrust coefficient decreases as the pitch angle increases. This occurs because a higher pitch angle reduces the blade's frontal area, thereby lowering the drag experienced by the blade.

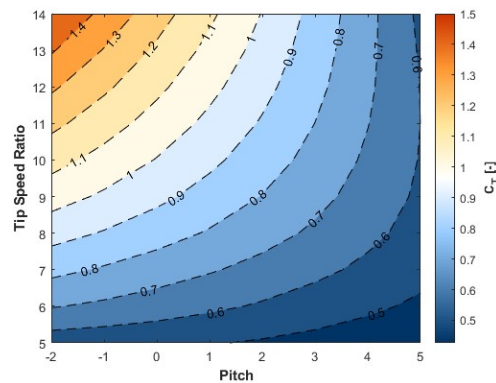


**Figure 4.3:** Variation of  $C_T$  for different  $\lambda$  and  $\theta$  (contour)

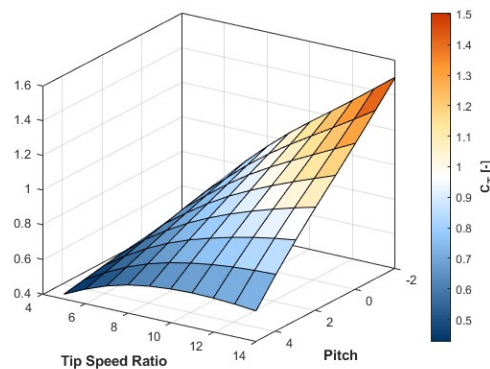


**Figure 4.4:** Variation of  $C_T$  for different  $\lambda$  and  $\theta$  (surface)

The rated velocity of the reference wind turbine, at which it achieves its maximum rated

power output of 10.64 MW, is found to be 11.44 m/s. For a tip speed of 90 m/s, the optimal power coefficient  $C_{p_{\max}}$  is 0.4662, and the maximum angular velocity  $\omega_{\max}$  is 1.01 rad/s. At the rated wind speed of 11.44 m/s, the turbine reaches a rotational speed of approximately 9.79 rpm. Beyond this velocity, the power output must be regulated by adjusting the blade pitch to prevent overloading the generator, as power output increases with the cube of the wind speed. This regulation is achieved by pitching the blades at sub-optimal angles, which reduces aerodynamic efficiency as needed.

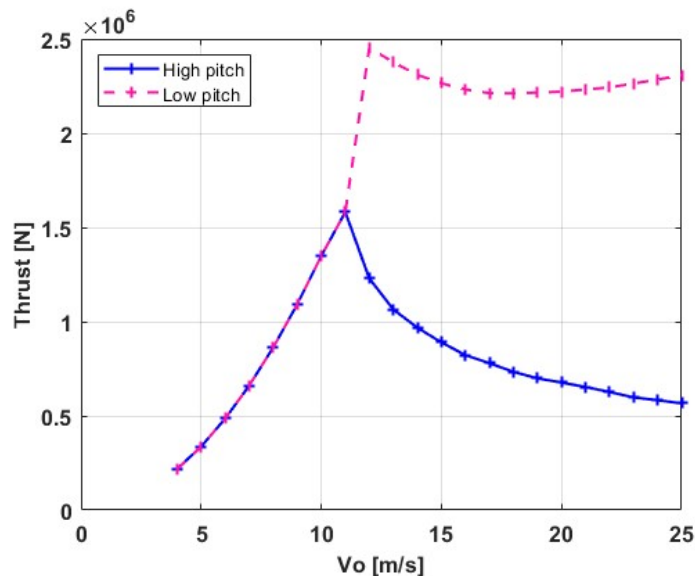


**Figure 4.5:** Thrust for high pitch and low pitch

To control the power output of a wind turbine at high wind speeds, the pitch angle of the blades is adjusted either by feathering, which reduces the angle of attack or by stalling, which increases it. Figure 4.5 shows how pitch angle varies with free-stream velocity, where at rated speed, the blades adjust up or down. At higher angles of attack, the pitch increases with wind speed, while at lower angles, it stabilizes around  $-12^\circ$  beyond 14 m/s. These methods affect the thrust force on the blades, as shown in Figure 4.6. Increasing the pitch reduces both power and thrust by decreasing the angle of attack ( $\alpha = \phi - [\beta + \theta_p]$ ) [32]. Conversely, decreasing the pitch reduces power but significantly increases thrust, which can strain the blades. Therefore, feathering is typically used to stop the turbine when needed safely.

Adjusting the pitch of a wind turbine's blades can significantly impact the wake formed behind the turbine. It also determines how fast or slow the wind will recover depending on the pitch angle of the blades. A higher pitch angle corresponds to the blades being more parallel to the direction of the wind. The turbine is in a low-loading condition, allowing the wind to recover more quickly in the wake behind the turbine. Conversely, a lower pitch angle, which corresponds to the blades being less parallel to the direction the wind is coming from, puts the turbine in a higher-loading condition, which means it is extracting more power and making the wind recover more slowly in the wake itself. Choosing the right pitch angle is essential for wind turbine optimization, particularly in multi-rotor and wind farm configurations.

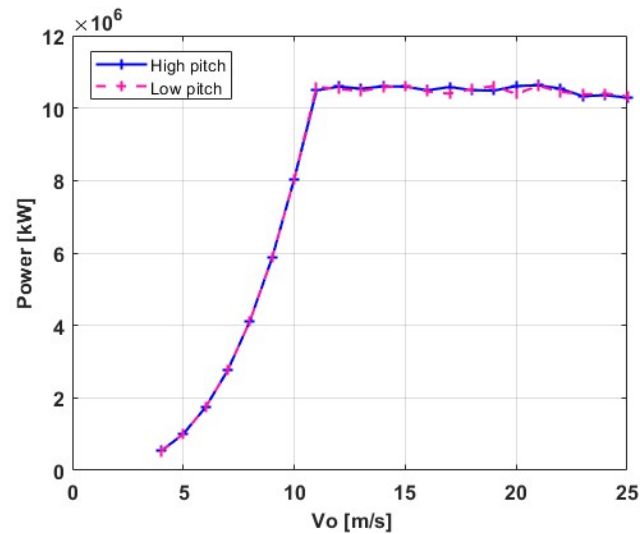


**Figure 4.6:** Power for high pitch and low pitch

## 4.2.2 Validation

BEM results are compared with the values reported in the DTU 10MW report [34], where the data are calculated from HAWT-OPT and HAWCStab2 simulations. Figures 4.7 and 4.8 compare the power coefficient and power output with the DTU report values. Similarly, Figures 4.9 and 4.10 illustrate the comparison of thrust coefficient and thrust. BEM results align well with the DTU 10 MW report values, validating the BEM code used in this study.

The maximum power coefficient  $C_{P_{\max}}$  obtained in this study is slightly underestimated when compared to results from CFD and HAWCStab2 simulations, where  $C_{P_{\max}}$  values of 0.496 and 0.476 were reported at a wind speed of 8 m/s, respectively [34]. The discrepancy can be attributed to several factors, including the simplifying assumptions inherent in the Blade Element Momentum (BEM) method. These assumptions exclude gravitational forces, pylon-shading effects, three-dimensional flow phenomena, and aeroelastic effects, all of which are taken into account in HAWC and Computational Fluid Dynamics (CFD) simulations. Despite these simplifications, the error margins of 2% relative to HAWC and 6% relative to CFD indicate that the basic BEM simulation yields reasonably accurate results.

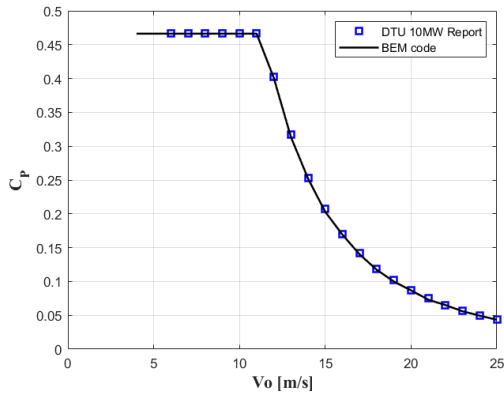


**Figure 4.7:** Comparison of reference model coefficient of power across velocities with BEM results

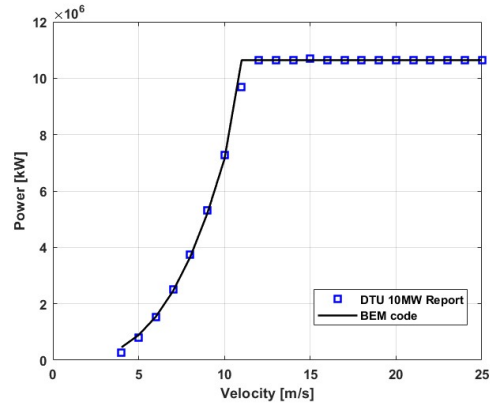


**Figure 4.9:** Comparison of reference model power across velocities with BEM Results

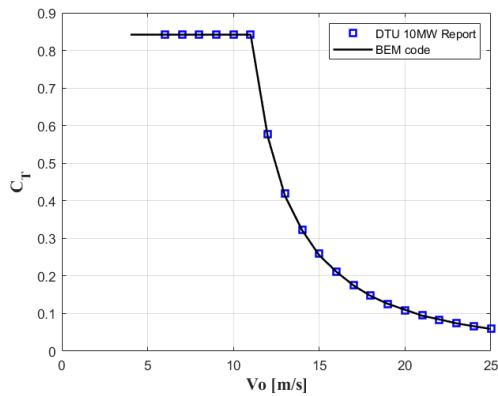


**Figure 4.8:** Comparison of reference model coefficient of thrust across velocities with BEM Results

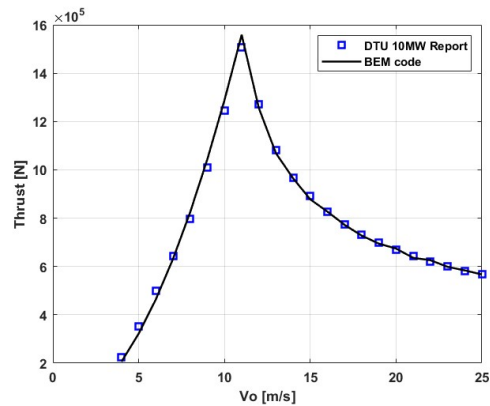


**Figure 4.10:** Comparison of reference model thrust across velocities with BEM Results

After validating the BEM results, the normal and tangential force distributions along the blade span were analyzed across various wind speeds. The forces were observed to be higher towards the blade tip than near the hub due to the greater induced velocities at the tip. As wind speed increased, both the magnitude and distribution of these forces also increased, as shown in Figure 4.11 for the normal force distribution and Figure 4.12 for the tangential force distribution.

The performance of the turbine at different tip speed ratios is analyzed. Figure 4.13 and Figure 4.14 illustrate the power and thrust coefficients, respectively, while Figure 4.15 and Figure 4.16 show the corresponding power output and thrust forces. It is observed that for higher tip speed ratios, the magnitude of the forces increases as expected. However, beyond the rated wind speed, the control mechanisms reduce  $C_P$ ,  $C_T$ , power output, and thrust force to protect the turbine while ensuring it maintains the rated power output.

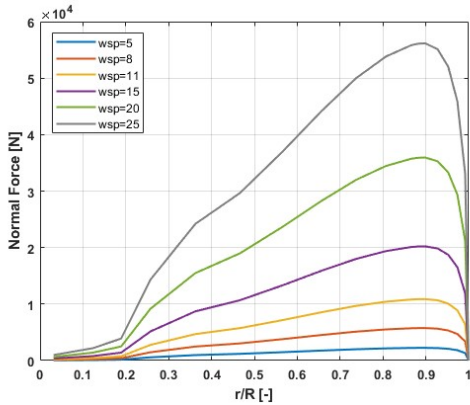


**Figure 4.11:** Normal force distribution over blade span for different wind speeds

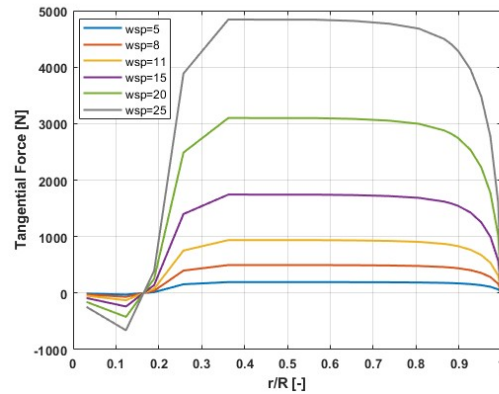


**Figure 4.12:** Tangential force distribution over blade span for different wind speeds

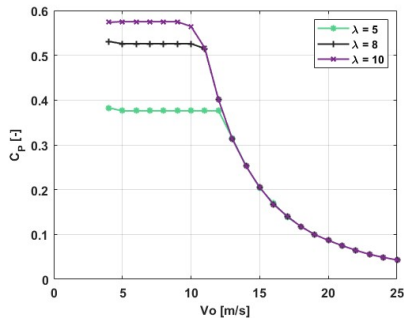


**Figure 4.13:** Power coefficient variation across wind speeds for different TSR

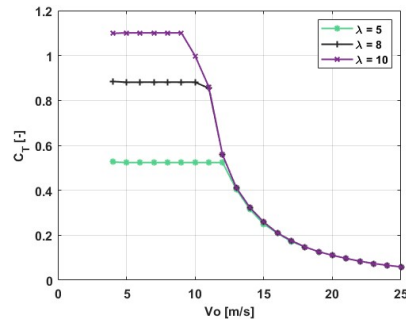


**Figure 4.14:** Thrust coefficient variation across wind speeds for different TSR

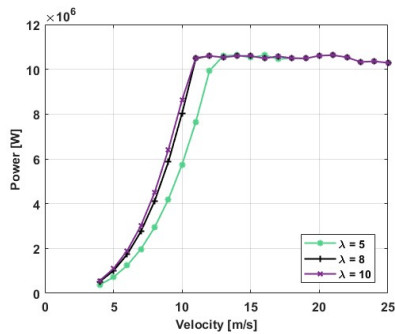


**Figure 4.15:** Power variation across wind speeds for different TSR

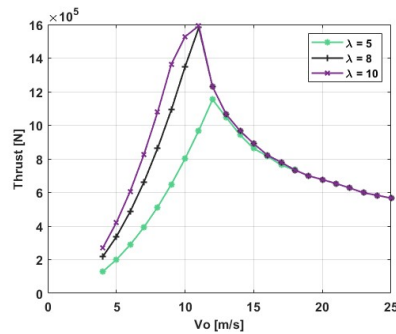


**Figure 4.16:** Thrust variation across wind speeds for different TSR

Figure 4.17 and Figure 4.18 illustrate the distribution of the axial and tangential induction factors along the blade span. The axial induction factor is higher at the blade tip than at the root, increasing with the tip speed ratio. In contrast, the tangential induction factor peaks just beyond the cylindrical portion of the blade. Additionally, the tangential induction factor remains smaller than the axial induction factor.

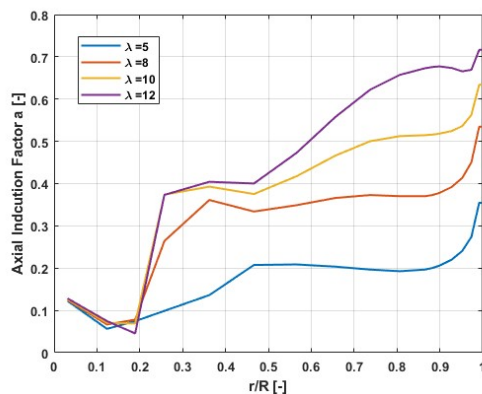


**Figure 4.17:** Axial induction factor distribution over bladespan

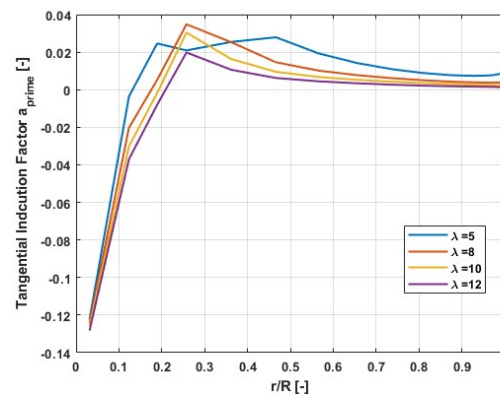


**Figure 4.18:** Tangential induction factor distribution over bladespan

### 4.2.3 Annual Energy Production

AEP is calculated for wind speeds between the cut-in velocity  $V_{\text{cut-in}} = 4$  m/s and the cut-out velocity  $V_{\text{cut-out}} = 25$  m/s, the total number of operational hours can be calculated using Equation 2.66. Specifically, within the range  $4 < V_o < 25$ , the annual operational hours amount to approximately 7062 hours, resulting in an annual energy output of 38.34 GWh. For turbulent wind speed data, calculated using HAWC2S, the total output is 33.80 GWh [36].

Using these results, the capacity factor for the 10.64 MW wind turbine can be determined by dividing the annual energy output by the theoretical maximum annual energy output, which assumes continuous operation at the rated power  $P_{\text{rated}}$ . This calculation yields capacity factors of 41.14% and 36% for 38.34 GWh and 33.80 GWh, respectively, which aligns well with statistics for offshore wind turbines in Denmark, where capacity factors typically range between 40% and 50% [37].

## 4.3 Actuator Disc Simulations Results

From the actuator disc simulations, the axial induction factor is calculated by taking a weighted average of the axial induction along the blade radius. This flow axial induction is then used to compute the power output. Single rotor simulations are conducted over the specified velocity range, and the resulting power values are compared with those from the BEM method and the DTU 10 MW report, showing good agreement as shown in Figure 4.19.

Figure 4.20 presents the normalized axial velocity for different cases. Based on the power and thrust curves, ADM simulations are run for various velocities and corresponding  $C_T$  values. In the higher velocity range, where  $C_T$  values are lower, there is still more energy left in the flow and the wake is weak hence the wake recovers more quickly. Conversely, in the lower velocity range, the  $C_T$  values are higher, resulting in a significant velocity deficit in the wake. This indicates that as the aerodynamic loading decreases, the wake recovery accelerates, as there is still considerable energy left in the flow. Furthermore, when the rotor is subjected to low loading the wake recovers fast and there is more available energy which can be captured by placing another rotor in the downstream.

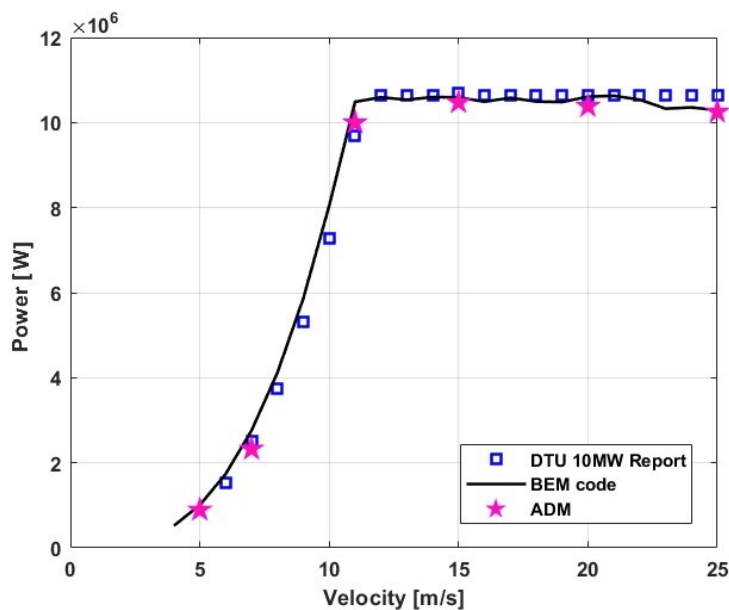


**Figure 4.19:** Validating the ADM power values with BEM and DTU 10MW results

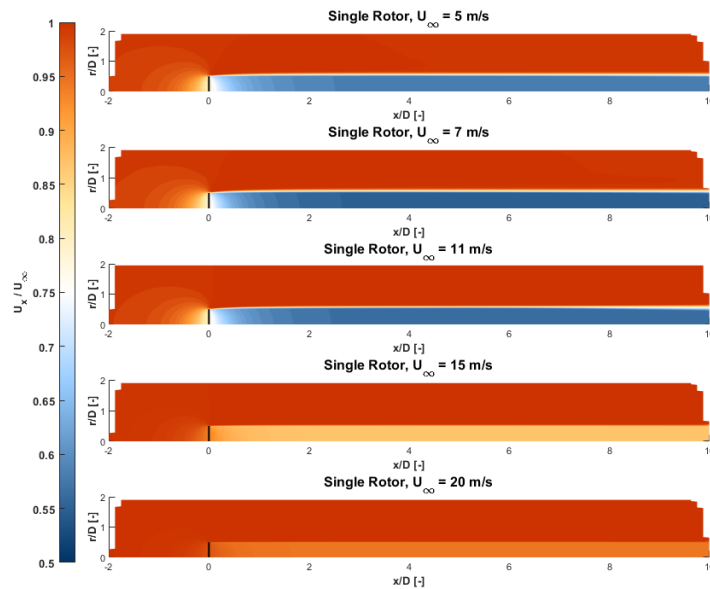


**Figure 4.20:** Normalised velocity variation in the downstream for variable  $C_T$

## 4.4 Summary

This chapter comprehensively evaluates the reference wind turbine's performance using the Blade Element Momentum method. The evaluation is validated against data from the 10 MW report produced by the Danish Technical University. The report authoring team included several renowned wind turbine aerodynamicists. The report is widely considered a benchmark for wind turbine performance assessment. Results from BEM calculations are in strong agreement with results from advanced simulation tools, including HAWT-OPT and HAWCStab2. The strong agreement suggests that BEM method is a robust assessment tool, rendering insights into the kinds of operating conditions one should expect from a wind turbine performing near its design limits.

The chapter investigated the influence of governing variables on the performance of an offshore wind turbine, focusing primarily on blade pitch. Power regulation is critical for safe turbine operation, and our primary research question was this: how does wind turbine governing power regulation work, particularly at varying wind speeds? An examination of the physical principles involved was conducted, working from a basic model to our final enhanced model. The basic model revealed the challenges inherent in ensuring safe operation during surges of power demand while attempting to also maintain adequate power supply during variable wind conditions. The working surfaces of the basic physical model were plotted and the results are used to derive expressions that formed the basis of the enhanced model. The validated BEM model and the derived optimal values will serve as a foundation for evaluating the performance of dual rotor configurations in subsequent studies. The ADM simulations are computed for the velocity range similar to BEM and the results are compared with the BEM and DTU 10 MW reports.

# CHAPTER 5

## Dual Rotor Performance - No rotation

---

### 5.1 Introduction

In this chapter, BEM is initially used to calculate the influence of the upwind rotor axial induction on the performance of the downwind rotor. Additionally, the effect of varying TSR and the pitch angle of the upwind rotor on the downwind rotor is analysed. Furthermore, the CFD simulations used are discussed. These simulations compute the near-wake and the influence of upwind and downwind rotors on each other.

### 5.2 BEM Results

In this section, as outlined in chapter 3, the approach begins by calculating the velocity deficit in the downstream wake, followed by an evaluation of the performance of the downwind rotor. A key assumption in this analysis is that wake rotation is not considered when calculating the power of the downwind rotor. Instead, only the effect of the upwind rotor's axial induction on the downwind rotor is considered, without any blockage effects affecting the interaction between the downwind and upwind rotors.

The velocity deficit is analyzed at various tip speed ratios and pitch angles. The upwind rotor is evaluated under optimal conditions, while the performance of the dual rotor system is assessed. Subsequently, an optimization analysis is conducted to determine the best positioning and operating conditions to maximize the total power output of the dual rotor configuration. This study involves varying the tip speed ratios and pitch angles of the upwind rotor.

#### 5.2.1 Velocity in the wake

The Equation 2.46 is used to calculate the axial induction factor in the flow behind the upwind rotor, and with Wilson's Equation 2.27, the velocity deficit along the rotor disc centerline is determined for a 1D downstream distance. The wake velocity profile for the upwind rotor operating under optimal conditions is shown in Figure 5.1. The rotor has a tip speed ratio of  $\lambda = 8$  and a thrust coefficient of  $C_T = 0.84$ . The values presented correspond to the maximum power coefficient of the upwind rotor at various downstream distances. The dashed lines illustrate the velocities in the near-wake and far-wake regions. As observed, the velocity deficit has not yet reached the far-wake velocity, indicating that it remains within the near-wake region. There is a steep decline in velocity up to approximately  $0.4D$ , after which it decreases more gradually. Positioning the downwind rotor within the near-wake could provide an advantage, as the velocity deficit remains low in this area.

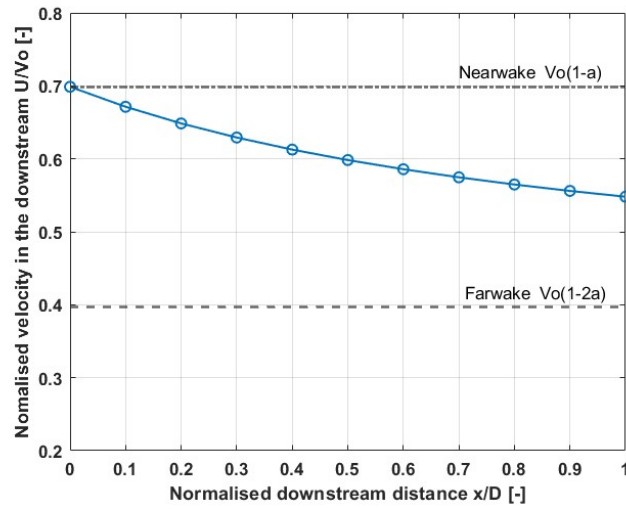


**Figure 5.1:** Normalised velocity in the wake of upwind rotor ( $\lambda = 8$ )

## 5.2.2 Varying downstream distance

The downwind rotor is placed at three different locations i.e. 10%D, 20%D, 40%D. based on the location, the inflow velocity from the wake profile is calculated, and then, using BEM, the performance is calculated for the downwind rotor. The performance of the dual-rotor configuration is compared with the performance of a single rotor. Figure 5.2 shows the sketch of the placement of the rotor on either side of the hub for a rotor spacing of 10%D, 20%D, and 40%D, where  $D$  is the diameter. The performance of the downwind rotor is computed when the upwind rotor is operating at optimal conditions, i.e.,  $\lambda_{opt} = 8$  and  $\theta = 0^\circ$ . The downwind rotor operates for a range of TSR varying from 5 to 14.

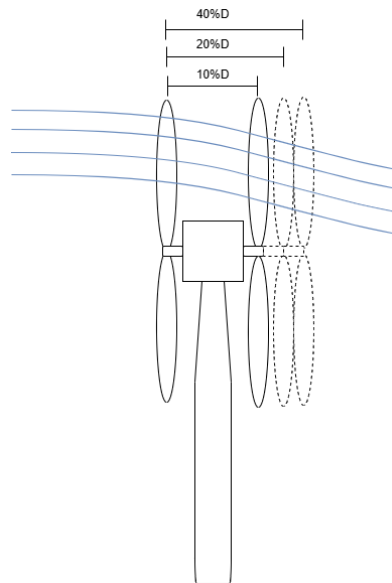


**Figure 5.2:** Sketch illustrating dual rotor for different downstream distances (not to the scale)

In this case, the upwind rotor operates at  $\lambda_{\text{opt}} = 8$ ,  $V = 11$  m/s, and  $\theta = 0^\circ$ , while the performance of the downwind rotor is analyzed for varying TSRs. Figure 5.3 shows the power of the downwind rotor with the single rotor. The upwind rotor, when operating under optimal conditions, captures the maximum amount of power. However, the downwind rotor at lower TSRs shows low performance. It has been observed that at TSRs around 7 to 8, the downwind rotor is able to achieve higher power extraction. Beyond this optimal TSR range, the performance begins to decline, similar to that of a single rotor. This decline occurs because the rotor blades operate at suboptimal lift-to-drag ratios at higher TSRs.

As the spacing between the rotors increases, the performance of the downstream rotor declines. This reduction is attributed to the axial induction effects present in the wake. From the analysis of Figure 5.1, it is clear that the velocity deficit remains significant up to approximately  $40\%D$ . At a spacing of  $10\%D$ , the velocity deficit is lower, leading to a smaller decrease in the new inflow velocity and, consequently, higher performance compared to rotors positioned at  $20\%$  and  $40\%D$ . It is important to note that the Wilson model calculates performance solely based on the axial induction factor. This model does not take into account the effects of wake rotation. As a result, while a reduction in magnitude is observed, the trend remains consistent for downwind rotors when compared to single rotors.

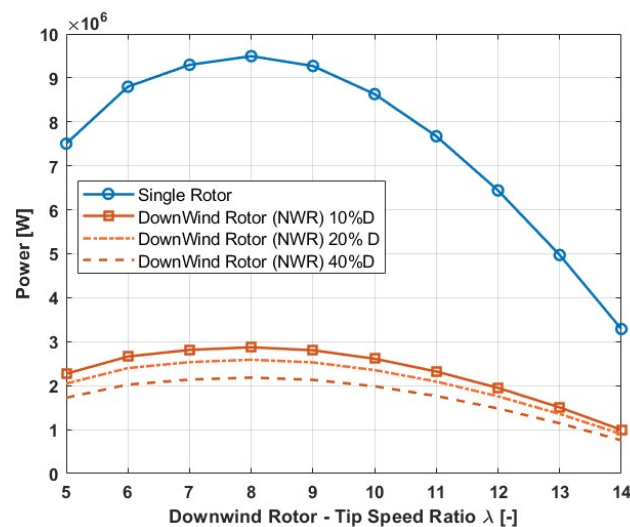


**Figure 5.3:** Comparing the Power for single rotor and downwind rotor placed at different downstream distances

Similar to power, the thrust of the downwind rotor decreases with increasing rotor spacing, as shown in Figure 5.4.

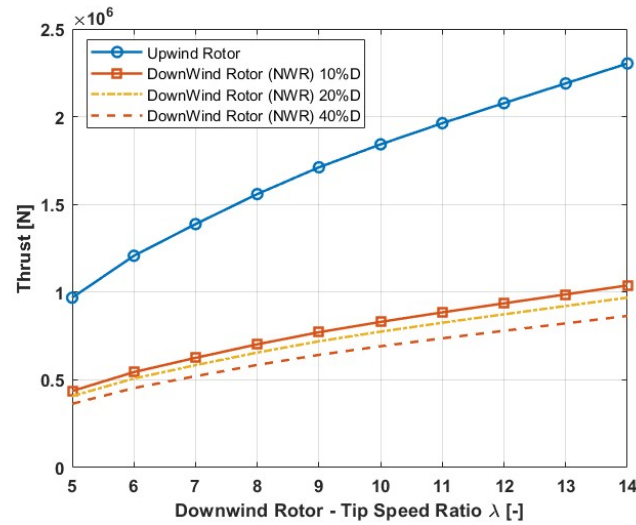


**Figure 5.4:** Comparing the Thrust for single rotor and downwind rotor placed at different downstream distances

Figure 5.5 illustrates the comparison of power curves between a single rotor and a dual rotor system. It is evident that the dual rotor generates more power across various tip-speed ratios. This performance improvement occurs because the upwind rotor operates under optimal conditions, effectively capturing maximum energy, while the downstream rotor compensates for energy losses in the wake created by the upwind rotor. As a result, the dual rotor configuration is less sensitive to variations in TSR due to the compensation provided by the downstream rotor. Similarly, Figure 5.6 shows the thrust curve. It is observed that the thrust for a single rotor increases linearly with the thrust-to-speed ratio, while the dual-rotor system consistently achieves higher total thrust due to the contributions from both rotors. As the distance between the rotors increases downstream, the thrust magnitude decreases. Based on the power and thrust curves, positioning the second rotor at a downstream distance of 10%D of the rotor diameter significantly improves the efficiency of the dual-rotor system.

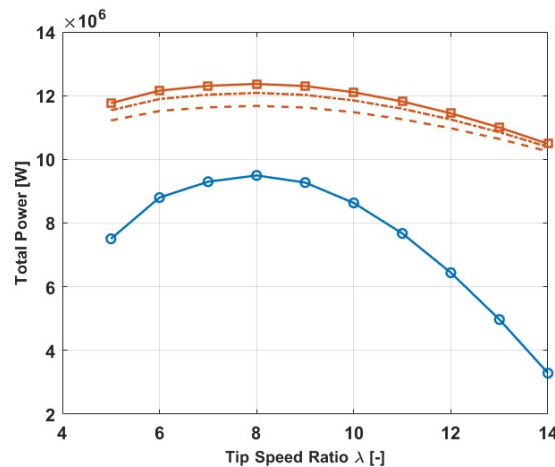


**Figure 5.5:** Comparing the single rotor Power[W] to the dual-rotor

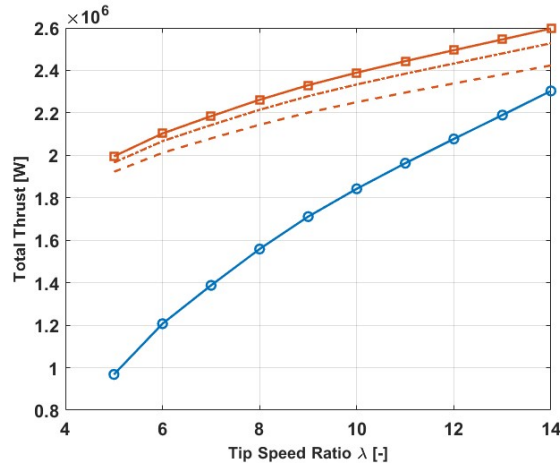


**Figure 5.6:** Comparing the single rotor Thrust[N] to the dual-rotor

As shown in Figure Figure 5.7, the total power is normalized based on the performance of a single rotor. The figure illustrates that the downwind rotor captures a greater amount of power. However, as the distance between the rotors increases, the power extracted by the downwind rotor decreases. The upwind rotor captures 46% of the available power at a specific freestream velocity. When the second rotor is positioned 10%D downstream, the total power captured by the dual-rotor system increases to 61%, with the downstream rotor contributing an additional 30% of the available energy. At a downstream distance of 20%D, the dual-rotor configuration captures 58% of the available power, and at 40%D of the rotor diameter, the total power capture decreases slightly to 57%.

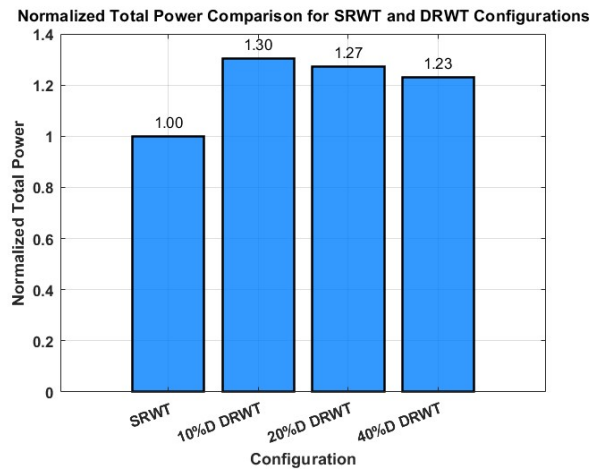


**Figure 5.7:** Comparing Power single-rotor to dual-rotor varying with the distance between the rotors

The comparison of thrust between single-rotor and dual-rotor configurations reveals the significant effect of downstream rotor placement on overall system performance. Dual-rotor configurations consistently produce greater total thrust than single-rotor configurations, with normalized thrust peaking at a downstream distance of 10% D, achieving 1.45 times the thrust of the single rotor. As the downstream distance increases to 20% D and 40% D, the total thrust diminishes to 1.42 and 1.38 times, respectively. This indicates that closer rotor placement improves system efficiency.

The thrust contributions from the downwind rotor indicate that as the separation between the rotors increases, the contribution from the downwind rotor decreases. This leads to a gradual decline in overall performance. It is crucial to optimize the rotor position to achieve the best overall performance. A dual-rotor setup with a rotor spacing of 10% of the rotor diameter (10% D) shows optimal performance.

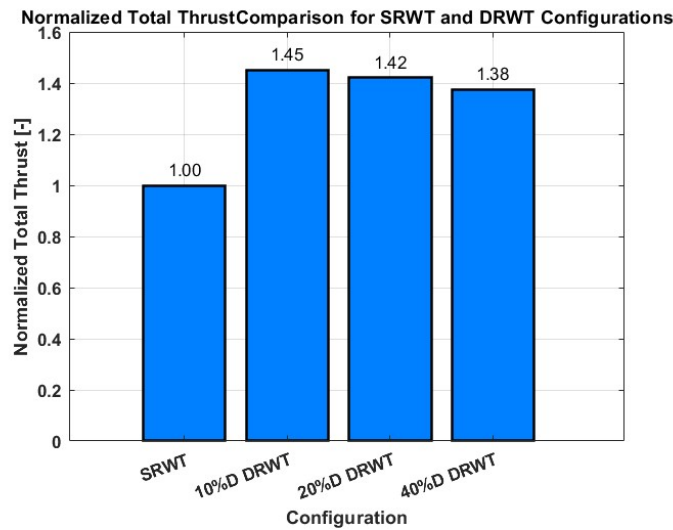


**Figure 5.8:** Comparing Thrust single-rotor to dual-rotor varying with distance between the rotors

### 5.2.3 Effect of variable rotational speed

Literature suggests that the maximum total power is extracted when the upwind rotor does not operate at the optimal TSR [10]. In this section, the different combinations of TSR for upwind and downwind rotors are explored to investigate the optimal combination of TSRs to capture maximum available power. Figure 5.9 shows the velocity in the wake varying as a function of the tip-speed ratio. As the tip-speed ratio increases, the loading on the upwind turbine also increases, leading to a greater velocity deficit. The flow induction is calculated for various load values, followed by the calculation of the velocity deficit downstream of the upwind rotor.

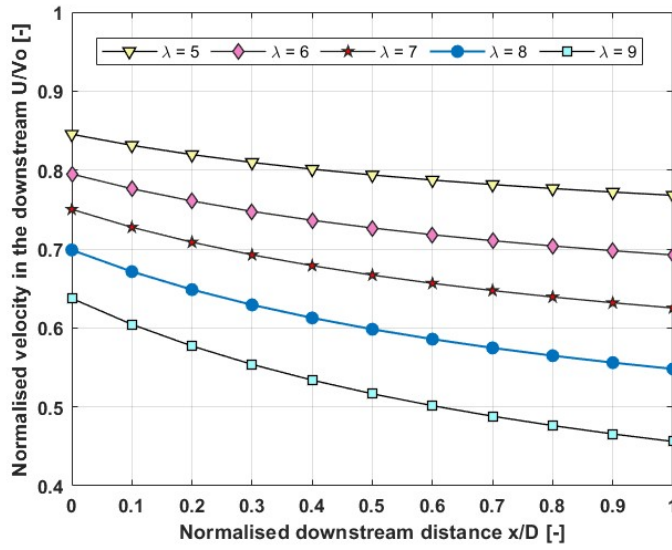


**Figure 5.9:** Normalised velocity in the wake of upwind rotor for varying TSR

Firstly, the performance is computed for the scenario where both the turbines are operating at the same TSR. The Figure 5.10 and Figure 5.11 The text compares the power and thrust of dual rotor systems with single rotor systems, as well as the performance of downwind rotors. As the Tip Speed Ratio (TSR) increases, the power of the dual rotor system also increases, showing a significant increase in magnitude. However, it follows the same trend as the single rotor system. Additionally, as the spacing between the rotors increases, the overall power magnitude decreases due to the increased induction effect, which aligns with the earlier explanation.

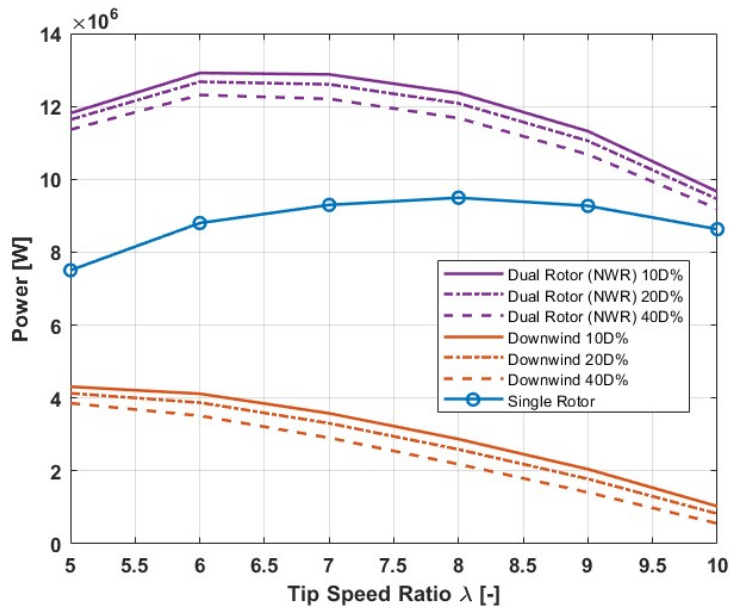


**Figure 5.10:** Comparing the Power[W] for dual rotor, single rotor and downwind rotor contribution for the upwind and downwind rotors operating at same TSR

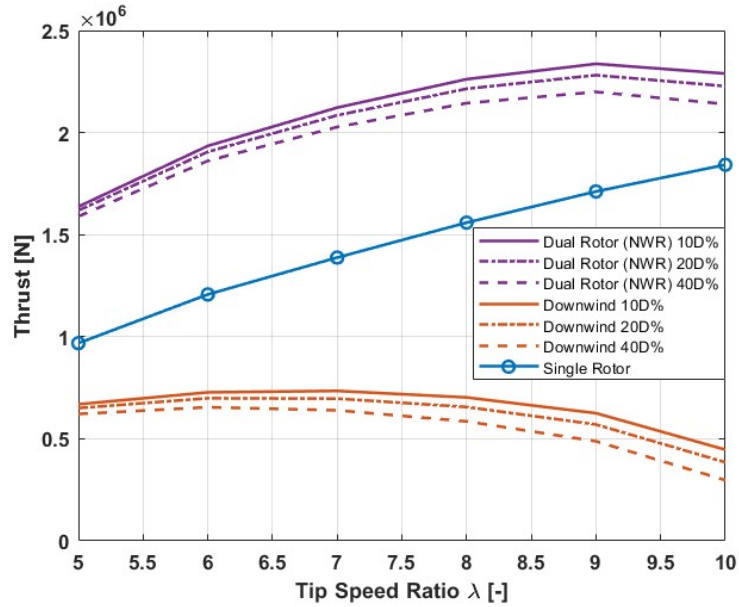


**Figure 5.11:** Comparing the Thrust [N] for dual rotor, single rotor and downwind rotor contribution for the upwind and downwind rotors operating at same TSR

Figure 5.12 shows the variation in total power produced by a dual-rotor wind turbine system as a function of the ratio between the TSR of the downstream and upstream rotors ( $\lambda_{downwind}/\lambda_{upwind}$ ) for various upstream rotor tip-speed ratios ( $\lambda_{upwind}$ ) and downstream distances. The total power shows maximum power at specific values of  $\lambda_{downwind}/\lambda_{upwind}$ , typically between 1.3 and 1.7, depending on the upstream TSR and downstream distance. For upstream TSRs of  $\lambda_{upwind} = 5$  and  $\lambda_{upwind} = 8$ , the highest total power is observed when the downstream rotor is placed at 10%D. As the distance increases to 20%D and 40%D, the total power decreases due to the downstream rotor operating further into the wake, where the velocity deficit reduces the available energy.

Higher upstream TSR values ( $\lambda_{upwind} = 10$ ) result in lower total power due to reduced efficiency in wake energy extraction, and the sensitivity to downstream distance is more pronounced. Conversely, moderate upstream TSRs ( $\lambda_{upwind} = 8$ ) demonstrate a balanced performance across different distances, with the optimal configuration being at 10%D. This plot highlights the importance of optimising the TSR ratio and downstream rotor placement to maximise the total power output of the dual-rotor system.

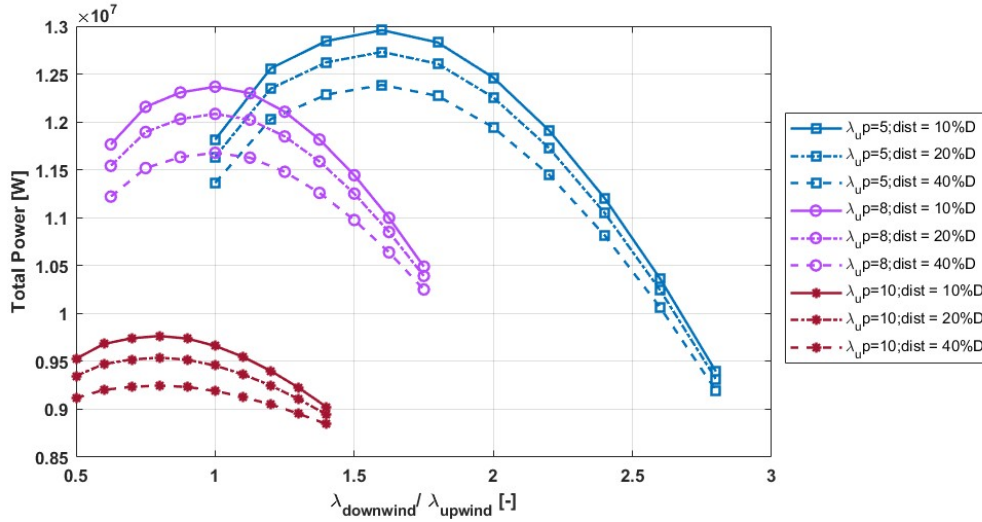


Figure 5.12: Comparing the total power for various TSR combinations

The total thrust generated by a dual-rotor wind turbine system as a function of the TSR ratio between the downstream and upstream rotors ( $\lambda_{downwind}/\lambda_{upwind}$ ) for different upstream TSRs ( $\lambda_{upwind}$ ) and downstream distances is shown in the Figure 5.13. The total thrust increases steadily with  $\lambda_{downwind}/\lambda_{upwind}$  for all configurations. At an upstream TSR of  $\lambda_{upwind} = 8$ , the system produces the highest total thrust, particularly for shorter downstream distances (10%D), as the downstream rotor benefits from higher energy availability in the near-wake region. As the downstream distance increases to 20%D and 40%D, the total thrust decreases due to wake dissipation and a larger velocity deficit in the downstream rotor. Higher upstream TSR values ( $\lambda_{upwind} = 10$ ) result in lower overall thrust due to reduced aerodynamic loading caused by higher wake velocities. Shorter distances (10%D) consistently show better performance in terms of thrust across all configurations, while the impact of distance is less pronounced at lower upstream TSRs ( $\lambda_{upwind} = 5$ ).

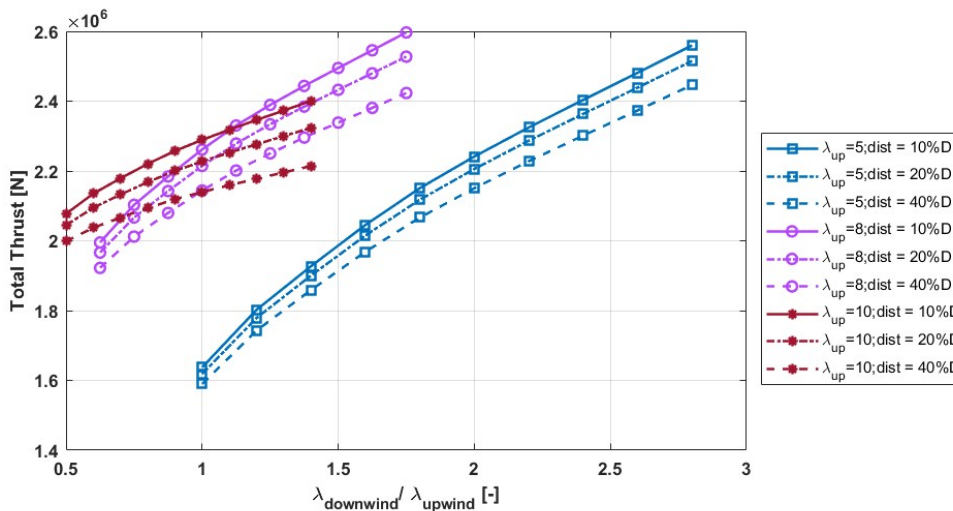


Figure 5.13: Comparing the total thrust for various TSR combinations

To achieve an optimal dual-rotor design, it is essential to consider the variations in both power and thrust together. It has been observed that maximum power is attained when the thrust-to-speed ratio (TSR) and rotor distance are carefully balanced. While higher power output is beneficial for energy generation, too much thrust can result in increased structural stress and a shortened lifespan of turbine components. An upstream TSR of  $\lambda_{upwind} = 8$  and a downstream distance of  $10\%D$  of the rotor diameter emerge as the optimal configurations, striking a balance between power and thrust performance. This combined analysis guarantees efficient energy extraction while preserving structural integrity and minimizing wake losses.

### 5.2.4 Effect of variable pitch

Pitching has a significant impact on the loading of a wind turbine. The pitch angle, defined as the angle of the blades relative to the oncoming wind, directly affects the aerodynamic forces acting on the rotor blades, which in turn influences the rotor loading. A smaller (or negative) pitch angle increases the angle of attack, leading to higher lift forces on the blades. This increases the aerodynamic loading ( $C_T$ , the thrust coefficient), which can maximise energy extraction but also subjects the blades and rotor to higher mechanical stresses. Conversely, a larger (or positive) pitch angle decreases the angle of attack, reducing lift and drag forces. This decreases the rotor loading and aerodynamic forces, providing protection for the turbine in high wind conditions.

The pitch angle also affects the axial induction factor, which represents how much the wind slows down as it passes through the rotor. A smaller pitch angle (higher loading) results in a larger induction factor, causing a greater velocity deficit in the wake. In contrast, a larger pitch angle reduces the induction factor, decreasing the velocity deficit and loading as shown in the ?? and Figure 5.14 respectively,

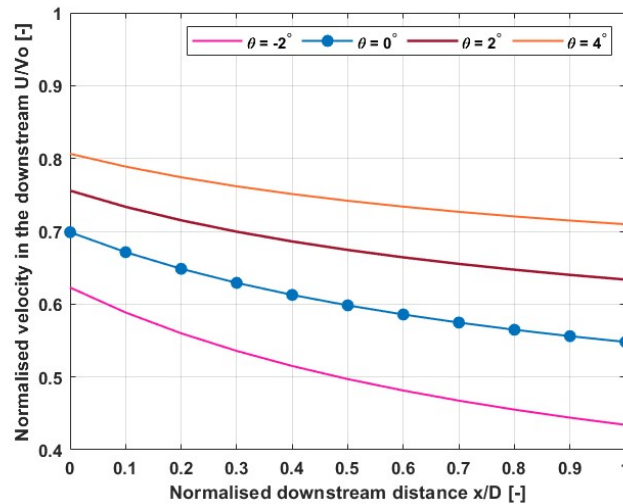


**Figure 5.14:** The velocity deficit for varying pitch at upwind optimal operating conditions

The variation in the power output of a dual-rotor wind turbine with a downstream rotor placed at  $10\%D$  from the upstream rotor is shown in ???. The power output is shown as a function of the pitch difference ( $\theta_{tupwind} - \theta_{downwind}$ ) for different upwind rotor pitch angles ( $\theta_{upwind}$ ). Figure 5.17 shows the power coefficient variance for the  $\theta$  For all upwind

pitch angles, the power output increases as the pitch difference approaches zero, peaks at a small positive pitch difference. Higher pitch angles of the upwind rotor ( $\theta_{upwind} = 4^\circ$ ) consistently yield the highest power, while lower pitch angles ( $\theta_{upwind} = -2^\circ$ ) result in a reduced power output. The figure highlights the sensitivity of power output to pitch difference, particularly at lower upwind rotor pitch angles. Optimal performance is achieved with a small positive pitch difference and higher upwind rotor pitch angles, emphasising the importance of coordinated pitch control to maximise the efficiency of dual-rotor systems.

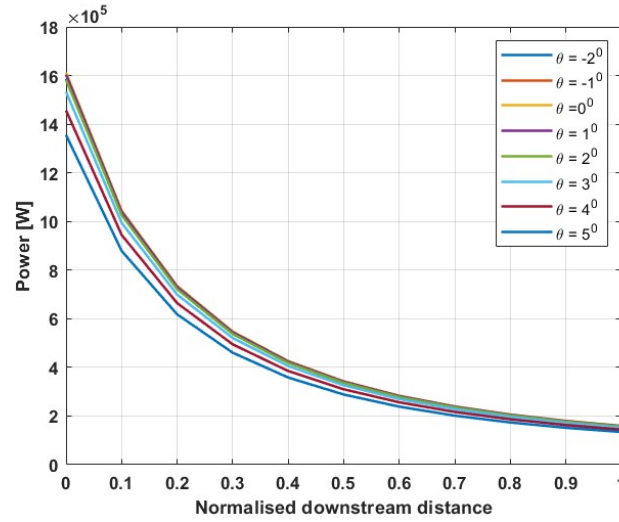


**Figure 5.15:** Power coefficient variation for pitch difference between two rotors as a set of curves for increasing upwind rotor pitch

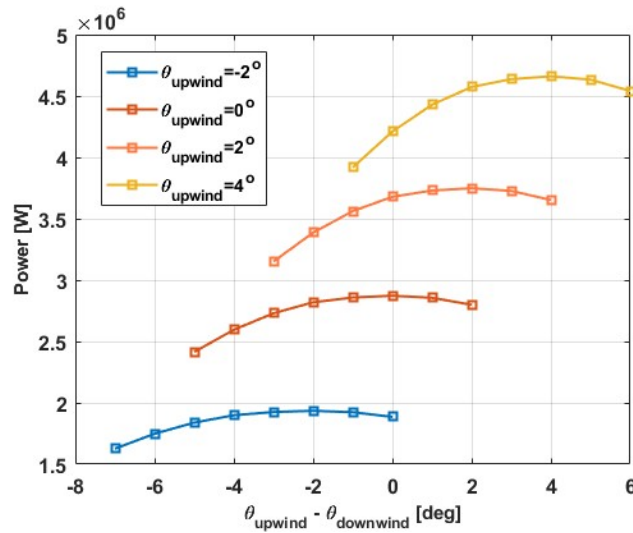


**Figure 5.16:** Power coefficient variation for DRWT 10%D pitch difference between two rotors as a set of curves for increasing upwind rotor pitch

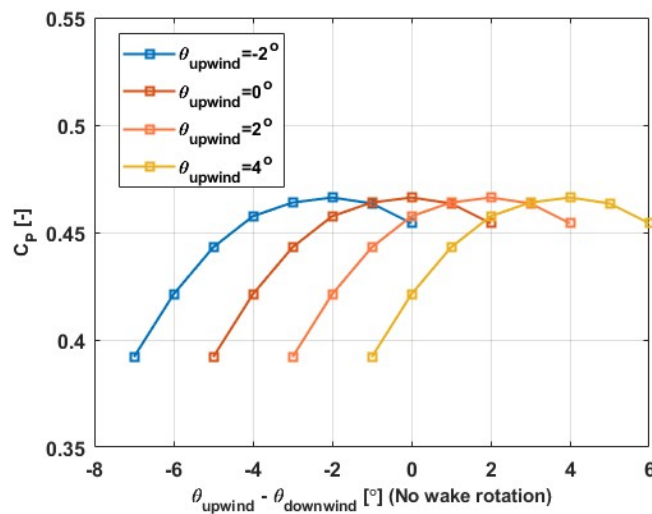


**Figure 5.17:** Power coefficient variation for pitch difference between two rotors as a set of curves for increasing upwind rotor pitch

## 5.3 Actuator Disc Simulation Results

Actuator Disk Model simulations are conducted to investigate the aerodynamic interaction between upwind and downwind rotors. Similar to BEM analysis, two rotors of the same diameter are placed at varying downstream distances. These computations provide a detailed study of wake interactions and their impact on the performance of the downstream rotor. A constant load is applied to both rotors, and the velocity deficit is calculated in the downstream. While the effect of wake rotation is challenging to implement in a simple actuator disc simulation due to the constant load and limitations of the model, the axial induction is modeled. The influence of the force model on the downstream rotor is analysed, and the influence of the downstream rotor on the upstream rotor.

The axial velocity in the wake along the centerline, calculated using Wilson's equation, is compared with the actuator disc simulations. Both data sets exhibit a similar trend, showing a reduction in velocity as the normalised downstream distance increases. However, a noticeable difference in the magnitude of the velocity is observed. This discrepancy can be attributed to the fact that Wilson's equation is based on a 1D momentum theory, while the actuator disc simulations are 3D and account for more complex flow phenomena.

Furthermore, Wilson's model shows a larger velocity deficit compared to the actuator disc simulations, particularly further downstream. This suggests that the 1D assumptions made by Wilson's model may oversimplify the flow dynamics, whereas the actuator disc model, being 3D, captures more detailed flow interactions, leading to a smaller velocity deficit.

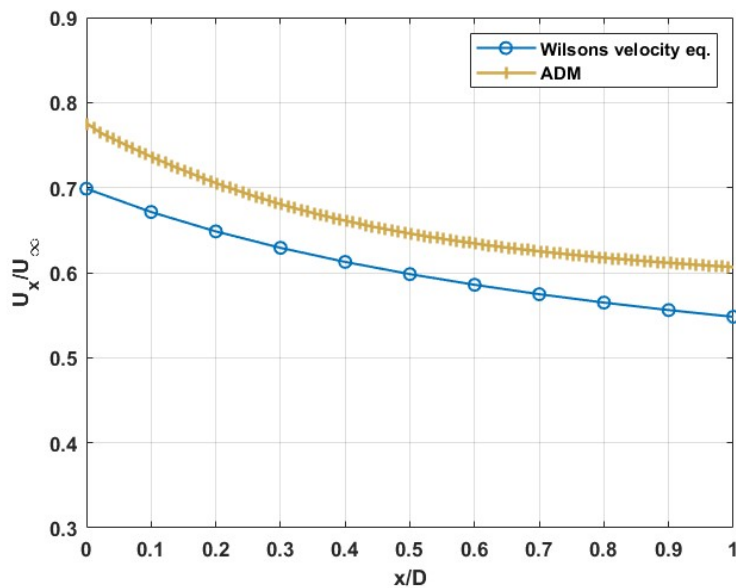


**Figure 5.18:** Axial velocity in the downstream wake of the upstream rotor. The velocity is compared between Wilson’s model, Actuator Disc Model (ADM), and observed far-wake velocity.

As the actuator disc method accounts for 3D wake effects, it enables the computation of wake influence and interaction between two rotors in each other’s presence. To investigate this, the upstream and downstream velocities of a single rotor are compared with those of a dual-rotor configuration at a close spacing of 10% of the rotor diameter ( $0.1D$ ), where the upstream rotor experiences the maximum influence.

Figure 5.19 shows the normalized axial velocity ( $U/U_\infty$ ) along the centerline of the rotor disc for a single-rotor and a dual-rotor at a spacing of 10% of the rotor diameter ( $0.1D$ ). The normalised velocity upstream of the dual rotor is lower compared to the single rotor due to wake interference. Downstream, the dual-rotor configuration results in a larger velocity deficit, as the downwind rotor extracts more energy from the flow. The Figure 5.20 shows a similar comparison but for the normalised velocity near the tip region (i.e.  $r/R = 0.95$ ). The upstream velocity for the dual rotor shows significant deviations closer to the tip, indicating stronger wake interactions. In the downstream, the velocity differs due to the greater energy extraction by the dual-rotor configuration, resulting in increased velocity deficits near the tip compared to the single rotor.

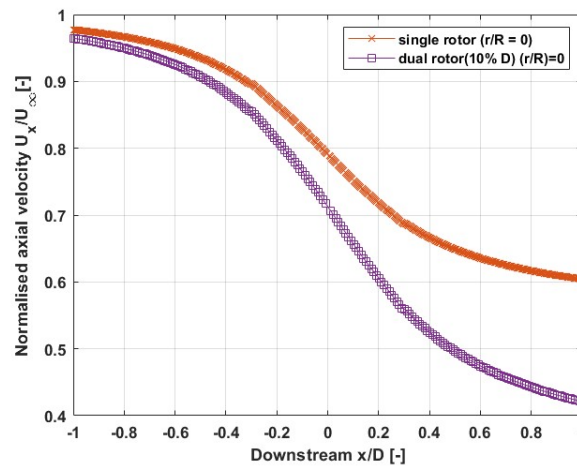


**Figure 5.19:** Comparing normalised velocity in upstream and downstream for single rotor and dual rotor for centerline ( $r/R = 0$ )

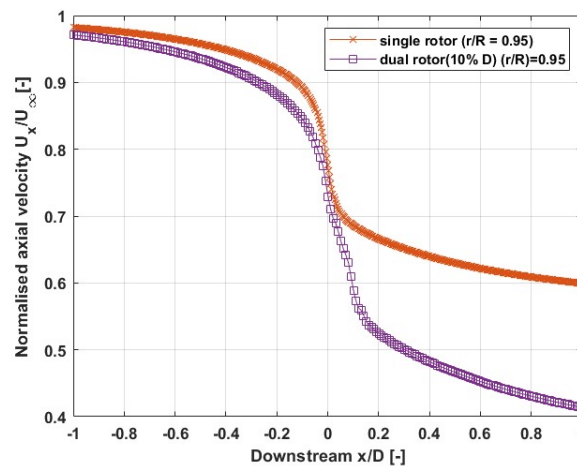


**Figure 5.20:** Comparing normalised velocity in upstream and downstream for SWRT and DWRT for  $r/R = 95$

Figure Figure 5.21 compares the power generated by the dual rotor and the single rotor. It is clear that as the downstream distance increases, the influence of the downwind rotor on the upwind rotor decreases. The table Table 5.1 compares the simulated power outputs of dual-rotor and single-rotor configurations. It is observed that the downstream rotor significantly influences the performance of the upstream rotor in a dual-rotor configuration. Especially for the rotors placed at a close spacing  $10\%D$ . This interaction is primarily influenced by wake effects and mutual interference between the two rotors. The downstream rotor alters the velocity field of the upstream rotor, resulting in a decrease in the performance of the upstream rotor. Additionally, this indicates that the upstream rotor experiences an increase in the axial induction factor when in a dual-rotor configuration. This increase can be attributed to the back-pressure effects caused by the downwind rotor. Such changes influence the flow field

around the upstream rotor, which can subsequently affect its power extraction capabilities. Subsequently, affect its power extraction capabilities.

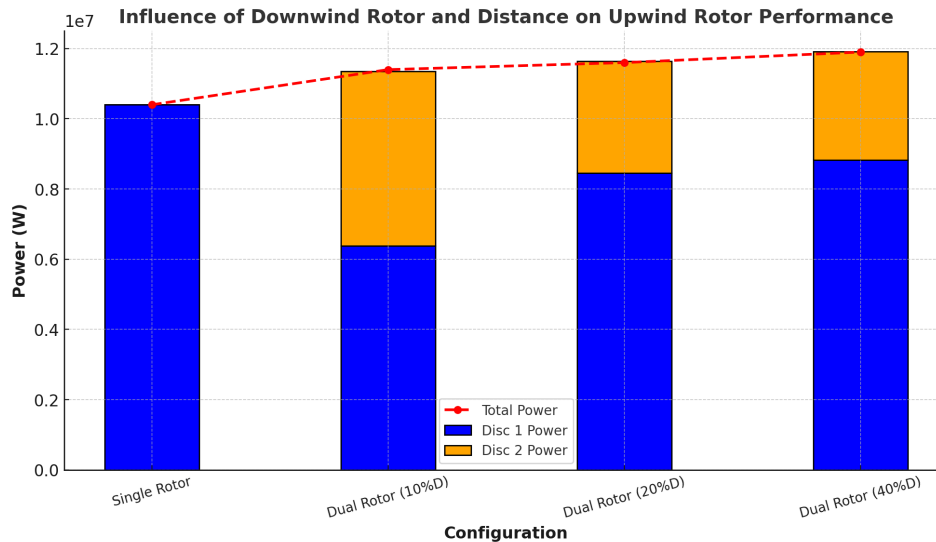


**Figure 5.21:** Influence of downwind rotor on upwind rotor for different rotor spacing

**Table 5.1:** Power Output for Single and Dual Rotor Configurations at Varying Spacings

| Configuration             | Upwind Rotor Power [W] | Downwind Rotor Power [W] | Total Power [W]    |
|---------------------------|------------------------|--------------------------|--------------------|
| Single Rotor              | $1.04 \times 10^7$     |                          | $1.04 \times 10^7$ |
| Dual Rotor (spacing 10%D) | $6.38 \times 10^6$     | $4.97 \times 10^6$       | $1.14 \times 10^7$ |
| Dual Rotor (spacing 20%D) | $8.45 \times 10^6$     | $3.19 \times 10^6$       | $1.16 \times 10^7$ |
| Dual Rotor (spacing 40%D) | $8.83 \times 10^6$     | $3.08 \times 10^6$       | $1.19 \times 10^7$ |

Figure 5.22 to Figure 5.24 shows contour plots of the normalised axial velocity ( $U_x/U_\infty$ ) for single and dual rotor wind turbine configurations at various thrust coefficients ( $C_T = 0.2, 0.6,$  and  $1.2$ ). The specified low, medium and high loading values are applied only to the upwind rotor, while the downwind rotor operates at the optimal tip speed ratio of 8. Each figure includes a comparison between the single-rotor and dual-rotor configurations, as well as a zoomed-in view showing the wake characteristics near the rotors. The plots show the increasing impact of loads on the wake dynamics and the combined influence observed in dual rotor configurations.

It has been observed that as the loading on the upwind rotor increases, the velocity deficit also increases. This results in a lower inflow velocity for the downwind rotor. Additionally, high loading on the upwind rotor can increase overall thrust, which may raise structural concerns.

Figures Figure 5.25 to Figure 5.27 illustrate the pressure contours normalized with atmospheric pressure for low, medium, and high loading conditions in both single and dual rotors. This comparison highlights the pressure variation between the upwind and downwind rotors. The rotor spacing is set at 10

For low loading values, the pressure drop is lower, indicating that the downwind rotor has a reduced influence on the upwind rotor. In contrast, as the loading on the upwind rotor increases, a higher pressure drop is observed, demonstrating a greater influence from the downwind rotor.

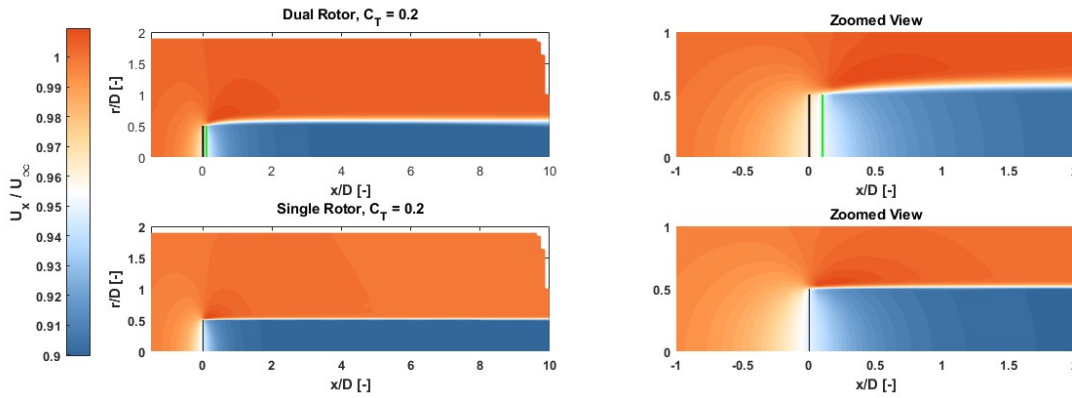


Figure 5.22: Normalized velocity contours for single and dual rotor configurations with  $C_T = 0.2$ .

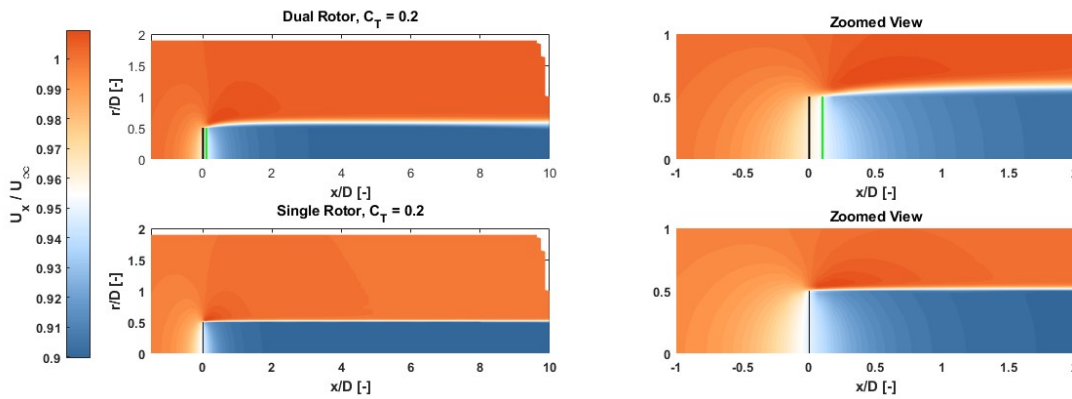


Figure 5.23: Normalized velocity contours for single and dual rotor configurations with  $C_T = 0.6$ .

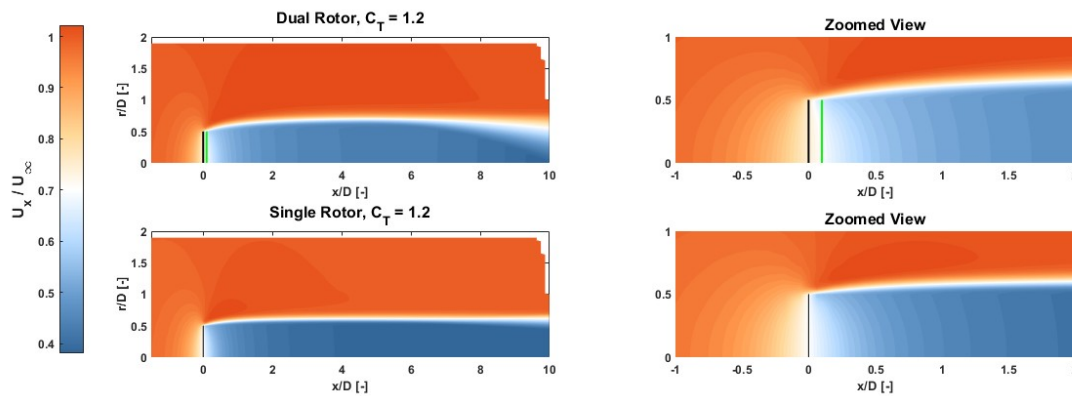
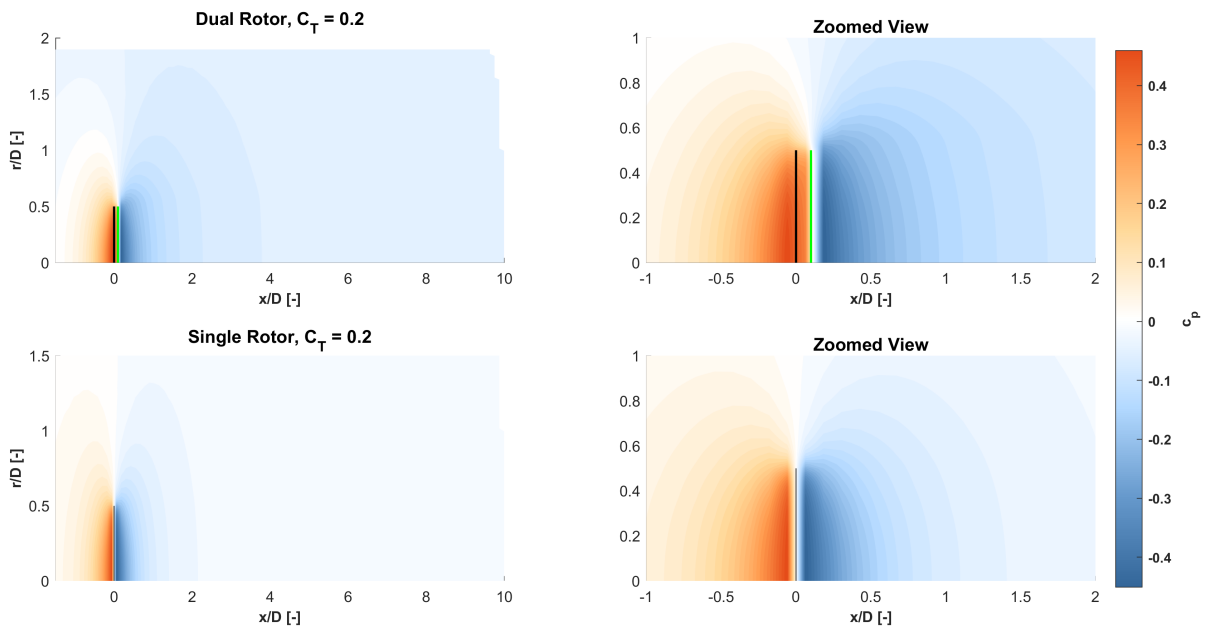
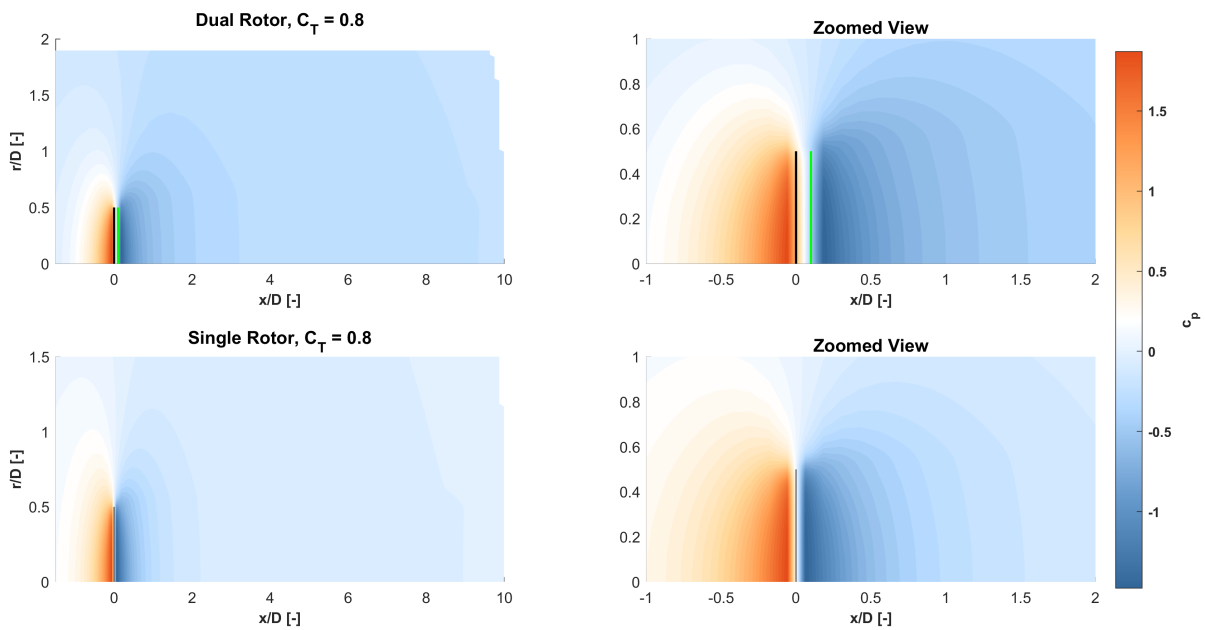


Figure 5.24: Normalized velocity contours for single and dual rotor configurations with  $C_T = 1.2$ .



**Figure 5.25:** Comparing pressure coefficient for the single rotor to dual rotor with  $C_T = 0.2$



**Figure 5.26:** Comparing pressure coefficient for the single rotor to dual rotor with  $C_T = 0.8$

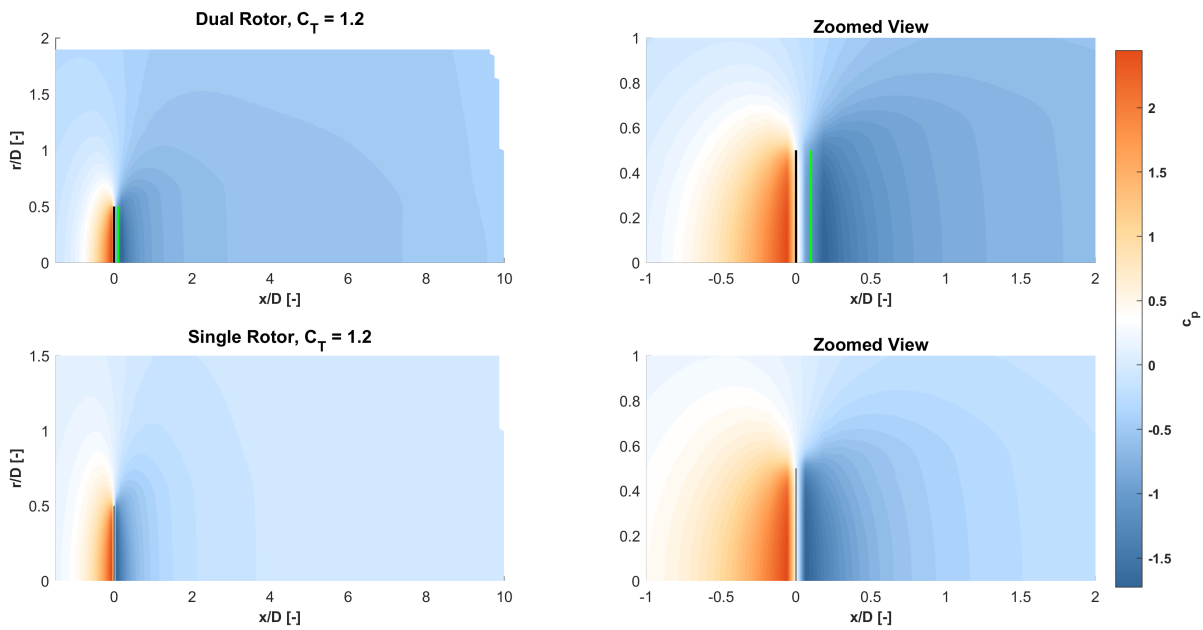


**Figure 5.27:** Comparing pressure coefficient for the single rotor to dual rotor with  $C_T = 1.2$

The Table 5.2 shows the comparison of power captured by upwind rotor and downwind rotor. The values align with the above discussion the same can be observed in the Figure 5.28

**Table 5.2:** Comparison of Power Output for Single and Dual Rotor Configurations with Varying  $C_T$

| $C_T$ (Upwind Rotor) | Case                      | Upwind Rotor Power [W] | Downwind Rotor Power [W] | Total Power [W] |
|----------------------|---------------------------|------------------------|--------------------------|-----------------|
| 0.2                  | Single Rotor              | 3.12E+06               |                          | 3.12E+06        |
|                      | Dual Rotor (Spacing 10%D) | 2.39E+06               | 8.55E+06                 | 1.09E+07        |
| 0.4                  | Single Rotor              | 6.07E+06               |                          | 6.07E+06        |
|                      | Dual Rotor (Spacing 10%D) | 4.46E+06               | 6.77E+06                 | 1.12E+07        |
| 0.6                  | Single Rotor              | 7.98E+06               |                          | 7.98E+06        |
|                      | Dual Rotor (Spacing 10%D) | 6.23E+06               | 5.25E+06                 | 1.15E+07        |
| 0.8                  | Single Rotor              | 1.04E+07               |                          | 1.04E+07        |
|                      | Dual Rotor (Spacing 10%D) | 6.38E+06               | 4.97E+06                 | 1.14E+07        |
| 1.2                  | Single Rotor              | 1.19E+07               |                          | 1.19E+07        |
|                      | Dual Rotor (Spacing 10%D) | 9.59E+06               | 2.23E+06                 | 1.18E+07        |

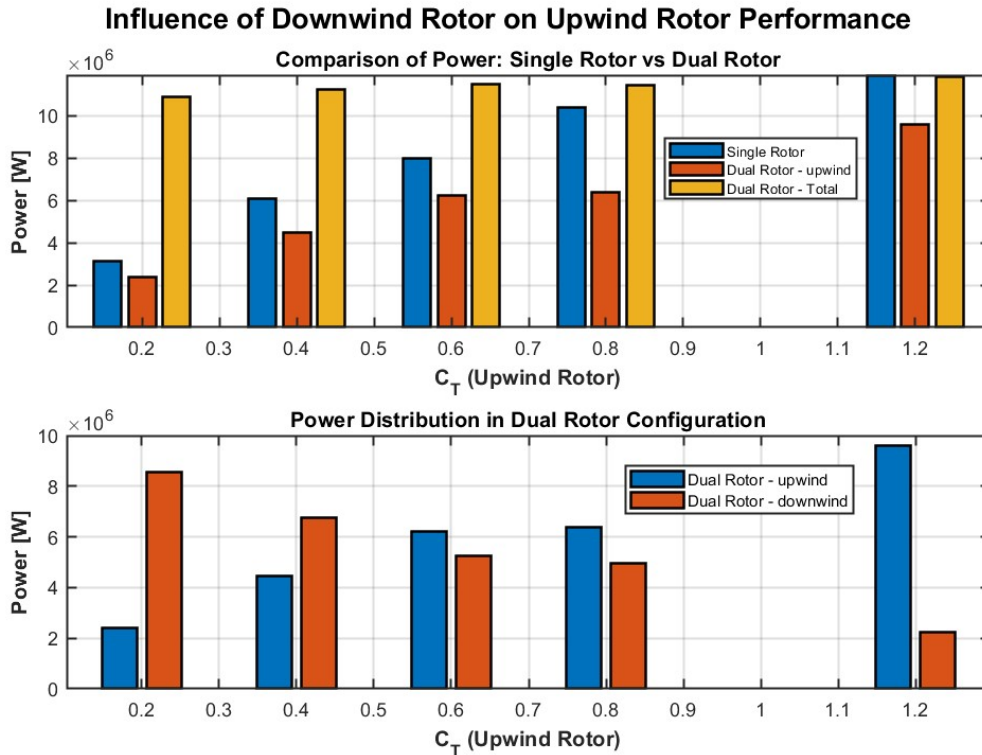


**Figure 5.28:** influence of the downwind rotor on upwind rotor for variable upwind loading and downwind rotor TSR = 8

## 5.4 Summary

This chapter provides an in-depth analysis of the dual-rotor wind turbine performance when the "no rotation" assumption was made. Different from the baseline configuration, the dual-rotor configuration has a wake that significantly alters the flow field behind it. Overall, the dual-rotor configuration has wake interactions that are much more complex than a single rotor, and it requires careful attention to the velocity deficits and axial induction factors to understand how the total installed power can be affected by this configuration.

The velocity deficit behind the upstream rotor was evaluated for various tip-speed ratios ( $\lambda$ ) and pitch angles, assuming optimal conditions for the upstream rotor. It was observed that closer rotor spacing ( $0.1D$ ) leads to significant wake interactions, resulting in reduced upstream velocities and increased axial induction factors. These effects are caused by the back-pressure generated by the downstream rotor, which influences the flow field around the upstream rotor and increases energy extraction.

Optimal rotor placement and operating conditions were explored, highlighting that closer downstream distances (e.g., 10% rotor diameter) maximise the overall power and thrust efficiency of the dual-rotor system. At this spacing, the system captures up to 61% of the available energy, with the downstream rotor contributing a substantial portion of the total power output. However, increasing the downstream distance to  $20%D$  and  $40%D$  reduces power capture due

to wake dissipation and velocity deficit recovery.

The performance changes due to variations in tip-speed ratio and pitch angle are studied. These analyses demonstrated that balanced tip-speed ratios between the upstream and downstream rotors maximize total power output from the wind turbine. More specifically, it is observed that for the best performance of the wind turbine when both the rotors maintain  $\lambda_{downwind}/\lambda_{upwind} \approx 1.83$ .

Simulations using the Actuator Disc Model were used to assess the three-dimensional wake effects and to validate the results. These simulations allowed for much more detailed flow interaction to be captured compared to the one-dimensional momentum theory. They also provided a more realistic representation of the wake velocity profile and the axial induction factor.

This chapter underscores that, to make dual-rotor wind turbine systems work better, you need to pay special attention to the placement of the downstream rotor, the conditions under which the system operates, and to ensure that both rotors are coordinated with respect to the turbine's thrust-to-speed ratio and the pitch of their blades.

# CHAPTER 6

## Co and Counter Rotating Dual Rotor Performance

### 6.1 Introduction

The dual rotor with wake rotation is analyzed using the relationship provided by O. Gur [16] as described in chapter 3, where the near-wake variation is assumed to vary linearly and accounts for wake rotation through the induced velocity. Similarly to the no-wake rotation case, performance analyses are conducted for both co-rotating and counter-rotating configurations for different TSR and  $\theta_{opt} = 0$

### 6.2 BEM Results

The velocity in the wake is calculated within the BEM loop for the downwind rotor. Figure 6.1 shows the velocity variation in the downstream region for upstream velocity 11m/s. The linear assumption model predicts a larger velocity deficit compared to Wilson's model. However, Wilson's model is specifically calculated along the centerline of the actuator disc. As seen in ADM simulations, the velocity variation at the center of the disc is lower, while at 0.95R, the velocity curve shows greater fluctuations. The relationship proposed by O. Gur calculates an average downstream velocity, effectively capturing these variations, as shown in the Figure 6.1.

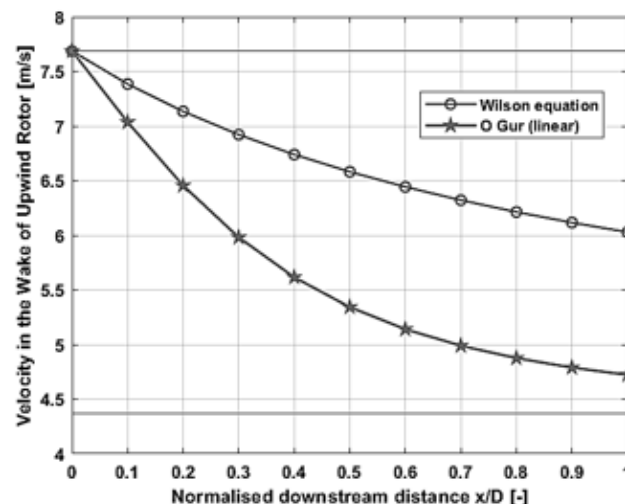
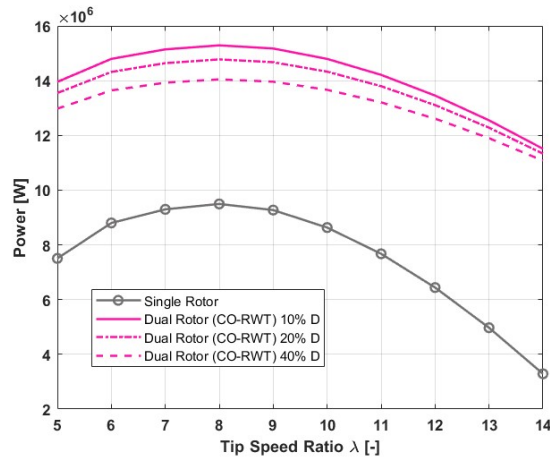


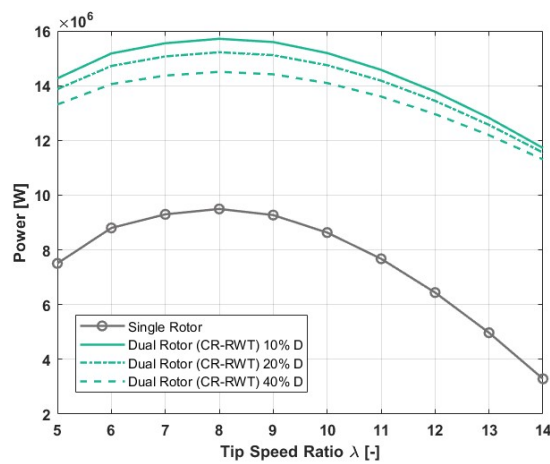
Figure 6.1: Comparing the velocity deficit equations given by Wilson [28] and Gur [16]

## 6.2.1 Comparing CO-RWT and CR-RWT the performance

Figure 6.2 and Figure 6.3 show the total power for co-rotating and counter-rotating configurations, with the upwind rotor operating under optimal conditions and the TSR varied for the downwind rotor. In both configurations. The highest total power is observed when the rotors are placed at  $10\%D$ , with a gradual decrease in total power as the distance between the rotors increases. Similar to no-rotation case described in chapter 5

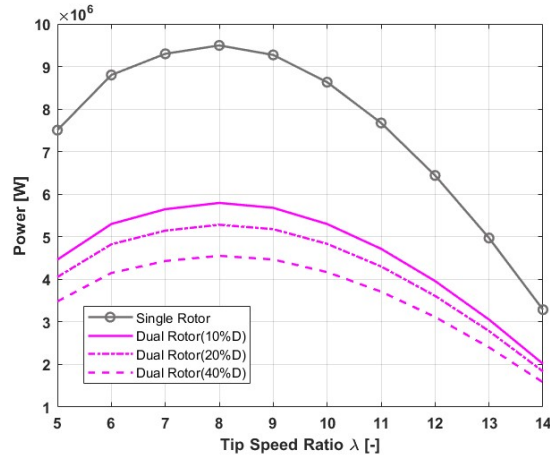


**Figure 6.2:** Comparing the single-rotor Power [W] to the Co-Rotating Configuration

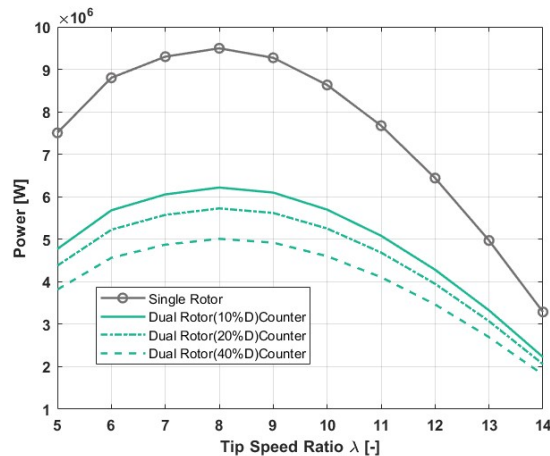


**Figure 6.3:** Comparing the singleT Power [W] to the Counter-Rotating Configuration

Figure 6.4 and Figure 6.5 shows the downwind performance of the co and counter-rotating configurations. The counter-rotating configuration shows a higher power extraction compared to the co-rotating configuration. The counter-rotating configuration achieves improved wake recovery leading to higher power efficiency at larger spacings (e.g.,  $20\% D$  and  $40\% D$ ). Unlike the co-rotating configuration, the counter-rotating setup benefits from better flow alignment, which enhances the performance of the downstream rotor and minimizes wake effects.



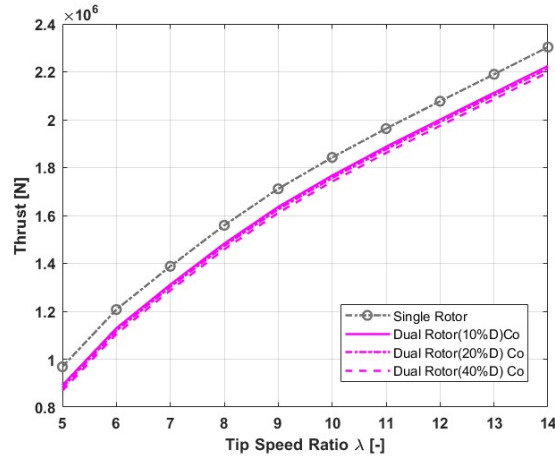
**Figure 6.4:** Comparing the single rotor Power [W] to the downwind rotor in co-rotating configuration



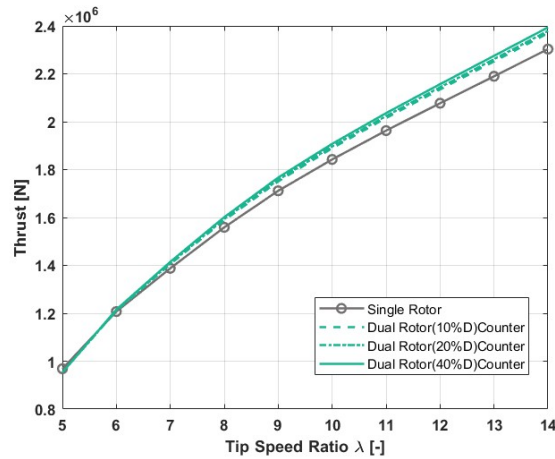
**Figure 6.5:** Comparing the single-rotor Power [W] to the downwind rotor in counter-rotating configuration

The Figure 6.6 compares the thrust output for single-rotor and dual-rotor in the co-rotating configuration. The DRWT exhibits higher thrust values than the SRWT due to the additional loading introduced by the downstream rotor. At closer spacings (10%D), the thrust on the downstream rotor increases significantly, but this also intensifies wake interactions. As spacing increases the thrust values decrease slightly due to wake dissipation and reduced aerodynamic loading on the downstream rotor.

The Figure 6.7 presents the thrust output for the counter-rotating configuration. The counter-rotating setup achieves better load distribution between the upstream and downstream rotors. At 10%D the total thrust is highest, but the counter-rotating configuration ensures a more balanced wake recovery. At larger spacings, the thrust decreases gradually due to reduced wake interactions and lower aerodynamic loading on the downstream rotor.10%D



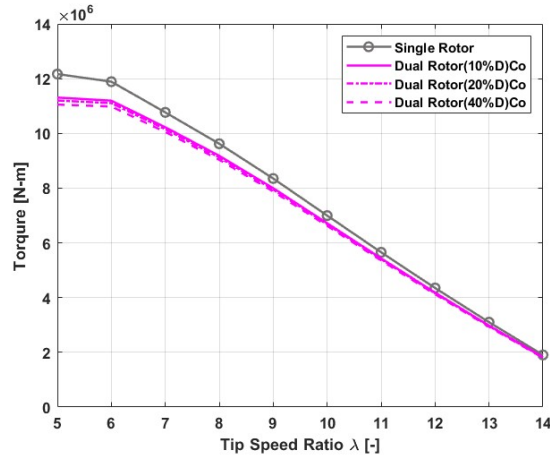
**Figure 6.6:** Comparing the single-rotor Thrust [N] output to downwind rotor (co-rotating)



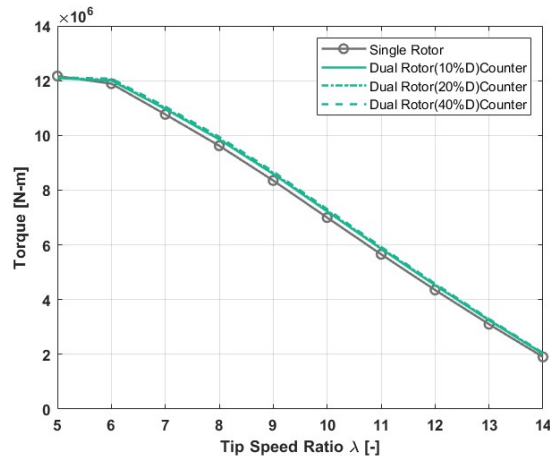
**Figure 6.7:** Comparing the single-rotor Thrust [N] output to downwind rotor (counter-rotating)

Figure 6.8 and Figure 6.9 show the torque generated by the downwind rotor for co-rotating and counter-rotating configurations, respectively. In co-rotating configurations, the downstream rotor benefits from a higher velocity inflow. However, as the spacing increases, the torque values decrease slightly due to reduced wake interactions and lower effective inflow velocity at the downstream rotor.

Similar to thrust, the counter-rotating setup ensures better wake recovery and load distribution. At 10%  $D$ , the torque is highest due to the optimized flow alignment between the upstream and downstream rotors. As the spacing increases to 20%  $D$  and 40%  $D$ , the torque values gradually decrease due to reduced wake effects and lower energy availability for the downstream rotor.



**Figure 6.8:** Comparing the SRWT Torque [N-m] output to downwind rotor (co-rotating)



**Figure 6.9:** Comparing the SRWT Torque [N-m] output to downwind rotor (counter-rotating)

It is observed that for the co-rotating configuration, higher power and torque are achieved at closer spacings (10%  $D$ ), but this comes at the cost of stronger wake interactions and reduced wake recovery. In contrast, the Counter-Rotating Configuration exhibits better wake recovery and higher power efficiency at larger spacings (20%  $D$  and 40%  $D$ ) due to improved flow conditions and reduced turbulence. The optimal configuration depends on the choice of spacing and configuration, based on the desired trade-off between power output, wake recovery, and aerodynamic loading.

The Figure 6.10 and Figure 6.11 shows the the total power for combination of TSR for upwind and downwind rotor for both co-rotating and counter-rotating configurations. Similar to the no-rotation, the co-rotating and counter-rotating the lower TSR in the upwind rotor shows higher value. the magnitude changes for co-rotating and counter-rotating configurations. A similar results are observed for thrust as shown in Figure 6.12 and Figure 6.13.

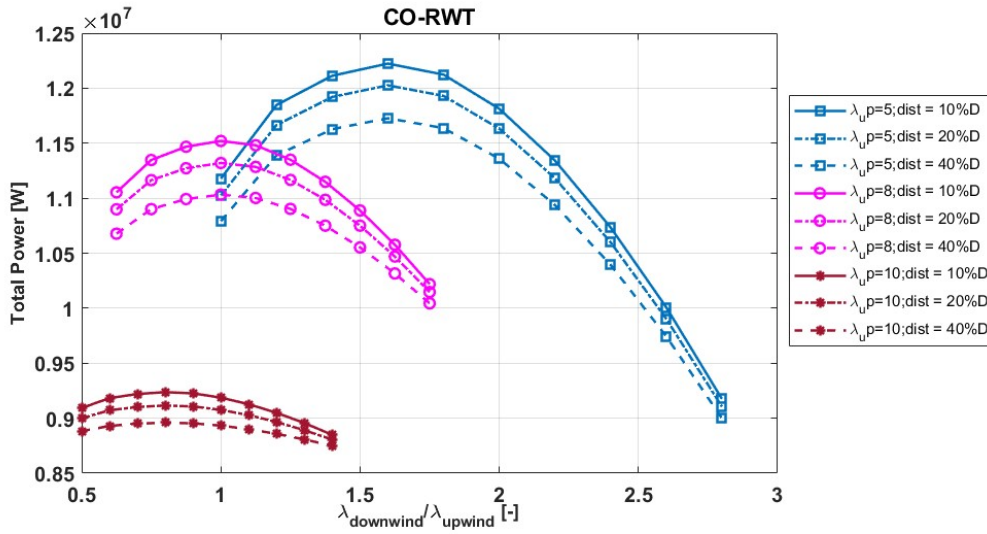


Figure 6.10: Comparing the total power for various TSR combinations for co-rotating

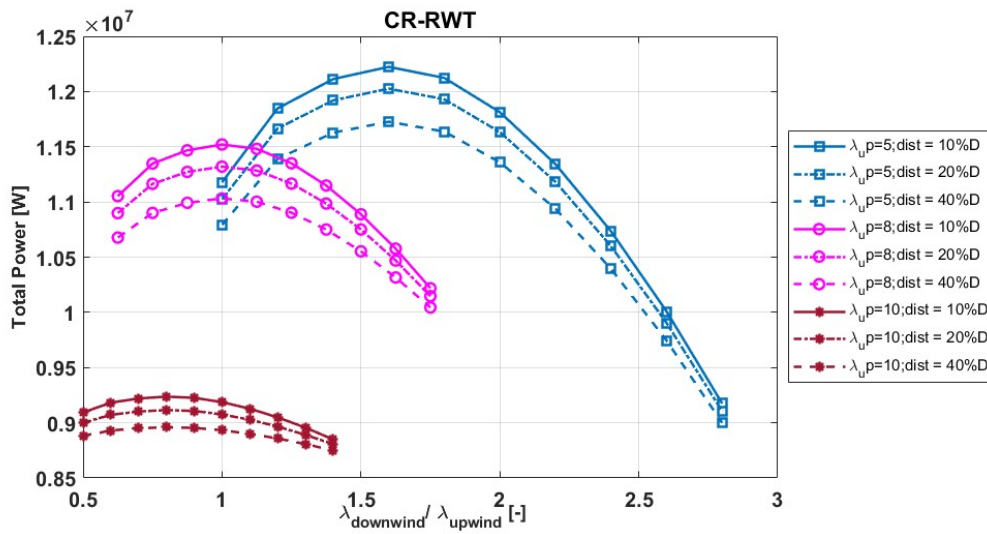


Figure 6.11: Comparing the total power for various TSR combinations for counter-rotating

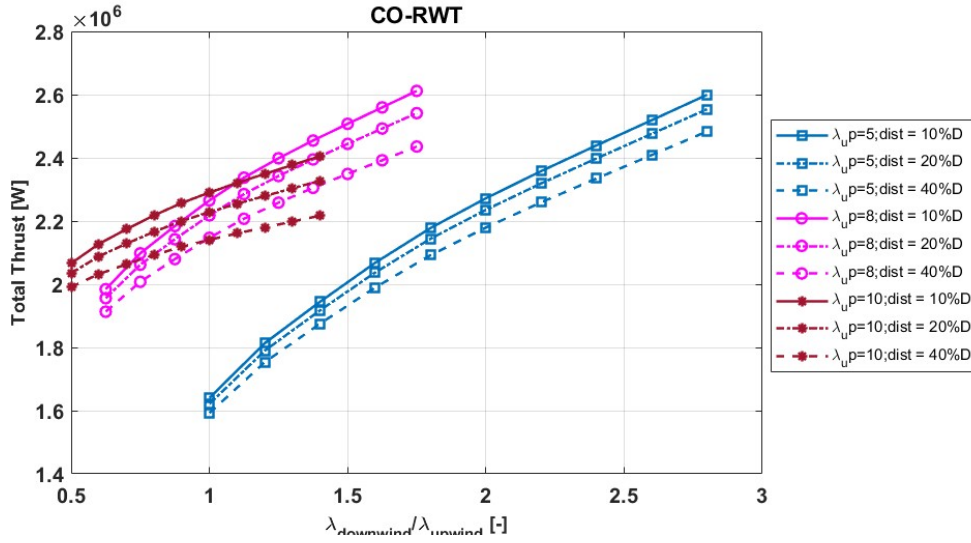


Figure 6.12: Comparing the total thrust for various TSR combinations for co-rotating

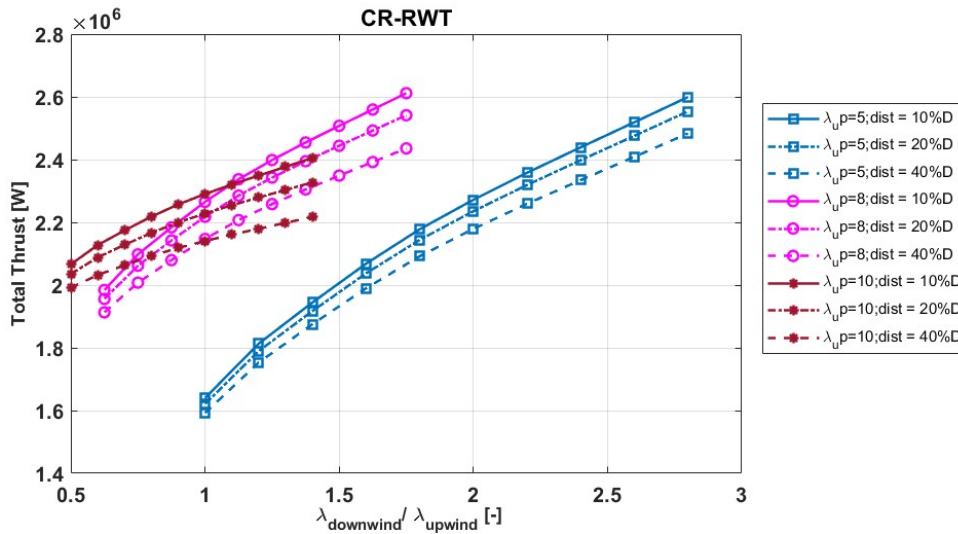
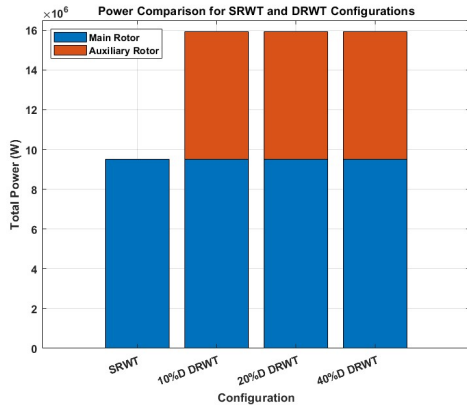


Figure 6.13: Comparing the total thrust for various TSR combinations for counter-rotating

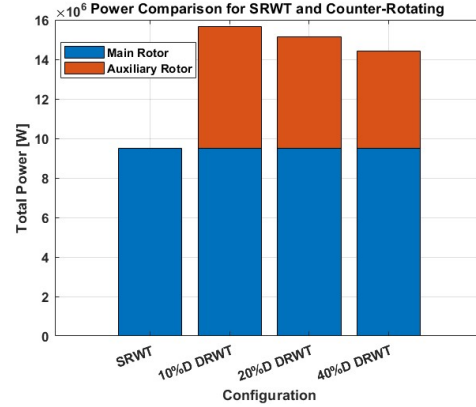
## 6.3 Power Comparison for Optimal Co-Rotating and Counter-Rotating Configurations

Figure 6.14 and Figure 6.15 illustrate the total power output for co-rotating and counter-rotating configurations, respectively. The DRWT consistently produces higher power than the SRWT due to the additional energy extracted by the downstream rotor. For the co-rotating configuration (Figure 6.14), the highest power is achieved at a rotor spacing of  $10\%D$ , where the downstream rotor operates in the high-velocity region of the upstream rotor's wake. As the rotor spacing increases to  $20\%D$  and  $40\%D$ , the power output decreases due to wake dissipation and reduced energy availability for the downstream rotor.

In the counter-rotating configuration, the DRWT achieves slightly higher power compared to the co-rotating setup at larger spacings (20% $D$  and 40% $D$ ). This improvement is attributed to better wake recovery and reduced turbulence in the counter-rotating design. Nevertheless, the total power is still maximized at 10% $D$ , similar to the co-rotating configuration.



**Figure 6.14:** Comparing Total power for Co Rotating configuration



**Figure 6.15:** Comparing Total power for Counter Rotating configuration

Figure 6.18 and Figure 6.17 show the normalized total power for co-rotating and counter-rotating configurations relative to the SRWT. In the co-rotating configuration, the DRWT achieves a normalized power of 1.62 at 10% $D$ , decreasing to 1.56 at 20% $D$  and 1.49 at 40% $D$ . Similarly, in the counter-rotating configuration, the normalized power is 1.66 at 10% $D$ , 1.58 at 20% $D$ , and 1.52 at 40% $D$ . These results highlight that the counter-rotating setup consistently outperforms the co-rotating configuration at larger spacings, primarily due to improved wake recovery.

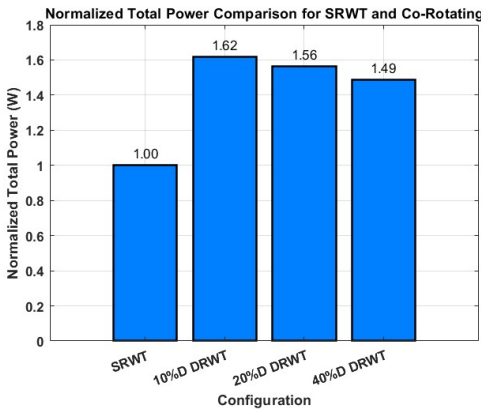


**Figure 6.16:** Comparing performance for Co-Rotating configuration

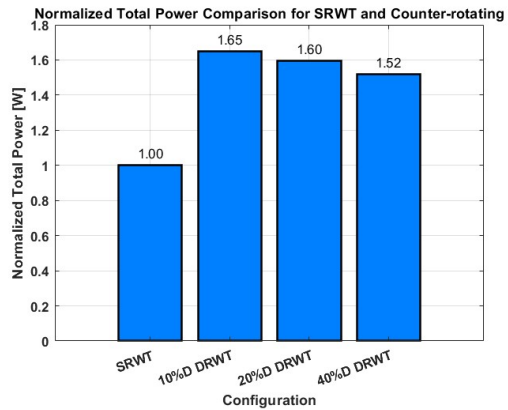


**Figure 6.17:** Comparing performance for Counter Rotating configuration

### 6.3.1 Power Contributions from Individual Rotors

The tables provide a detailed breakdown of power contributions from the upstream (Disc 1) and downstream (Disc 2) rotors for both configurations:

- In the **co-rotating configuration**, the downstream rotor contributes  $5.87\text{E}+06$  W at  $10\%D$ , decreasing to  $5.36\text{E}+06$  W at  $20\%D$  and  $4.63\text{E}+06$  W at  $40\%D$ .
- In the **counter-rotating configuration**, the downstream rotor contributes  $6.15\text{E}+06$  W at  $10\%D$ , higher than the co-rotating case. As the spacing increases to  $20\%D$  and  $40\%D$ , the downstream rotor's contribution decreases to  $5.35\text{E}+06$  W and  $4.93\text{E}+06$  W, respectively.

The results indicate that the Dual Rotor Wind Turbine (DRWT) achieves optimal performance at  $10\%D$  for both co-rotating and counter-rotating configurations. However, the counter-rotating setup provides slightly better power efficiency when the rotor spacing is larger. This improved performance in the counter-rotating configuration can be attributed to enhanced wake recovery and reduced turbulence, making it a more effective design for maximizing total power output in dual-rotor systems.

| Co-Rotating                   | Upwind Rotor Power [W] | Downwind Rotor Power [W] | Total Power[W]    |
|-------------------------------|------------------------|--------------------------|-------------------|
| Single Rotor                  | $9.49\text{E}+06$      |                          | $9.49\text{E}+06$ |
| Dual Rotor (spacing $10\%D$ ) | $9.49\text{E}+06$      | $5.87\text{E}+06$        | $1.54\text{E}+07$ |
| Dual Rotor (spacing $20\%D$ ) | $9.49\text{E}+06$      | $5.36\text{E}+06$        | $1.49\text{E}+07$ |
| Dual Rotor (spacing $40\%D$ ) | $9.49\text{E}+06$      | $4.63\text{E}+06$        | $1.41\text{E}+07$ |

| Counter-Rotating              | Upwind Rotor Power [W] | Downwind Rotor Power [W] | Total Power [W]   |
|-------------------------------|------------------------|--------------------------|-------------------|
| Single Rotor                  | $9.49\text{E}+06$      |                          | $9.49\text{E}+06$ |
| Dual Rotor (spacing $10\%D$ ) | $9.49\text{E}+06$      | $6.15\text{E}+06$        | $1.56\text{E}+07$ |
| Dual Rotor (spacing $20\%D$ ) | $9.49\text{E}+06$      | $5.65\text{E}+06$        | $1.51\text{E}+07$ |
| Dual Rotor (spacing $40\%D$ ) | $9.49\text{E}+06$      | $4.93\text{E}+06$        | $1.44\text{E}+07$ |

## 6.4 Model comparison

The Figure 6.18 shows the comparison of the three models used to study the dual-rotor configurations. It is observed the velocity in the wake varies as each model has different assumptions and limitations. Table 6.3 provides a detailed comparison of the models. The parametric analysis indicates that the counter-rotating configuration exhibits slightly higher power extraction and improved efficiency. The models effectively demonstrate the influence of axial induction in comparison to tangential induction. A high-fidelity CFD model can offer better insights into the wake between the rotors, leading to more refined performance values.

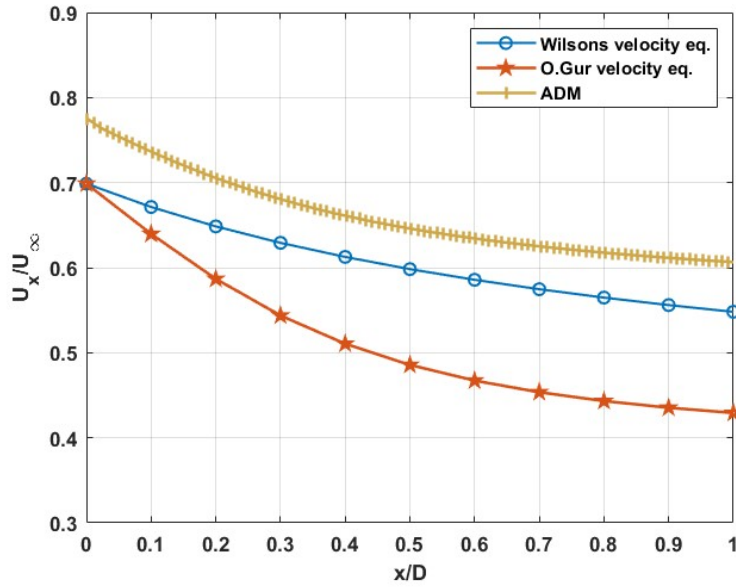


**Figure 6.18:** Comparing the different models used to compute the wake velocity in the downstream

**Table 6.3:** Comparison of Wilson’s Model, ADM, and Linear Variation (O Gur)

| Aspect               | Wilson’s Model                 | ADM (Constant Loading)                 | Linear Variation (O Gur)                      |
|----------------------|--------------------------------|--|---|
| Velocity Deficit     | Overpredicts far-wake deficit. | Realistic but assumes constant thrust. | Better near-wake modelling, variable deficit. |
| Tangential Induction | Neglected.                     | Included but constant.                 | Captures radial variation.                    |
| Wake Rotation        | Not modeled.                   | Simulated.                             | Detailed near-wake rotation.                  |
| Computational Cost   | Low.                           | Medium.                                | Low.  |
| Best Use Case        | Initial estimates, far-wake.   | Intermediate wake analysis.            | Near-wake and rotor interaction.              |

## 6.5 Summary

This chapter explores the performance of co-rotating and counter-rotating dual-rotor wind turbine configurations under optimal operating conditions. It utilizes various metrics, including wake interactions, power extraction, and structural loading, across different rotor spacings (10%  $D$ , 20%  $D$ , and 40%  $D$ ). The results enable several key conclusions: in both co-rotating and counter-rotating configurations, the dual-rotor system outperforms a single-rotor system of equivalent diameter.

The highest total power and torque were observed at 10% $D$  spacing for both configurations, with the co-rotating setup achieving strong energy extraction but experiencing increased wake interactions. In contrast, the counter-rotating configuration exhibited better wake recovery and higher power efficiency at larger spacings (20% $D$  and 40% $D$ ), benefiting from improved flow conditions and reduced wake. The normalized power comparisons indicated that the counter-rotating configuration slightly outperformed the co-rotating setup at larger spacings, achieving values of 1.66 at 10% $D$ , 1.58 at 20% $D$ , and 1.52 at 40% $D$ . Thrust and torque outputs trended similarly, with the counter-rotating configuration yielding a more balanced thrust/torque distribution across rotors that resembles the balance one would expect to find between a rotor and a counter-rotor. While the staggered configuration benefited from spacing optimization—being farther apart generally yielded better performance—the counter-rotating design emerged as the most balanced performer in terms of thrust and torque.

# CHAPTER 7

## Conclusion

---

This thesis comprehensively explored the performance and optimization of dual-rotor wind turbines, focusing on the effects of loading, induction, and design parameters on turbine efficiency, as well as comparing co-rotating and counter-rotating configurations. The findings provide critical insights into aerodynamic interactions and key design considerations for maximizing dual-rotor wind turbine performance.

The results demonstrated that the aerodynamic efficiency and overall performance of dual-rotor wind turbines are significantly influenced by axial and tangential loading, induction effects, and design parameters such as rotor spacing, blade pitch angle, rotational speed, and loading distribution between the upwind and downwind rotors. The induction effects from the upwind rotor created a wake deficit that directly impacted the inflow conditions for the downstream rotor. Close rotor spacings ( $10\%D$ ) resulted in higher power output due to enhanced energy extraction but also led to stronger wake interactions and increased aerodynamic loading. Larger spacings ( $20\%D$  and  $40\%D$ ) allowed for improved wake dissipation, leading to better downstream rotor performance.

The counter-rotating configuration consistently outperformed the co-rotating setup in terms of aerodynamic efficiency, particularly at larger rotor spacings. Improved wake recovery and reduced turbulence in the counter-rotating design provided superior inflow conditions for the downstream rotor, resulting in higher power generation and more balanced aerodynamic loading. Normalized power values for the counter-rotating configuration reached 1.66 at  $10\%D$ , 1.58 at  $20\%D$ , and 1.52 at  $40\%D$ , slightly exceeding those of the co-rotating configuration.

The study also identified optimal operating conditions for the counter-rotating configuration. These include rotor spacings of  $10\%D$  to  $20\%D$ , a moderate tip-speed ratio ( $\lambda_{upwind} = 8$ ), and a slight positive pitch angle difference between the upwind and downwind rotors. These parameters maximized energy extraction while ensuring sufficient wake recovery and minimizing mechanical stresses on turbine components.

Comparing co-rotating and counter-rotating configurations, the co-rotating setup exhibited higher power output at close spacings due to the increased energy extraction by the downstream rotor. However, the counter-rotating design demonstrated better performance at larger spacings, owing to its ability to mitigate wake effects and enhance energy recovery. These findings underscore the importance of selecting appropriate configurations and design parameters based on the desired trade-offs between power output, wake recovery, and structural loads.

This thesis establishes a foundation for understanding the aerodynamic interactions and optimization strategies for dual-rotor wind turbines. It emphasizes the critical role of rotor spacing, pitch angle, rotational speed, and loading distribution in achieving high turbine

---

efficiency. The counter-rotating configuration, with its superior wake dynamics and energy extraction capabilities, emerged as a promising design, particularly at larger spacings. Future research should explore unsteady flow effects, advanced control strategies, and experimental validations to further optimize dual-rotor wind turbine performance.

Future studies can focus on advancing numerical modeling techniques to further enhance the understanding and optimization of dual-rotor wind turbine performance. Incorporating unsteady flow effects, such as turbulence intensity, yawed inflow, and transient loading, can provide insights into the impact of real-world aerodynamic phenomena on turbine efficiency. High-fidelity simulations using CFD models, particularly with Large Eddy Simulations (LES) or Direct Numerical Simulations (DNS), can capture finer details of wake interactions and rotor dynamics, offering improved accuracy over existing models. Additionally, validation of these findings through wind tunnel or field experiments is crucial for refining numerical models and ensuring their reliability under practical operating conditions.

# Bibliography

---

- [1] Global Wind Energy Council. *Global Wind Report 2024*. Accessed: 2024-07-02. 2024. URL: <https://gwec.net/global-wind-report/>.
- [2] A Betz. “Zeitschrift für das gesamte Turbinenwesen”. In: *Zeitschrift für das gesamte Turbinenwesen* (1920), pp. 307–309.
- [3] Hui Hu and Anupam Sharma. *Innovative Dual-Rotor Wind Turbine (DRWT) Designs for Improved Turbine Performance and Wind Farm Efficiency*. Accessed: 2024-04-05. 2014. URL: [https://www.nsf.gov/awardsearch/showAward?AWD\\_ID=1438099](https://www.nsf.gov/awardsearch/showAward?AWD_ID=1438099).
- [4] B. G. Newman. “Multiple actuator-disc theory for wind turbines”. In: *Wind Energy Journal* 24.3 (2013), pp. 215–225.
- [5] V. A. Koehuan, Sugiyono, and S. Kamal. “Investigation of Counter-Rotating Wind Turbine Performance using Computational Fluid Dynamics Simulation”. In: *IOP Conference Series: Materials Science and Engineering*. Vol. 267. IOP Publishing. 2017, p. 012034. DOI: 10.1088/1757-899X/267/1/012034.
- [6] Q. Zhang and X. Liu. “Study on Tip-Speed Ratio Optimization for Dual-Rotor Turbines”. In: *Wind Power* 34 (2019), pp. 342–355.
- [7] W. Z. Shen et al. “Analysis of Counter-Rotating Wind Turbines”. In: *Journal of Physics: Conference Series* 75.1 (2007), p. 012003.
- [8] A. Riszal. “Analysis Effect Ratio of Rotation Rotors and Tip Speed Ratio (TSR) On The Variations of Distance Rotors Counter Rotating Wind Turbine (CRWT)”. In: *IOP Conference Series: Materials Science and Engineering*. Vol. 1273. ICoVEMAT 2018. IOP Publishing. 2019, p. 012060. DOI: 10.1088/1742-6596/1273/1/012060.
- [9] K. Yamamoto and S. Tanaka. “Rotor Separation Optimization for Counter-Rotating Turbines”. In: *Journal of Wind Energy* 41 (2022), pp. 123–136.
- [10] Seungmin Lee, Hogeon Kim, and Soogab Lee. “Analysis of Aerodynamic Characteristics on a Counter-Rotating Wind Turbine”. In: *Current Applied Physics* 10.suppl. 2 (2010), S339–S342.
- [11] Xuesong Wei et al. “Experimental investigation into the effects of blade pitch angle and axial distance on the performance of a counter-rotating tidal turbine”. In: *Ocean Engineering* 110 (2015), pp. 78–88. DOI: 10.1016/j.oceaneng.2015.09.037. URL: <https://www.sciencedirect.com/science/article/pii/S0029801815004680>.
- [12] C. Chantharasenawong, B. Suwantragul, and A. Ruangwiset. “Axial Momentum Theory for Turbines with Co-axial Counter Rotating Rotors”. In: *Commemorative International Conference of the Occasion of the 4th Cycle Anniversary of KMUTT Sustainable Development to Save the Earth: Technologies and Strategies Vision 2050 (SDSE2008)*. Bangkok, Thailand, 2008, 11–13 December.

- [13] Haripriya Sundararaju et al. “Aerodynamics and CFD analysis of equal size dual-rotor wind turbine”. In: *Journal of Renewable and Sustainable Energy* 9.043305 (2017).
- [14] Sung Nam Jung, Tae-Soo No, and Ki-Wahn Ryu. “Aerodynamic performance prediction of a 30 kW counter-rotating wind turbine system”. In: *Renewable Energy* 30 (2005), pp. 631–644.
- [15] S. Lee et al. “Effects of Design Parameters on Aerodynamic Performance of a Counter-Rotating Wind Turbine”. In: *Renewable Energy* 42 (2012), pp. 140–144.
- [16] Ohad Gur. “Extending Blade-Element Model to Contra-Rotating Configuration”. In: *IOP Conference Series: Materials Science and Engineering*. Vol. 638. 2019, p. 012001. DOI: 10.1088/1757-899X/638/1/012001.
- [17] P. Santhana Kumar et al. “Computational and Experimental Analysis of a Counter-Rotating Wind Turbine System”. In: *Journal of Scientific & Industrial Research* 72 (2013), pp. 300–306.
- [18] Michał Pacholczyk, Krzysztof Blecharz, and Dariusz Karkosiński. “Study on the Influence of an Axial Distance Between Rotors on a Performance of a Small Counter-Rotating Wind Turbine”. In: *Proceedings of the 5th World Congress on New Technologies (NewTech'19)*. Lisbon, Portugal, 2019. DOI: 10.11159/icert19.119.
- [19] Saixian Bian et al. “CFD simulation of the aerodynamic performance of co-axial multi-rotor wind turbines using the actuator line method”. In: *Ocean Engineering* 311 (2024), p. 118933. DOI: 10.1016/j.oceaneng.2023.118933.
- [20] Z. Wang et al. “An experimental study on the aerodynamic performances and wake characteristics of an innovative dual-rotor wind turbine”. In: *Energy* 147 (2018), pp. 94–109. DOI: 10.1016/j.energy.2018.01.020.
- [21] I Ushiyama, T Shimota, and Y Miura. “An experimental study of the two-staged wind turbines”. In: *Renewable Energy* 9.1 (1996), pp. 909–912.
- [22] M. S. Adaramola and P.Å. Krogstad. “Experimental investigation of wake effects on wind turbine performance”. In: *Renewable Energy* 36.8 (2011), pp. 2078–2086. DOI: 10.1016/j.renene.2011.01.024.
- [23] A. Ozbay, W. Tian, and H. Hu. “Experimental investigation on the wake characteristics and aeromechanics of dual-rotor wind turbines”. In: *Wind Turbines* 138.4 (2014). DOI: 10.1115/1.4031476.
- [24] W. Yuan et al. “An experimental study on the effects of relative rotation direction on the wake interferences among tandem wind turbines”. In: *Wind Turbines* 57 (2014). DOI: 10.1007/s11433-014-5429-x.
- [25] A. Author and B. Other. “Technical, Ecconomical, and Marketing Analyses of Corotating Dual-Rotor Wind Turbines”. In: *Journal of Renewable Energy Research* (2023). Available at: [URL if available], pp. 123–456.
- [26] China Wind Power News. *The World’s First Huaneng Twin-Wheel Wind Turbine Completes Hoisting*. Available at: <https://inf.news/en/economy/f59cf4c6972cda5484105b004fc7a3c5.html>. 2023.
- [27] Tony Brunton et al. *Wind Energy Handbook*. John Wiley and Sons, 1947.

- 
- [28] R. E. Wilson. “Wind Turbine Flow Field Model”. In: *ASME Journal of Solar Energy Engineering* 108 (1986), pp. 344–345.
- [29] “Numerical Study of Wake Characteristics in a Horizontal-Axis Hydrokinetic Turbine”. In: *An. Acad. Bras. Ciênc.* 88.4 (2016). DOI: 10.1590/0001-3765201620150652. URL: <https://doi.org/10.1590/0001-3765201620150652>.
- [30] The OpenFOAM Foundation. *OpenFOAM The Open Source CFD Toolbox: User Guide*. Available at <https://www.openfoam.com/documentation/user-guide>. 2023.
- [31] Thomas Amoretti et al. “Configurable Dual Rotor Wind Turbine Model Based on BEM Method: Co-Rotating and Counter-Rotating Comparison”. In: *Energy Conversion and Management* (2023).
- [32] Martin O L Hansen. *Aerodynamics for Wind Turbines*. Earthscan from Routledge, 2015.
- [33] Harika Gurram, Abhigyan Roy, and Prasanna Srinivasan. *Wind Turbine Technology: Assignment 1 - BEM Algorithm*. s223693, s222496, s223031. 2023.
- [34] Christian Bak et al. *The DTU 10-MW Reference Wind Turbine*. DTU Wind Energy, 2013. URL: <https://orbit.dtu.dk/>.
- [35] Arianna Sala. “CFD study of induction and finite blade effect on a floating horizontal-axis wind turbine”. Master’s Thesis. Delft, Netherlands: Delft University of Technology, 2023.
- [36] Eric Folmar et al. *Loads, Aerodynamics, and Control of Wind Turbines: Assignment 4 - Loads and AEP*. Group 3: s223520, s223693, s233727, s223031. 2023.
- [37] B. Tranberg, K. Tranberg, and D. Michalco. *Statistics*. n.d.